AUS DEM LEHRSTUHL FÜR COMPUTERUNTERSTÜTZTE KLINISCHE MEDIZIN
DER MEDIZINISCHEN FAKULTÄT MANNHEIM
DIREKTOR: PROF. DR. RER. NAT. LOTHAR R. SCHAD

Lung Imaging and Function Assessment using Non-Contrast-Enhanced Magnetic Resonance Imaging

INAUGURALDISSERTATION
ZUR ERLANGUNG DES DOCTOR SCIENTIARUM HUMANARUM (DR. SC. HUM.)
DER
MEDIZINISCHEN FAKULTÄT MANNHEIM
DER RUPRECHT-KARLS-UNIVERSITÄT
ZU
HEIDELBERG

vorgelegt von

EFE ILICAK

aus
ÇANKAYA, ANKARA

2023

Dean: Prof. Dr. med. Sergij Goerdt
Referee: Prof. Dr. rer. nat. Lothar R. Schad

Abstract

Measurement of pulmonary ventilation and perfusion has significant clinical value for the diagnosis and monitoring of prevalent lung diseases. To this end, non-contrast-enhanced MRI techniques have emerged as a promising alternative to scintigraphical measurements, computed tomography, and contrast-enhanced MRI. Although these techniques allow the acquisition of both structural and functional information in the same scan session, they are prone to robustness issues related to imaging artifacts and post-processing techniques, limiting their clinical utilization. In this work, new acquisition and post-processing techniques were introduced for improving the robustness of non-contrast-enhanced MRI based functional lung imaging. Furthermore, pulmonary functional maps were acquired in 2-year-old congenital diaphragmatic hernia (CDH) patients to demonstrate the feasibility of non-contrast-enhanced MRI methods for functional lung imaging.

In the first study, a multi-acquisition framework was developed to improve robustness against field inhomogeneity artifacts. This method was evaluated at 1.5T and 3T field strengths via acquisitions obtained from healthy volunteers. The results demonstrate that the proposed acquisition framework significantly improved ventilation map homogeneity ($p < 0.05$).

In the second study, a post-processing method based on dynamic mode decomposition (DMD) was developed to accurately identify dominant spatiotemporal patterns in the acquisitions. This method was demonstrated on digital lung phantoms and in vivo acquisitions. The findings indicate that the proposed method led to a significant reduction in dispersion of estimated ventilation and perfusion map amplitudes across different number of measurements when compared with competing methods ($p < 0.05$).

In the third study, the free-breathing non-contrast-enhanced dynamic acquisitions were obtained from 2-year-old patients after CDH repair, and then processed using the DMD to obtain pulmonary functional maps. Afterwards, functional differences between ipsilateral and contralateral lungs were assessed and compared with results obtained using contrast-enhanced MRI measurements. The results demonstrate that pulmonary ventilation and perfusion maps can be generated from dynamic acquisitions successfully without the need for ionizing radiation or contrast agents. Furthermore, lung perfusion parameters obtained with DMD MRI correlate very strongly with parameters obtained using dynamic contrast-enhanced MRI.

In conclusion, the presented work improves the robustness and accuracy of non-contrast-enhanced functional lung imaging using MRI. Overall, the methods introduced in this work may serve as a valuable tool in the clinical adaptation of non-contrast-enhanced imaging methods and may be used for longitudinal assessments of pulmonary functional changes.

Zusammenfassung

Die Messung der Lungenventilation und -perfusion ist von erheblichem klinischen Wert für die Diagnose und Überwachung häufiger Lungenerkrankungen. Die nicht kontrastmittelverstärkte MRT hat sich als vielversprechende Alternative zu szintigraphischen Messungen, Computertomographie und kontrastmittelverstärkter MRT erwiesen. Obwohl diese Technik die Erfassung sowohl struktureller als auch funktioneller Informationen in derselben Scansitzung ermöglicht, ist sie nicht sonderlich robust in Bezug auf Bildartefakte und Postprocessing-Techniken, was ihre klinische Anwendung einschränkt. In dieser Arbeit wurden neue Bildaufnahme- und Postprocessing-Techniken entwickelt, welche die Robustheit der nicht kontrastmittelverstärkten MRT-basierten funktionellen Lungenbildgebung verbessern. Darüber hinaus wurden Lungenfunktionskarten von 2-jährigen Patienten mit kongenitaler Zwerchfellhernie (CDH) erstellt, um die Durchführbarkeit von nicht kontrastmittelverstärkten MRT-Methoden für die funktionelle Lungenbildgebung zu demonstrieren.

Im ersten Teil dieser Arbeit wurde ein Multi-Erfassungs-Framework entwickelt, um die Bildaufnahme robuster gegenüber Feldinhomogenitätsartefakten zu machen. Diese Methode wurde bei Feldstärken von 1.5T und 3T anhand von Aufnahmen gesunder Probanden evaluiert. Es konnte gezeigt werden, dass das neu entwickelte Framework zur Bildaufnahme die Homogenität der Ventilationskarte signifikant verbessert ($p < 0.05$).

Im zweiten Teil dieser Arbeit wurde eine Postprocessing-Methode auf Basis der Dynamic Mode Decomposition (DMD) entwickelt, um dominante räumlich-zeitliche Muster in den Aufnahmen präzise zu identifizieren. Diese Methode wurde anhand digitaler Lungenphantome und in vivo-Messungen evaluiert. Verglichen mit herkömmlichen Methoden führte die hier entworfene Methode zu einer signifikanten Reduktion der Streuung der geschätzten Amplituden von Ventilations- und Perfusion-Karten bei unterschiedlicher Anzahl von Messungen ($p < 0.05$).

Im dritten Teil dieser Arbeit wurden nicht kontrastmittelverstärkte dynamische Aufnahmen bei freier Atmung in 2-jährigen Patienten nach CDH-Reparatur durchgeführt und anschließend mit Hilfe von DMD verarbeitet, um pulmonale Funktionskarten zu erstellen. Danach wurden funktionelle Unterschiede zwischen ipsilateralen und kontralateralen Lungen ausgewertet und mit Ergebnissen von kontrastmittelverstärkten MRT-Messungen verglichen. Es konnte gezeigt werden, dass aus den dynamischen Aufnahmen pulmonale Ventilations- und Perfusion-Karten erzeugt werden können ohne den Gebrauch von ionisierender Strahlung oder Kontrastmitteln. Darüber hinaus korrelieren Lungenperfusion-Parameter, die mit DMD MRT gemessen wurden, stark mit Parametern, die mittels dynamischer kontrastmittelverstärkter MRT gemessen wurden.

Zusammenfassend verbessert die vorgestellte Arbeit die Robustheit und Genauigkeit der nicht kontrastmittelverstärkten funktionellen Lungenbildgebung mittels MRT. Die hier eingeführten Methoden können als wertvolles Instrument bei der klinischen Anwendung von nicht kontrastmittelverstärkten Bildgebungsmethoden dienen und können für longitudinale Bewertungen von pulmonalen Funktionsänderungen verwendet werden.

Preface

Several chapters of this thesis have already been published or are currently submitted for publication. The citations for these chapters are:

Chapter 3: Efe Ilicak, Safa Ozdemir, Lothar R. Schad, Meike Weis, Stefan o. Schoenberg, Frank G. Zöllner, Jascha Zapp. "Phase-cycled balanced SSFP imaging for non-contrast-enhanced functional lung imaging." *Magnetic Resonance in Medicine.* 2022 Oct; 88(4): 1764-1774. doi:10.1002/mrm.29302.

Chapter 4: Efe Ilicak, Safa Ozdemir, Jascha Zapp, Lothar R. Schad, Frank G. Zöllner. "Dynamic Mode Decomposition of Dynamic MRI for Assessment of Pulmonary Ventilation and Perfusion." *Magnetic Resonance in Medicine.* 2023 Aug; 90(2): 761- 769. doi:10.1002/mrm.29656.

Chapter 5: Efe Ilicak[1], Greta Thater[1], Safa Ozdemir, Jascha Zapp, Lothar R. Schad, Stefan O. Schoenberg, Frank G. Zöllner[2], Meike Weis[2]. "Functional lung imaging of 2-year-old children after congenital diaphragmatic hernia repair using dynamic mode decomposition." *European Radiology*. Submitted on 19.04.2023.

---

[1] Efe Ilicak and Greta Thater contributed equally to this work.

[2] Frank G. Zöllner and Meike Weis contributed equally to this work.

Summary of publications included in cumulative dissertations

Name of the doctoral student: Efe Ilicak

Title of dissertation: Lung Imaging and Function Assessment using Non-Contrast-Enhanced Magnetic Resonance Imaging

Supervised by: Prof. Dr. Lothar R. Schad

☐ I wish to submit a cumulative dissertation, and hereby ask the doctoral committee to examine whether the quantity and quality of the proposed publications are sufficient to meet the requirements for a cumulative dissertation.

☒ The doctoral committee has previously examined whether my publications are suitable for a cumulative dissertation, and this is a final overview of the publications contained in my cumulative thesis.

1. List of peer-reviewed publications included in the cumulative dissertation. For each publication, provide a complete list of authors, title, journal, journal impact factor, and whether the manuscript has been accepted for publication, is in revision after peer review, or has been submitted and is awaiting peer review. Shared first authorships should be clearly indicated. Please also indicate whether the publication is an original research report, a review, or another type of article.

Publication 1

Efe Ilicak, Safa Ozdemir, Lothar R. Schad, Meike Weis, Stefan O. Schoenberg, Frank G. Zöllner, Jascha Zapp. Phase-cycled balanced SSFP imaging for non-contrast-enhanced functional lung imaging. Magnetic Resonance in Medicine. 2022 Oct; 88(4): 1764- 1774. doi:10.1002/mrm.29302. Impact Factor: 3.737. Article Type: Technical Note.

Publication 2

Efe Ilicak, Safa Ozdemir, Jascha Zapp, Lothar R. Schad, Frank G. Zöllner. Dynamic mode decomposition of dynamic MRI for assessment of pulmonary ventilation and perfusion. Magnetic Resonance in Medicine. 2023 Aug; 90(2): 761-769. doi: 10.1002/mrm.29656. Impact Factor: 3.737. Article Type: Technical Note.

Publication 3

Efe Ilicak*, Greta Thater*, Safa Ozdemir, Jascha Zapp, Lothar R. Schad, Stefan O. Schoenberg, Frank G. Zöllner**, Meike Weis**. Functional lung imaging of 2-year-old children after congenital diaphragmatic hernia repair using dynamic mode decomposition. European Radiology. Under Review. Impact Factor: 7.034. Article Type: Original Article.

* Efe Ilicak and Greta Thater contributed equally to this work.
** Frank G. Zöllner and Meike Weis contributed equally to this work.

2. Summary of the doctoral student's contribution to the work reported in each manuscript.

Work steps	Publication 1	Publication 2	Publication 3
Conception (%)	50%	100%	50%
Literature search (%)	90%	90%	90%
Ethics proposal (%)	0%	0%	0%
Animal experimentation proposal (%)	-	-	-
Data collection (%)	100%	100%	70%
Data analysis (%)	100%	100%	70%
Interpretation of results (%)	50%	90%	70%
Manuscript writing (%)	90%	95%	90%
Revision (%)	95%	95%	75%
Indicate which figures and tables resulted from your dissertation work.	Figures: 1-4 Tables: 1	Figures: 1-4 Tables: 1	Figures: 1-6 Tables: 1-5

3. For cumulative dissertations, the doctoral student should be first author on at least two of the publications. In the case of joint first authorship or last authorship, please justify below why the publication should be considered equivalent to a single first authorship.

The doctoral student is the first author of two publications, and only shares an authorship for the third publication.

I hereby certify that this is a true representation of the doctoral student's contribution to the publications listed.

Signature of the doctoral candidate

Prof. Dr. Lothar Schad
Lehrstuhl für Computerunterstützte Klinische Medizin
Medizinische Fakultät Mannheim
Universität Heidelberg
Theodor-Kutzer-Ufer 1-3
D-68167 Mannheim

Signature of supervisor

Contents

Abstract iii

Zusammenfassung iv

Preface v

1 Introduction 1
1.1 Motivation . . . 1
1.2 Outline . . . 2
1.3 Citation of Previous Publications . . . 3

2 Theoretical Background 5
2.1 Nuclear Magnetic Resonance . . . 5
2.1.1 Nuclear Spin . . . 5
2.1.2 Macroscopic Magnetization . . . 7
2.1.3 RF Excitation . . . 9
2.1.4 Free Precession and Relaxation . . . 10
Longitudinal Relaxation . . . 11
Transverse Relaxation . . . 11
2.1.5 Bloch Equation . . . 12
2.1.6 Gradient Fields . . . 13
2.1.7 Off-Resonance Sources . . . 14
2.2 Magnetic Resonance Imaging . . . 15
2.2.1 Signal Equation and k-Space . . . 15
2.2.2 Signal Localization . . . 16
Slice Selection . . . 16
Spatial Information Encoding . . . 17
Frequency Encoding . . . 17
Phase Encoding . . . 18
Echoes . . . 18
2.2.3 Sampling Requirements . . . 19
Field of View . . . 19
Spatial Resolution . . . 20
Noise Considerations . . . 21
2.3 Pulmonary Physiology . . . 22
2.3.1 Overview of the respiratory system . . . 22
Airways . . . 23
Alveolar-Capillary Unit . . . 24
Pulmonary Circulation . . . 24
Muscles of Respiration . . . 25
Mechanics of Breathing . . . 25
Ventilation-Perfusion Relationships . . . 26
2.3.2 Congenital Diaphragmatic Hernia . . . 27

2.4 MRI of the Lung 28
  2.4.1 Contrast-Enhanced Lung Imaging 29
  2.4.2 Non-contrast-Enhanced Lung Imaging 30
    Spin Echo-Based Sequences 31
    Ultrashort Echo Time-based Sequences 31
    Gradient Echo-Based Sequences 32
  2.4.3 Balanced Steady Steady-State Free Precession Imaging 32
  2.4.4 Non-contrast-Enhanced Functional Lung Imaging 34
  2.4.5 Challenges in Adaptations to Higher Field Strengths 35
  2.4.6 Challenges in Pediatric Imaging 36

3 Phase-cycled balanced SSFP imaging for non-contrast-enhanced functional lung imaging 39
3.1 Introduction 39
3.2 Methods 40
  3.2.1 Fourier decomposition MRI 40
  3.2.2 Phase-cycled bSSFP 40
  3.2.3 Adaptation of phase-cycled bSSFP for FD MRI 41
  3.2.4 Data acquisitions 42
  3.2.5 Image postprocessing and analyses 42
3.3 Results 44
3.4 Discussion 48
3.5 Conclusions 50
3.6 Appendix 50

4 Dynamic mode decomposition of dynamic MRI for assessment of pulmonary ventilation and perfusion 53
4.1 Introduction 53
4.2 Methods 54
  4.2.1 DMD 54
  4.2.2 DMD of the Respiratory Signal and Image Analyses 55
  4.2.3 Phantom Simulations 56
  4.2.4 MRI Data Acquisitions 58
4.3 Results 59
4.4 Discussion 60
4.5 Conclusion 62
4.6 Appendix 62

5 Functional lung imaging of 2-year-old children after congenital diaphragmatic hernia repair using dynamic mode decomposition 63
5.1 Introduction 63
5.2 Materials and methods 64
  5.2.1 Patients 64
  5.2.2 DMD-based Functional Pulmonary MRI 65
  5.2.3 MRI Protocols 65
  5.2.4 Data Analyses 67
  5.2.5 Statistical Analyses 67
5.3 Results 68
  5.3.1 Feasibility of pediatric DMD MRI 68
  5.3.2 DMD MRI-based pulmonary functional parameters 69
  5.3.3 TWIST-based pulmonary perfusion parameters 70

5.3.4 Comparisons between DMD-based perfusion and TWIST-based perfusion . . . 70
5.4 Discussion . . . 74

6 Summary **79**

7 Outlook **81**

Bibliography **83**

A Publications **97**
A.1 Peer-Reviewed Journal Publications . . . 97
A.2 Journal Publications Under Peer-Review . . . 98
A.3 Peer-Reviewed Conference Proceedings . . . 98

B Curriculum Vitae **101**
B.1 Personal Data . . . 101
B.2 Education . . . 101
B.3 Work Experience . . . 102
B.4 Teaching Experience . . . 102

C Acknowledgements **103**

List of Figures

2.1 (A) Nuclear magnetic moment vectors aligned in the direction of an external magnetic field. (B) The precession of the magnetic moment vector is clockwise when observed against the direction of the magnetic field. 7
2.2 Zeeman splitting for a spin-1/2 system. The spin in the spin-up (parallel) state is in the lower energy state. 8
2.3 (A) Longitudinal (T_1) relaxation process. (B) Transverse (T_2 and T_2^*) relaxation processes. 12
2.4 (A) In response to a rotating RF field, the magnetization vector $\vec{M}$ precesses around the x'-axis in the rotating frame. (B) In the laboratory frame, the actual motion of $\vec{M}$ is a spiral. 13
2.5 Desired slice is selected by application of a slice selection gradient and excitation with an appropriate RF pulse. 17
2.6 Sampling in k-space and corresponding replication in image domain. . . 20
2.7 Modeling of airway generations in human lung according to Weibel's lung model. In adults, air may pass through between 10 to 23 generations on its way to alveoli. 23
2.8 Schematics of the (A) lungs and (B) pulmonary acinus. 24
2.9 Various lung volumes and capacities. Inspiratory and expiratory phase in tidal breathing are shown equal durations for illustrative purposes. 26
2.10 Chest radiography acquired from a female infant with congenital diaphragmatic hernia reveals multiple loops of bowel occupying the left hemithorax, which shifts the cardiothymic structures to the right. Reproduced with permission from (Klein and Sirota, 2017), copyright Massachusetts Medical Society. 27
2.11 Representative ^{1}H, ^{3}He, and ^{129}Xe acquisitions from (i) healthy volunteer, (ii) non-small-cell lung cancer patient, and (iii) chronic obstructive pulmonary disease patient. Reproduced from (Stewart et al., 2018), used under Creative Commons CC-BY license. 30
2.12 The characteristic bSSFP off-resonance signal profiles for (A) lung parenchyma and (B) lipid tissue at different flip angles. Shapes of the signal profiles are a strong function of T_2/T_1 and α, and the optimal flip angle depends on the tissue relaxation properties. The simulation parameters: TE/TR=1/2 ms; $T_1 = 1100$ and $T_2 = 40$ for lung parenchyma; $T_1 = 300$ and $T_2 = 80$ for lipid tissue. Notice the scale difference between the plots, indicating a difference in achievable signal level from different tissue types. 33

3.1 Overview of the proposed method. Phase-cycled Fourier decomposition MRI uses balanced SSFP (bSSFP) acquisitions with different RF phase increments during free breathing. Images acquired with different phase-cycle increments are then individually processed with Fourier decomposition MRI to obtain respective functional maps. Afterward, quantitative maps are generated and large vessels are excluded. Finally, individual functional maps are weighted-combined to obtain final functional maps. 41
3.2 Quantitative ventilation maps (denoted as V Map) obtained from individual subgroups (SGs) and their combination are shown for a volunteer, overlaid on representative cross sections at 1.5T and 3T with respective CV (in units of 10^{-2}) values. In addition, difference maps between subgroups (SGs) and combined map and mean absolute error (MAE, in units of 10^{-2}) values are displayed. At both field strengths, local signal losses (orange arrows highlight for conventional $\Delta\phi = \pi$ acquisition) and signal inhomogeneity is observed across the SGs. In comparison, the combined maps reduce local signal losses while improving map homogeneity across lung parenchyma. 44
3.3 Quantitative perfusion maps (denoted as Q Map) obtained from individual SGs and their combinations are shown for a volunteer, overlaid on representative cross sections at 1.5T and 3T with respective CV (in units of 10^{-2}) values. In addition, difference maps between SGs and combined map and MAEs (in units of 10^{-2}) are displayed. At 3 T, individual SGs suffer from local signal losses within the lung parenchyma, as visible in the difference maps. In comparison, the combined maps reduce local signal losses while providing increased map homogeneity. 45
3.4 Combined functional maps of SGs for both methods overlaid on combined cross section at 1.5T and 3T. At both field strengths, the quantitative ventilation maps (denoted as V Map) obtained from phase-cycled acquisitions show robustness against local signal losses (orange arrows) compared with single-phase acquisitions. Regarding perfusion maps (denoted as Q Map), phase-cycled acquisitions display slightly reduced signal levels compared with single-phase acquisitions, due to averaging of multiple phase cycles, including acquisitions with suboptimal SNR. Nevertheless, phase-cycled acquisitions are able to reproduce prominent structures (teal arrows) at both field strengths and improve parenchymal perfusion depiction at 3T. 48
3.5 For the selection of air region, manual ROIs were used. The selected ROIs are displayed in color blue, overlaid on representative magnitude images in grayscale. Same ROIs were assigned for all subjects and at both field strengths. 51

4.1 Representative DMD modes obtained from a volunteer measurement. The modes are obtained from a rank-15 approximation. Here, only a single component of complex conjugate pairs is displayed. The corresponding mode frequencies (f) and mode amplitudes (b) are also displayed overlaid on the modes. The DMD algorithm provides physically interpretable results while identifying dominant spatiotemporal features; such as ventilation and perfusion related signal variations together with secondary motions or harmonics. Here, mode with $f = 0.41$ Hz was associated with ventilation related signal changes, whereas modes with $f = 1.05$ Hz and $f = 1.18$ Hz were associated with perfusion related signal changes. 57

4.2 (A) A noise-free digital phantom was generated with three different tissue types for $m = 480$ different measurements. Signal changes associated with ventilation and perfusion were simulated in parenchymal tissues, whereas for large vessel structures, perfusion related signal changes were simulated. (B) Signal changes across m are shown for a pixel in the parenchymal tissue (shown in (A) with red crosshair). (C) Ventilation and perfusion values were estimated using FD, MP, and DMD for measurement sets with different lengths, $\ell \in [50\ 480]$, and the mean values were obtained by averaging across parenchymal tissues. (D) For a more realistic case, bivariate Gaussian noise was added to the phantom, and respiratory and cardiac frequencies were varied. (E) Frequencies were linearly decreased during a 20-sample duration (shown with gray zone). The signal changes across m are shown for a pixel in parenchymal tissue (shown in (D) with red crosshair). (F) Ventilation and perfusion values were estimated using FD, MP, and DMD for measurement sets with $\ell \in [50\ 480]$, and mean values were obtained by averaging across parenchymal tissues. 58

4.3 Mean ventilation and perfusion results from a volunteer were calculated over the lung parenchyma across measurement sets with different lengths $\ell \in [50\ 250]$. (A) The selected ROI (displayed in white) encapsulating the lung parenchyma is shown overlaid on a representative bSSFP magnitude image. The mean ventilation and perfusion results are displayed in (B) and (C), respectively. FD shows a dependency on ℓ, resulting in oscillations in estimated amplitudes. MP decreases this dependency on ℓ and reduces the associated oscillations; however, it occasionally manifests sudden inconsistencies along consecutive measurements in the estimation of amplitudes. In contrast, the proposed DMD method further reduces the oscillatory behavior, and can estimate respective amplitudes robustly across different ℓ. . . 59

4.4 (A) Ventilation and (B) perfusion maps obtained from a volunteer for three sequential ℓ. Additionally, the mean ventilation and perfusion values are calculated over lung parenchyma (shown in white) and displayed overlaid on respective maps (mean values are scaled by a factor of 100 for better visualization). Similarly, ventilation map differences (C) and perfusion map differences (D) are illustrated to highlight the spatial differences between DMD and competing methods. Functional maps obtained with FD leads to stability issues in estimated amplitudes depending on ℓ; and maps obtained with MP indicate inconsistent estimation of amplitudes, as evident in the ventilation map for $\ell = 176$. In comparison, DMD displays consistent results in both ventilation and perfusion maps across all ℓ. 60

5.1 Workflow of the DMD MRI method. (**a**) Dynamic acquisitions are obtained during free-breathing to capture signal variations stemming from respiration and pulsation. (**b**) Lung structures are aligned using a non-rigid registration technique to enable the observation of regional parenchymal signal changes. Movements across measurements for a region (displayed with green line) before and after registration are also shown below acquisitions. (**c**) Registered time-series images are analysed using dynamic mode decomposition (DMD), and modes related to ventilation (displayed with blue boxes) and perfusion (displayed with red boxes) are identified. (**d**) Using these identified modes, ventilation and perfusion maps are calculated. Overall, functional maps can be obtained from dynamic acquisitions without the need for breathing manoeuvres or administration of contrast agents. 66

5.2 Exemplary magnitude images and frequency spectrums calculated from the acquisitions obtained with (**a**) Protocol A, and (**b**) Protocol B, from a CDH patient with left-sided hernia and ECMO treatment. The magnitude images are scaled to better visualize lung parenchyma. Both protocols are able to successfully detect frequency peaks associated with respiration ($\sim$ 0.35 Hz) and cardiac pulsation ($\sim$ 1.55 Hz). 69

5.3 Exemplary dominant modes obtained with the DMD analysis from measurements of a patient with left-sided herniation and ECMO treatment. Here, the dynamic images are obtained with Protocol A, and non-rigid registration is completed before the DMD analysis. The mode frequencies (f) and mode amplitudes (b) associated with the individual modes are also displayed overlaid on the modes. The DMD analysis identifies coherent spatiotemporal structures in the dynamic acquisitions, such as signal variations caused by respiration and pulsation, as well as secondary motions or harmonics. For this patient, modes related to pulmonary ventilation (mode with $f = 0.40$ Hz) and perfusion (mode with $f = 1.51$ Hz) were selected and used for the calculation of fractional ventilation and normalized perfusion maps. . 74

5.4 Exemplary fractional ventilation and normalized perfusion maps obtained through DMD MRI of a patient with right-sided herniation and without ECMO therapy obtained with (**a**) Protocol A, and (**b**) Protocol B. The maps are cropped to the region of interest for visualization purposes. Next to the maps, violin plots depict the distribution of functional values of each lung. For both protocols, differences between ipsilateral and contralateral lungs are discernible in both ventilation and perfusion maps, as well as the accompanying violin plots, which imply impaired lung function in the ipsilateral lung relative to the contralateral lung. 75

5.5 Pearsons correlation and Bland-Altman analyses of functional ratios obtained through DMD MRI with Protocol A and Protocol B. V_{Ratio} and Q_{Ratio} values obtained with two non-contrast-enhanced bSSFP protocols display a very strong correlation and a close agreement with each other without any systematic differences. 76

5.6 Representative magnitude images from bSSFP protocols, along with normalized perfusion, and fractional ventilation maps obtained through DMD MRI from a patient with left sided hernia and ECMO therapy. Additionally, a representative magnitude image and PBF map obtained from TWIST protocol for the same patient from a similar slice location are displayed. For visualization purposes, all functional maps are cropped to the region of interest. Overall, reductions in the ipsilateral lung can be observed visually, and can be confirmed by the resulting quantitative ratios (displayed overlaid on functional maps). Although the TWIST-based method can generate quantitative PBF maps, DMD MRI does not require the administration of contrast agents and is also capable of generating ventilation maps. 77

5.7 Pearsons correlation and Bland-Altman analyses between perfusion ratios obtained via TWIST (PBF_{Ratio}) and DMD MRI (Q_{Ratio}) for (**a**) Protocol A and (**b**) Protocol B. For both protocols, we observe a very strong correlation without any significant bias or systematic difference. (r, Pearsons correlation coefficient; RPC, reproducibility coefficient.) 78

List of Tables

2.1 List of some NMR-active nuclei. Data in the table are adapted from Brown et al., 2014. Relative abundance values are given for the human body with 1 M = 1 mol/L. A negative γ indicates that the magnetic moment is anti-parallel to the angular momentum. 6
2.2 List of approximate T_1 and T_2 relaxation times for various biological tissues at 1.5 T field strength. Data in the table are adapted from (Bernstein, King, and Zhou, 2004). *T_1 value for blood is given for arterial blood, whereas T_2 value is given for venous blood. 12
2.3 List of approximate T_1, T_2, and T_2^* relaxation times for lung parenchyma at various field strengths. Data in the table are adapted from (Nichols and Paschal, 2008; Yu, Xue, and Song, 2011; Campbell-Washburn et al., 2019). 28

3.1 Parenchymal SNR of registered images and CNR measurements obtained from functional maps for individual subgroups (SGs) and for both methods at 1.5T and 3T field strengths. Metrics are reported separately for each subgroup as mean±std across 5 subjects. 46
3.2 Parenchymal SNR and CNR measurements obtained from the combined measurements at 1.5T and 3T field strengths. For the combined SNR_L measurements, normalized registered images of individual subgroups were analyzed and weighted combined with respect to the estimated SNR. For the combined CNR measurements, individual functional maps (FD_V and FD_Q) were weighted combined with respected to estimated SNR and corrected for the number of breaths and heart beats per minute (f_V and f_Q), but were not quantified according to Equations 3.1 and 3.2 in order to avoid amplified signal levels in the air regions. Metrics are reported as mean±std across 5 subjects. 47
3.3 Coefficient of variation (CV in units of 10^{-2}) measurements of combined functional maps are reported at 1.5T and 3T field strengths. Metrics are reported for each combined functional map as mean±std across 5 subjects, * and ** denotes significant differences ($p < 0.05$) between respective groups. 47

4.1 Mean and standard deviation across different measurement lengths $\ell \in [50\ 250]$ of average ventilation and perfusion values estimated with FD, MP and DMD methods for all volunteers. The average functional values at each ℓ are calculated over ROIs encompassing lung parenchyma, and the values are scaled by a factor of 100 for better visualization of differences. 61

5.1 Patient demographics. 65
5.2 Relevant parameter list of two different bSSFP protocols used for imaging. *Voxel resolution with interpolation. 67

5.3 Quantitative measurements obtained from acquisition Protocol A. The average values are reported as mean ± standard deviation across patients. 68
5.4 Quantitative measurements obtained from acquisition Protocol B. The average values are reported as mean ± standard deviation across patients. 70
5.5 Mean fractional ventilation (V, scaled by a factor of 100 for better visualization) and normalized perfusion (Q) results calculated over ipsilateral (V_{Ipsi}, Q_{Ipsi}) and contralateral (V_{Cont}, Q_{Cont}) lungs from images obtained with Protocol A. Their ratios (V_{Ratio} and Q_{Ratio}) are also reported. The average values are reported as mean ± standard deviation across patients. 71
5.6 Mean fractional ventilation (V, scaled by a factor of 100 for better visualization) and normalized perfusion (Q) results calculated over ipsilateral (V_{Ipsi}, Q_{Ipsi}) and contralateral (V_{Cont}, Q_{Cont}) lungs from images obtained with Protocol B. Their ratios (V_{Ratio} and Q_{Ratio}) are also reported. The average values are reported as mean ± standard deviation across patients. 72
5.7 Perfusion parameters obtained through DCE-based TWIST protocol. . . 73

List of Abbreviations

ADC	**A**nalog to **D**igital **C**onverter
bSSFP	**B**alanced **S**teady **S**tate **F**ree **P**recession
CDH	**C**ongenital **D**iaphragmatic **H**ernia
CNR	**C**ontrast-to-**N**oise **R**atio
CSF	**C**erebro**s**pinal **F**luid
CT	**C**omputed **T**omography
DCE	**D**ynamic **C**ontrast **E**enhanced
DMD	**D**ynamic **M**ode **D**ecompoisition
ECMO	**E**xtra**c**orporeal **M**embrane **O**xygenation
EPI	**E**cho **P**lanar **I**maging
FD	**F**ourier **D**ecomposition
FWHM	**F**ull **W**idth at **H**alf **M**aximum
FSE	**F**ast **S**pin **E**cho
GRAPPA	**G**ene**r**alized **a**utocalibrating **p**artially **p**arallel **a**cquisition
GRE	**G**radient **E**cho
HP	**H**yper**p**olarized
MP	**M**atrix **P**encil
MR	**M**agnetic **R**esonance
MRI	**M**agnetic **R**esonance **I**maging
NMR	**N**uclear **M**agnetic **R**esonance
PREFUL	**P**hase-**RE**solved **FU**nctional **L**ung Imaging
RF	**R**adio **F**requency
ROI	**R**egion **O**f **I**nterest
SAR	**S**pecific **A**bsorption **R**ate
SE	**S**pin **E**cho
SENCEFUL	**SE**lf-gated **N**on-**C**ontrast-**E**nhanced **FU**nctional **L**ung
SNR	**S**ignal-to-**N**oise **R**atio
SPECT	**S**ingle **P**hoton **E**mission **C**omputerized **T**omography
SSFP	**S**teady **S**tate **F**ree **P**recession
TE	**E**cho **T**ime
TR	**R**epetition **T**ime
TWIST	**T**ime-resolved Angiography **Wi**th **S**tochastic **T**rajectories
UTE	**U**ltrashort **E**cho **T**ime
ZTE	**Z**ero **E**cho **T**ime

Chapter 1

Introduction

1.1 Motivation

Lung imaging plays a critical role in the diagnosis and monitoring of prevalent lung diseases. Alongside chest radiography, which serves as the most commonly employed initial screening method for chest abnormalities, and computed tomography (CT), which remains the preferred approach for cross-sectional and three-dimensional imaging of the lungs (Biederer, 2018), magnetic resonance imaging (MRI) is emerging as a viable alternative and a complementary method for the evaluation of pulmonary disorders. Indeed, it is the most recent modality to be integrated into clinical practice for lung imaging (Biederer et al., 2012a; Miller et al., 2014), and thereby holds a great potential in the assessment of pulmonary disorders.

Compared to other imaging modalities, MRI offers a crucial advantage owing to its capability of acquiring both structural and functional information in the same scan session (Biederer et al., 2012a; Bieri, 2013). While radionuclide-based scintigraphy and single-photon emission computed tomography (SPECT) can be utilized to obtain pulmonary functional information, capturing regional distribution of ventilation (V), perfusion (Q), and ventilation-to-perfusion (V/Q) mismatch, they lack the ability to obtain morphological information. On the other hand, CT-based measurements can provide structural information at high spatial resolutions, yet they are not capable of generating functional images (Biederer, 2018). While lung imaging using MRI remains challenging due to inherent low-proton density of lung tissue, the continuous motion of the lung, and very fast signal decay, with recent improvements in image quality and robustness, images with submillimetre resolution can be now acquired with MRI (Tiddens et al., 2018), and functional information can be obtained with and without the use of contrast agents (Bauman et al., 2009).

Moreover, current clinical evidence indicates that omitting functional scans is associated with a higher risk of misdiagnosis of lung diseases, such as pulmonary embolism caused by COVID-19 (Le Roux, Le Gal, and Salaun, 2020). However, safety concerns regarding the radiation exposure limits the application of radionuclide-based imaging methods as well as CT-based imaging; whereas recent evidence of gadolinium deposition limits the application of dynamic contrast enhanced MRI methods (Gulani et al., 2017). These limitations are particularly important for the imaging of children, where repeated radiation exposure or invasive administration of intravenous contrast agents remains a strong consideration (Walkup, Higano, and Woods, 2019). Additionally, in cases with chronic morbidities, regular examinations might be needed for the longitudinal assessment of these patients. As such, alternative methods for obtaining functional information without the radiation burden or contrast agents are of great importance, and MRI is set to become the preferred modality in cases where minimizing exposure to harmful ionizing radiation or contrast agents is of utmost importance.

To this end, several non-contrast-enhanced functional lung imaging methods have been proposed to evaluate regional distribution of ventilation and perfusion by exploiting periodic signal changes associated with respiration and cardiac pulsation (Bauman et al., 2009; Kjørstad et al., 2015). However, balanced steady state free precession (bSSFP) pulse sequence used for obtaining dynamic acquisitions in these techniques is known to be sensitive to the field inhomogeneities (Cukur, 2015). Moreover, Fourier decomposition and matrix pencil decomposition techniques used for spectrally analyzing the data suffer from the amplitude and frequency estimation issues (Bondesson et al., 2019). Lastly, these non-contrast-enhanced MRI methods for obtaining regional ventilation and perfusion information have not been investigated in CDH patients.

The aims of this thesis are to improve the robustness of non-contrast-enhanced functional lung imaging and to demonstrate its feasibility in pediatric patients. To achieve these objectives, a multiple-acquisition bSSFP method with phase-cycling scheme is introduced to improve the bSSFP sequence's robustness against commonly observed field inhomogeneity artifacts, and a novel post-processing method is developed for accurately estimating pulmonary ventilation and perfusion related signal changes in dynamic acquisitions. Furthermore, the non-contrast-enhanced MRI acquisitions are demonstrated as a viable option for functional lung imaging in 2-year-old children after congenital diaphragmatic hernia repair.

1.2 Outline

This thesis is written cumulatively. As such, Chapters 3, 4, and 5 are self-contained scientific studies that have distinct sections dedicated to introduction, materials and methods, discussion, and conclusion.

Chapter 2 serves as an introduction to the fundamentals of nuclear magnetic resonance (NMR) and the principles of magnetic resonance imaging (MRI). Additionally, it offers an overview of pulmonary physiology with a special focus on congenital diaphragmatic hernia (CDH), followed by a brief overview of proton MRI of the lung.

In Chapter 3, an image acquisition technique based on phase-cycled bSSFP imaging is presented to improve the robustness against field inhomogeneity artifacts. This technique is demonstrated on healthy volunteers at 1.5T and 3T field strengths, where results indicate significantly improved ventilation map homogeneity at both field strengths.

Chapter 4 presents a robust post-processing technique based on dynamic mode decomposition (DMD) to obtain pulmonary functional maps robustly and accurately from dynamic acquisitions. This technique is demonstrated on healthy volunteers at 1.5T field strength and it displays reduced variations in estimated amplitudes compared to Fourier decomposition and matrix pencil decomposition methods.

Chapter 5 showcases the application of DMD technique to dynamic bSSFP acquisitions obtained at 1.5T field strength from 2-year-old CDH patients after patch repair. Here, ventilation and perfusion maps are obtained successfully without the need for ionizing radiation or intravenous contrast agents. Moreover, the pulmonary perfusion results obtained with the DMD method are demonstrated to correlate very strongly with perfusion parameters obtained using dynamic contrast-enhanced MRI.

Finally, Chapter 6 provides an overarching summary of this thesis, while Chapter 7 outlines future research directions.

1.3 Citation of Previous Publications

Several chapters of this thesis have already been published or are currently submitted for publication. The citations for these chapters are:

> Chapter 3: Efe Ilicak, Safa Ozdemir, Lothar R. Schad, Meike Weis, Stefan o. Schoenberg, Frank G. Zöllner, Jascha Zapp. "Phase-cycled balanced SSFP imaging for non-contrast-enhanced functional lung imaging." *Magnetic Resonance in Medicine.* 2022 Oct; 88(4): 1764-1774. doi:10.1002/mrm.29302.
>
> Chapter 4: Efe Ilicak, Safa Ozdemir, Jascha Zapp, Lothar R. Schad, Frank G. Zöllner. "Dynamic Mode Decomposition of Dynamic MRI for Assessment of Pulmonary Ventilation and Perfusion." *Magnetic Resonance in Medicine.* 2023 Aug; 90(2): 761- 769. doi:10.1002/mrm.29656.
>
> Chapter 5: Efe Ilicak[1], Greta Thater[1], Safa Ozdemir, Jascha Zapp, Lothar R. Schad, Stefan O. Schoenberg, Frank G. Zöllner[2], Meike Weis[2]. "Functional lung imaging of 2-year-old children after congenital diaphragmatic hernia repair using dynamic mode decomposition." *European Radiology*. Submitted on 19.04.2023.

---

[1] Efe Ilicak and Greta Thater contributed equally to this work.

[2] Frank G. Zöllner and Meike Weis contributed equally to this work.

Chapter 2

Theoretical Background

The present chapter covers the fundamentals of nuclear magnetic resonance (NMR) and the principles of magnetic resonance imaging (MRI), followed by an overview of pulmonary physiology, with a special focus on congenital diaphragmatic hernia (CDH), as well as a review of the proton MRI of the lung. A more thorough explanation of NMR and MRI can be found in (Brown et al., 2014; Zhi-Pei Liang and Lauterbur, 2000). A more detailed overview of pulmonary physiology can be found in (West and Luks, 2016; Michael A. Grippi et al., 2015).

2.1 Nuclear Magnetic Resonance

The purpose of this section is to provide an overview of fundamentals regarding nuclear magnetic resonance. Although a rigorous description of the MR physics requires quantum mechanics, the underlying principles of MRI can be described using classical vector models, because MRI deals with the collective behavior of a large ensemble of nuclei present in macroscopic scale (Nishimura, 1996; Zhi-Pei Liang and Lauterbur, 2000).

2.1.1 Nuclear Spin

Magnetic resonance imaging is possible due to a physical phenomenon called *nuclear magnetic resonance* (NMR). A fundamental property of nuclei is that, nuclei with either an odd atomic number or an odd mass number (e.g., hydrogen (^{1}H) with one proton) possess a nuclear spin angular momentum $\vec{J}$, also called *spin*. Although nuclear spin is truly characterized by quantum mechanics, these nucleons can be visualized as spinning charged spheres.

A nucleus with nonzero spin creates a magnetic field around it, giving rise to a small magnetic moment $\vec{\mu}$. The magnetic moment is related to spin angular momentum by:

$$\vec{\mu} = \gamma \vec{J} \qquad \text{rad/s/T} \tag{2.1}$$

where γ is the *gyromagnetic ratio* and depends on the particle or nucleus. A related constant is 'gamma-bar', and defined as $\bar{\gamma} = \gamma/2\pi$ (MHz/T). The magnitude of the magnetic moment is $|\vec{\mu}| = \gamma\hbar\sqrt{I(I+1)}$, where $\hbar$ is Planck's constant divided by 2π and I is the nuclear spin quantum number (Zhi-Pei Liang and Lauterbur, 2000). The spin quantum number takes half-integer or integer values (e.g., $I = 0, 1/2, 1, 3/2, ...$) and a nucleus is NMR-active only for $I \neq 0$. A spin system with $I = 1/2$ (e.g., ^{1}H, ^{13}C, ^{19}F, and ^{31}P nuclei) is called a spin-1/2 system. Properties of some NMR-active nuclei are listed in Table 2.1.

TABLE 2.1: List of some NMR-active nuclei. Data in the table are adapted from Brown et al., 2014. Relative abundance values are given for the human body with 1 M = 1 mol/L. A negative γ indicates that the magnetic moment is anti-parallel to the angular momentum.

Nucleus	Spin I	γ (MHz/T)	Abundance
^{1}H	1/2	42.58	88 M
^{17}O	5/2	-5.77	17 mM
^{19}F	1/2	40.08	4 μM
^{23}Na	3/2	11.27	80 mM
^{31}P	1/2	17.25	75 mM

Although the magnitude of $\vec{\mu}$ is certain regardless of the conditions, there is no preferred orientation in the absence of an external magnetic field due to thermal random motion. Therefore, in the absence of an external magnetic field, the randomly oriented nuclear spins cancel each other out and no net magnetic field exists around a macroscopic object. However, in the presence of an external magnetic field, the spins tend to align in the direction of this field and become macroscopically magnetized. This direction of applied field is conventionally called the z-direction or *longitudinal* direction, and the external magnetic field is expressed in laboratory frame as:

$$\vec{B_0} = B_0\,\vec{k} \tag{2.2}$$

Based on the quantum model, a magnetic moment vector can point in one of a discrete set of orientations. Accordingly, in the presence of a B_0 field, the z-component of $\vec{\mu}$ is given by (Zhi-Pei Liang and Lauterbur, 2000):

$$\mu_z = \gamma m_I \hbar \tag{2.3}$$

where m_I is called the magnetic quantum number and $m_I = \{-I, -I+1, ..., I\}$. For a spin-1/2 system, $I = 1/2$ and $m_I = \pm 1/2$, this implies that magnetization can take one of two possible orientations relative to the z-direction. In particular, it can be $\theta = 54.74°$ off z-direction indicating pointing up (*spin up* or *parallel*), which is the low energy state, or it can be $\theta = 125.26°$ off z-direction indicating pointing down (*spin down* or *antiparallel*), as illustrated in Figure 2.1.

Assuming $\vec{\mu}$ is a classical magnetic moment vector without mutual interactions, it would experience a torque from the external magnetic field, which is given by $\vec{\mu} \times B_0\,\vec{k}$. This is equivalent to the rate of change in its angular momentum and can be described as:

$$\frac{d\vec{J}}{dt} = \vec{\mu}\ \times B_0\,\vec{k} \tag{2.4}$$

Using the relation between magnetic moment and spin angular momentum in Equation 2.1 yields:

$$\frac{d\vec{\mu}}{dt} = \gamma\vec{\mu} \times B_0\vec{k} \tag{2.5}$$

With the initial magnetization conditions of $\mu_{xy}(0)$ and $\mu_z(0)$, the solution to the Equation 2.5 is expressed by:

$$\begin{cases} \mu_{xy}(t) = \mu_{xy}(0)e^{-i\gamma B_0 t} \\ \mu_z(t) = \mu_z(0) \end{cases} \tag{2.6}$$

which describes a precession of $\vec{\mu}$ around B_0 with an angular frequency:

$$\omega_0 = \gamma B_0 \tag{2.7}$$

which is known as the *Larmor frequency*, and the precession occurs in the clockwise direction when viewed against the direction of the magnetic field, as illustrated in Figure 2.1.

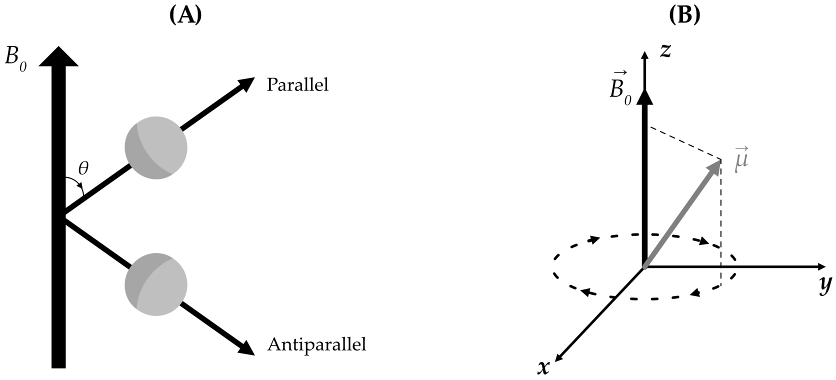

FIGURE 2.1: (A) Nuclear magnetic moment vectors aligned in the direction of an external magnetic field. (B) The precession of the magnetic moment vector is clockwise when observed against the direction of the magnetic field.

2.1.2 Macroscopic Magnetization

When an external static magnetic field $\vec{B}_0$ is applied to a specific spin system within a volume of material, the collective behavior of the spin system can be modeled using a macroscopic (bulk) magnetization vector $\vec{M}$, which is the vector sum of all the individual magnetic moments. Let $\vec{\mu}_n$ be the magnetic moment of the n^{th} nuclear spin, and N_S be the total number of spins in the object. Then, the macroscopic magnetization can be defined as:

$$\vec{M} = \sum_{n=1}^{N_S} \vec{\mu}_n \tag{2.8}$$

Considering a spin-1/2 system, $\vec{\mu}_n$ can take either spin-up or spin-down state. Spins in different states possess different energy of interaction with $\vec{B}_0$, which is given based on quantum theory by (Zhi-Pei Liang and Lauterbur, 2000):

$$E = -\vec{\mu} \cdot \vec{B}_0 = -\mu_z B_0 = -\gamma \hbar m_I B_0 \tag{2.9}$$

Accordingly, for spin-up systems with $m_I = 1/2$, this would yield:

$$E_\uparrow = -\frac{1}{2}\gamma \hbar B_0 \tag{2.10}$$

and for spin-down systems with $m_I = -1/2$, this would yield:

$$E_{\downarrow} = \frac{1}{2}\gamma\hbar B_0 \tag{2.11}$$

Note that the energy levels indicate that the spin-up state is the lower energy state, whereas the spin-down state is the higher energy state (Zhi-Pei Liang and Lauterbur, 2000); and the energy difference between the states is:

$$\Delta E = E_{\downarrow} - E_{\uparrow} = \gamma\hbar B_0 = \hbar\omega_0 \tag{2.12}$$

The phenomenon of splitting in the nuclear energy levels is referred to as the *Zeeman effect*, as illustrated in Figure 2.2. Note that the frequency associated with transition between the states in Equation 2.12 is the Larmor frequency.

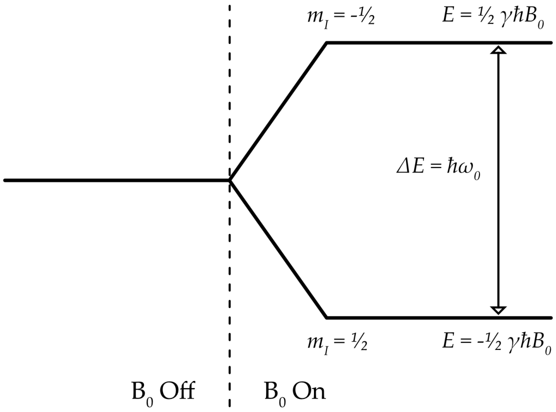

FIGURE 2.2: Zeeman splitting for a spin-1/2 system. The spin in the spin-up (parallel) state is in the lower energy state.

The ratio of two spin populations is related to their energy difference and this can be defined according to Boltzmann distribution as:

$$\frac{N_{\uparrow}}{N_{\downarrow}} = exp\left(\frac{\Delta E}{kT}\right) \tag{2.13}$$

where $N_{\uparrow}$ and $N_{\downarrow}$ is the number of spins in the spin-up an spin-down states, respectively, k is the Boltzmann constant (1.38×10^{-23} J/K), and T is the absolute temperature. Using first order Taylor series expansion, Equation 2.13 can be approximated as:

$$\frac{N_{\uparrow}}{N_{\downarrow}} \approx 1 + \frac{\gamma\hbar B_0}{kT} \tag{2.14}$$

and subsequently,

$$N_{\uparrow} - N_{\downarrow} \approx N_S \frac{\gamma\hbar B_0}{2kT} \tag{2.15}$$

Note that Equation 2.15 indicates an excess of spins in the spin-up state (with lower energy and higher stability) (Zhi-Pei Liang and Lauterbur, 2000); therefore an uneven spin distribution between two spin systems. At human body temperature ($T \approx 310$ K) and for a magnetic field strength $B_0 = 1$ T, the ratio of spins is about 1.0000066 = 6.6 parts per million (ppm). This implies that a fractional population difference $(N_{\uparrow} - N_{\downarrow})/N_S \approx 3 \times 10^{-6}$ or approximately an excess of 3 out of 10^6

spins. Nevertheless, macroscopically, this difference generates an observable magnetization.

The resulting macroscopic magnetization vector $\vec{M}$ can be written as:

$$\begin{aligned}\vec{M} &= M_x\,\vec{i} + M_y\,\vec{j} + M_z\,\vec{k} \\ &= \left(\sum_{n=1}^{N_S} \mu_{x,n}\right)\vec{i} + \left(\sum_{n=1}^{N_S} \mu_{y,n}\right)\vec{j} + \left(\sum_{n=1}^{N_S} \mu_{z,n}\right)\vec{k}\end{aligned} \tag{2.16}$$

with the macroscopic magnetization vector being projected onto x-, y-, and z-axes; $\vec{i}$, $\vec{j}$ and $\vec{k}$ are the unit vectors. Here, note that the projections onto x- and y-axes are zero due to the random phase (Zhi-Pei Liang and Lauterbur, 2000). Therefore, the macroscopic magnetization in Equation 2.16 can be simplified using Equation 2.3 as:

$$\vec{M} = \left(\sum_{n=1}^{N_\uparrow} \frac{1}{2}\gamma\hbar - \sum_{n=1}^{N_\downarrow} \frac{1}{2}\gamma\hbar\right)\vec{k} = \frac{1}{2}(N_\uparrow - N_\downarrow)\gamma\hbar\vec{k} \tag{2.17}$$

Equation 2.17 implies that the macroscopic magnetization vector has the same direction as $\vec{B}_0$, and using Equation 2.15, it can be shown that its magnitude is:

$$|\vec{M}| = M_z^0 = \frac{\gamma^2\hbar^2 B_0 N_S}{4kT} \tag{2.18}$$

for a spin-1/2 system. For a spin-I system, it is given as (Zhi-Pei Liang and Lauterbur, 2000):

$$M_z^0 = \frac{\gamma^2\hbar^2 B_0 N_S \mathrm{I(I{+}1)}}{3kT} \tag{2.19}$$

Here, note that the magnitude of $\vec{M}$ depends on B_0 and N_S; indicating that both stronger magnets and higher number of spins produce a larger magnitude.

2.1.3 RF Excitation

In the presence of a static external $\vec{B}_0$ field, a macroscopic magnetization $\vec{M}$ is generated along the direction of the field. However; at thermal equilibrium, the transverse component of the magnetization, $\vec{M}_{xy}$, is zero due to the random phase. To generate a detectable signal, the magnetization must be tipped away from the $\vec{B}_0$ direction, such that it produces a detectable changing magnetic flux in the receiver coils (via Faraday's law of induction). To this end, a *radio frequency* (RF) magnetic pulse denoted as $\vec{B}_1$ tuned to the resonant frequency is applied perpendicularly to $\vec{B}_0$. Even though weak RF fields are used on human imaging systems, they are still able to rotate the magnetization away from its alignment with $\vec{B}_0$, and this rotation is most efficient when the resonance condition is satisfied.

According to Planck's law, the energy carried by the electromagnetic radiation of frequency ω_{rf} can be defined as:

$$E_{rf} = \hbar\omega_{rf} \tag{2.20}$$

To induce a coherent transition of spins between the energy states (Zhi-Pei Liang and Lauterbur, 2000), the radiation energy must match the energy difference $\Delta E = \hbar\omega_0$ (Equation 2.12). Accordingly,

$$\omega_{rf} = \omega_0 \tag{2.21}$$

Equation 2.21 implies that the $\vec{B_1}$ field is most efficient when the applied RF frequency matches the Larmor frequency, and this condition is known as the resonance condition.

Typically, the $\vec{B_1}$ field (RF pulse) has a very short duration and oscillates in the RF range. Assuming that the carrier frequency is close to Larmor frequency, it can be characterized as (Zhi-Pei Liang and Lauterbur, 2000):

$$\vec{B_1} = B_1^e(t)[\cos(\omega_{rf}t + \phi)\vec{i} - \sin(\omega_{rf}t + \phi)\vec{j}] \tag{2.22}$$

where B_1^e is the envelope function, ω_{rf} is the carrier frequency, and ϕ is the phase angle. For brevity, $\vec{B_1}$ in Equation 2.22 can also be written in the complex exponential notation as:

$$\vec{B_1} = B_1^e(t)e^{-i(\omega_{rf}t+\phi)} \tag{2.23}$$

A useful definition is the *flip angle*, which describes the rotation angle of the magnetization with respect to the z-axis in the rotating frame of reference[1]. The flip angle depends on the magnitude of the RF pulse as well as its duration (τ) and is given by:

$$\alpha = \int_0^\tau \gamma B_1^e(t)dt \tag{2.24}$$

Following the excitation with the RF pulse, the magnetization will continue to precess about the z-axis. This transverse magnetization induces a change in the flux Φ_B in the receiver coils via Faraday's law of induction, thereby generates a small electromotive force (EMF) ϵ:

$$\epsilon = -\frac{d\Phi_B}{dt} = -\frac{d}{dt}\int_{vol} \vec{B^r} \cdot \vec{M}(r,t)dt \tag{2.25}$$

where $\vec{B^r}$ is the laboratory frame magnetic field at location r, produced by a unit current flowing in the receive coil. The resulting electromotive force, or voltage, lays the foundation for the detection of MR signal detection.

2.1.4 Free Precession and Relaxation

After a spin has been perturbed from the thermal equilibrium via an RF excitation (e.g., an RF pulse with flip angle of 90° would rotate the magnetization to lie completely in the x-y plane), it will return to its equilibrium state (along the z-axis) given the external force is removed and sufficient time has passed. This process is characterized by the precession of $\vec{M}$ around B_0, and is called *free precession*.

Furthermore, note that this process implies a decay in the transverse component of the magnetization (M_{xy}), called *transverse relaxation*, and a regrowth in the longitudinal component of magnetization (M_z), called *longitudinal relaxation*. Both of these relaxations are attributed to the existence of time-dependent microscopic magnetic fields that surround a nucleus (Zhi-Pei Liang and Lauterbur, 2000), and two important time constants, T_1 and T_2, characterize this return to the equilibrium state (Nishimura, 1996).

---

[1] The rotating frame of reference is a coordinate system that rotates clockwise along a fixed axis with an angular frequency. A *Larmor-rotating frame* is a rotating frame that rotates in the transverse plane with Larmor frequency, and x', y', and z' are used to denote the three orthogonal axes in this rotating frame.

Longitudinal Relaxation

The longitudinal relaxation, or *spin-lattice relaxation*, is characterized in the Larmor-rotating frame as the following process:

$$\frac{dM_{z'}}{dt} = -\frac{M_{z'} - M_z^0}{T_1} \tag{2.26}$$

Solving Equation 2.26 results in:

$$M_{z'}(t) = M_z^0(1 - e^{-t/T_1}) + M_{z'}(0_+)e^{-t/T_1} \tag{2.27}$$

where, $M_{z'}(0_+) = M_z^0 \cos\alpha$ is the longitudinal magnetization immediately after the RF pulse, and M_z^0 is the longitudinal magnetization at the thermal equilibrium.

The T_1 time constant characterizes the return of magnetization to thermal equilibrium in the direction of B_0 (Figure 2.3), and involves an energy exchange between the nuclei and the surrounding lattice. This process is due to the preference of a lower energy state, and the spins transfer energy to their environment in the form of heat. Here, note that the T_1 time constant is defined as the time interval for $M_{z'}$ to regain approximately 63% of its thermal equilibrium value ($M_{z'}(T_1) \approx 63\% M_z^0$), and it is dependent on the field strength.

Transverse Relaxation

The transverse relaxation, or *spin-spin relaxation*, is characterized in the Larmor-rotating frame as the following process:

$$\frac{dM_{x'y'}}{dt} = -\frac{M_{x'y'}}{T_2} \tag{2.28}$$

Solving Equation 2.28 results in:

$$M_{x'y'}(t) = M_{x'y'}(0_+)e^{-t/T_2} \tag{2.29}$$

where, $M_{x'y'}(0_+) = M_z^0 \sin\alpha$ is the transverse magnetization immediately after the RF pulse.

The T_2 time constant characterizes the decay of the transverse magnetization, and involves an energy exchange between neighboring spins. Microscopically, the Brownian motion causes fluctuations in the local magnetic fields, leading to a broadening of the spins' resonant frequencies. The frequency variations over time cause a transverse decay due to spins losing their relative phase coherence (*dephasing*). Here, note that the T_2 time constant is defined as the time interval for $M_{x'y'}$ to fall to approximately 37% of its initial value ($M_{x'y'}(T_2) \approx 37\% M_{x'y'}(0_+)$).

The T_1 and T_2 relaxation times depend on tissue composition, structure, and surroundings. In biological tissues, T_1 is longer than T_2, and relaxation times for ^{1}H nuclei in various biological tissues are given in Table 2.2.

In reality, the transverse magnetization decays more rapidly than T_2 (Figure 2.3). This is due to local and static inhomogeneities in the magnetic field. To characterize the signal decay, T_2^* time constant is commonly used, which satisfies $T_2 > T_2^*$ (Prince and Links, 2015). In cases where the field inhomogeneity follows a Lorentzian spin density distribution (Zhi-Pei Liang and Lauterbur, 2000), the relationship between

TABLE 2.2: List of approximate T_1 and T_2 relaxation times for various biological tissues at 1.5 T field strength. Data in the table are adapted from (Bernstein, King, and Zhou, 2004). *T_1 value for blood is given for arterial blood, whereas T_2 value is given for venous blood.

Tissue	T_1 (ms)	T_2 (ms)
Brain white matter	790	90
Brain gray matter	920	100
Cerebrospinal fluid (CSF)	4000	2000
Blood*	1200	50
Liver	490	40
Lung	830	80
Myocardium	870	60
Skeletal muscle	870	50
Lipids	260	80

the transverse relaxation constants is:

$$\frac{1}{T_2^*} = \frac{1}{T_2} + \frac{1}{T_2'} \tag{2.30}$$

where $1/T_2' = \gamma \Delta B_0$, and the loss of transverse magnetization due to T_2' is recoverable (Brown et al., 2014).

Overall, the dephasing causes a loss of coherence in the RF wave induced by the spin system, and therefore a loss in the received signal. The resultant time signal detected in the receiver coil is called a *free induction decay* (FID).

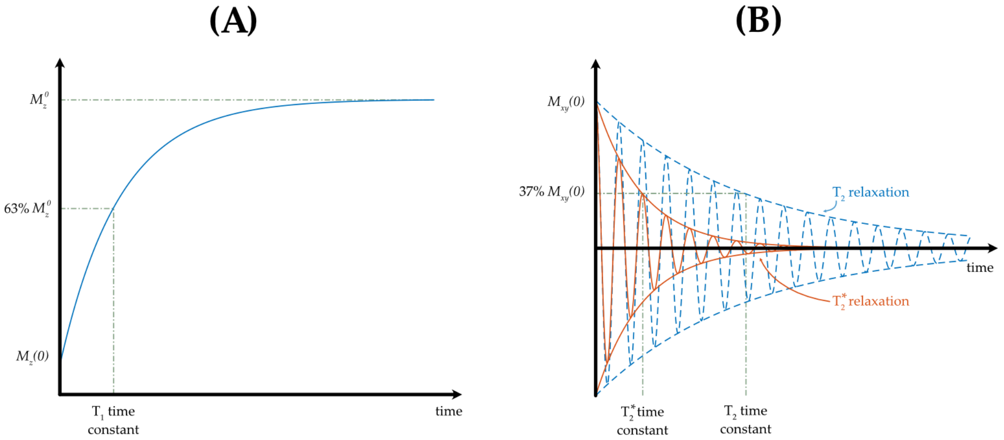

FIGURE 2.3: (A) Longitudinal (T_1) relaxation process. (B) Transverse (T_2 and T_2^*) relaxation processes.

2.1.5 Bloch Equation

In general, the time-dependent behavior of nuclear magnetization $\vec{M}$ in the presence of magnetic field $\vec{B}(t)$ can be described by the *Bloch equation*, given by:

$$\frac{d\vec{M}}{dt} = \gamma \vec{M} \times \vec{B} - \frac{M_x\vec{i} + M_y\vec{j}}{T_2} - \frac{(M_z - M_z^0)\vec{k}}{T_1} \tag{2.31}$$

which can be expressed as the following in the rotating frame (Zhi-Pei Liang and Lauterbur, 2000):

$$\frac{\partial \vec{M}}{\partial t} = \gamma \vec{M}_{rot} \times \vec{B}_{eff} - \frac{M_{x'}\vec{i'} + M_{y'}\vec{j'}}{T_2} - \frac{(M_{z'} - M_z^0)\vec{k'}}{T_1} \tag{2.32}$$

where $\vec{M}_{rot} = R_z(\omega t)\vec{M}$, is the magnetization in the rotating frame; R_z denotes the rotation matrix in the clockwise direction; $\vec{B}_{eff} = \vec{B}_{rot} + \vec{\omega}/\gamma$, is the effective magnetic field; and $\vec{B}_{rot} = R_z(\omega t)\vec{B}$.

Note that the Bloch equation above states that, when the relaxation terms are ignored, the time rate of change of $\vec{M}$ is proportional to the cross-product $\vec{M} \times \gamma\vec{B}$. Since the cross-product gives a vector that is perpendicular to $\vec{M}$ and $\vec{B}$, the rate of change will be also perpendicular to these fields, implying the angle between $\vec{M}$ and $\vec{B}$ does not change. Recalling Equation 2.23 and assuming $\phi = 0$ with B_1^e as rectangular function with amplitude B_1 and duration τ would yield a $\vec{B}_1(t)$ field in the direction of x' in the rotating frame. This excitation would cause the precession of $\vec{M}$ in the clockwise direction in the y'-z' plane, as illustrated in Figure 2.4. This type of motion is called *forced precession* and can be derived using the Bloch equation. Equivalently, this evolution can be visualized as a spiral from the z-axis to x-y plane in clockwise orientation in the laboratory frame as illustrated in Figure 2.4.

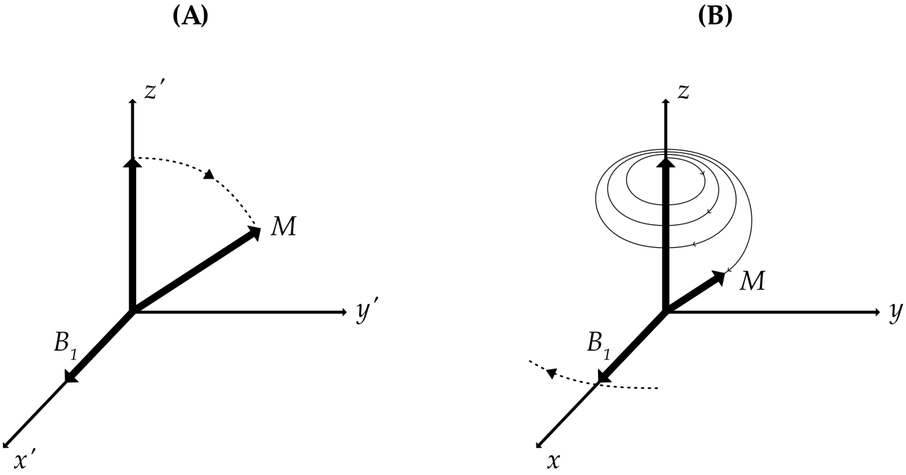

FIGURE 2.4: (A) In response to a rotating RF field, the magnetization vector $\vec{M}$ precesses around the x'-axis in the rotating frame. (B) In the laboratory frame, the actual motion of $\vec{M}$ is a spiral.

In MR imaging, $\vec{B}$ consists of three different magnetic fields (Nishimura, 1996): first, the main static field, $\vec{B_0}$; second, the radio frequency fields, $\vec{B_1}(t)$ used for excitation; and third, gradient fields, $\vec{G}(t)$ that are used for spatial encoding.

2.1.6 Gradient Fields

As evident from Larmor equation (Equation 2.7), when spins from a sample of interest are in a static magnetic field B_0 in the z-direction, then all of the spins in the sample will possess the same resonance frequency $\omega_0 = \gamma B_0$. Since the RF pulses can only be frequency selective and the RF coil hardware encompasses the entire region of interest, it is not possible to excite a selected portion of the object. Therefore, it would not be possible to distinguish between generated signals coming from different spatial locations.

In order to make RF pulses spatially selective, it is necessary to introduce a spatially-dependent magnetic field in addition to B_0. This is achieved by creating a gradient field $\vec{G}$ via gradient coils, which create temporary changes in the magnitude of B_0. In MRI systems there are usually three orthogonal gradient coils to encompass each of the physical x, y, and z-directions, and the respective gradient field magnitudes are denoted by G_x, G_y, and G_z. When all three of the gradients coils are utilized, the main field is given by:

$$\vec{B} = (B_0 + G_x x + G_y y + G_z z)\,\vec{k} \tag{2.33}$$

One important remark from Equation 2.33 is that the gradient coils do not change the direction of the magnetic field but they change the magnitude of the field along one axis (e.g., $G_x = dB/dx$). Another important remark is that the resonant frequency of the nuclei changes instantaneously when the field strength changes, and the change in frequency is proportional to the applied field strength (Nishimura, 1996).

2.1.7 Off-Resonance Sources

Larmor equation (Equation 2.7) states the resonance frequency depends on the gyromagnetic ratio and the strength of magnetic field. Here, it might be assumed that the Larmor frequency is constant for a given spin system, since the B_0 field is supposed to have a constant magnitude and the γ is nuclei specific. However, in practice, a spin system can display a range of resonance frequencies, due to three main reasons: main field inhomogeneities, susceptibility induced field variations, and chemical shift effects (Nishimura, 1996). These deviations from the resonant frequency are often referred as *off-resonance* conditions.

In MR imaging applications, the magnet design and calibrations allow very homogeneous main fields, and with the use of auxiliary *shim coils*, inhomogeneities can be kept under a few ppm over a 30 cm diameter spherical volume (Brown et al., 2014).

Magnetic susceptibility refers to a material property that changes the magnetic field inside the material, relative to the surrounding field. Even when a sample is placed in a perfectly homogeneous external magnetic field, resonant frequency differences may exist due to sample induced B_0 variations arising from the differences in bulk magnetic susceptibility χ within the sample. The field inhomogeneity depends on the geometry and susceptibility differences between materials, and the magnetic field in presence of susceptibility can be modeled as (Prince and Links, 2015):

$$\hat{B}_0 = B_0(1 + \chi) \tag{2.34}$$

Materials are categorized as: diamagnetic for $\chi < 0$, which slightly decrease the field (e.g., water); paramagnetic for $\chi > 0$ which slightly increase the field (e.g., air); ferromagnetic for $\chi \gg 0$ (e.g., iron) which strongly increase the field. Due to the abundance of water (diamagnetic) in tissues, the body is mostly diamagnetic (Brown et al., 2014). In MR imaging applications, the resultant inhomogeneity is most severe at tissue boundaries, such as air-tissue boundaries in the lung parenchyma.

Chemical shift refers to a change in the Larmor frequency due to the different chemical environments nuclei are attached to in a chemically heterogeneous sample. Since each nucleus of a molecule is surrounded by orbiting electrons with their own weak magnetic fields, these electrons can shield the nucleus to the effects of main magnetic field to a varying degree. As a result, the effective magnetic field observed by the nucleus is given by:

$$\hat{B}_0 = B_0(1 - \delta) \tag{2.35}$$

where δ is the shielding constant. Accordingly, the resonance frequency for the nucleus is:

$$\hat{\omega}_0 = \omega_0 - \Delta\omega = \omega_0(1 - \delta) = \gamma B_0(1 - \delta) \tag{2.36}$$

Chemical shift is usually on the order of a few ppm. A well known example is the ^{1}H nuclei in fat (CH_2), which are shifted down by 3.35 ppm from those in water (H_2O); which at 1.5T, corresponds to a shift of Larmor frequency by -214 Hz.

2.2 Magnetic Resonance Imaging

2.2.1 Signal Equation and *k*-Space

In MRI systems, the receive coil is designed to detect flux changes in the transverse plane. Assuming uniform receiver coil sensitivity for the entire volume, the received time signal $s_r(t)$ would be derived from the contributions of all precessing transverse magnetization in the volume, which can be written as (Nishimura, 1996):

$$\begin{aligned} s_r(t) &= \int_{vol} M(r,t)\, dV \\ &= \int_x \int_y \int_z M(x,y,z,t)\, dx\, dy\, dz \end{aligned} \tag{2.37}$$

The received signal from the excited plane can be written as:

$$s(t) = \int_x \int_y m(x,y) e^{-i2\pi[k_x(t)x + k_y(t)y]}\, dx\, dy \tag{2.38}$$

with

$$\begin{aligned} k_x(t) &= \gamma \int_0^t G_x(\tau)\, d\tau \\ k_y(t) &= \gamma \int_0^t G_y(\tau)\, d\tau \end{aligned} \tag{2.39}$$

and is commonly referred to as *signal equation*. The signal equation states that the received baseband signal from a plane is the integral of magnetization multiplied by a spatially-dependent phase factor. Assuming that linear gradient fields are applied, the resultant phase modulation would also vary linearly. Furthermore, note that the double integral in the signal equation can be interpreted as a 2D Fourier transform of $m(x,y)$:

$$M(k_x, k_y) = \int_x \int_y m(x,y) e^{-i2\pi(k_x x + k_y y)}\, dx\, dy \tag{2.40}$$

therefore indicating the following relationship:

$$s(t) = M\left(k_x(t), k_y(t)\right) \tag{2.41}$$

As indicated by Equation 2.41, at any given time t, *s(t)* depends on the 2D Fourier transform of $m(x,y)$ at some spatial frequency (Nishimura, 1996). In MRI literature, the Fourier space is usually referred to as k-space[2]. As such, the recorded signal $s(t)$ maps the trajectory through k-space as determined by the time integrals of the applied gradients.

2.2.2 Signal Localization

In practice, it is necessary to differentiate signals coming from different parts of an object of interest. The main types of spatial localization methods are *selective excitation/reception* and *spatial encoding*. In both methods, localization is achieved using the gradient fields to encode spatial position by changing the Larmor frequency and the phase of the transverse magnetization.

Slice Selection

In MRI, it is possible to excite and receive signal from a selected slice (*2D imaging*) or a volume (*3D imaging*). In 2D imaging, *slice selection* is performed using a gradient field and a shaped RF pulse to selectively excite spins in a desired slice. Recall from Section 2.1.6 that a linear gradient field is defined as a magnetic field that points in the direction of z-axis with linearly varying magnitude along a selected gradient direction, μ_G. As such, the slice selection gradient can be denoted as:

$$G_{ss} = (G_x, G_y, G_z) = G_{ss}\mu_G \tag{2.42}$$

Without the loss of generality, consider a rectangular spatial selection function along z-direction centered at z_0 with slice thickness Δz:

$$p_s(z) = \sqcap\left(\frac{z - z_0}{\Delta z}\right) \tag{2.43}$$

This would necessitate the application of $G_{ss} = (0, 0, G_z)$, which yields a Larmor frequency that is a function of z:

$$\omega(z) = \omega_0 + \gamma G_z z \tag{2.44}$$

or

$$\begin{aligned} f(z) &= f_0 + \gamma\!\!\!- G_z z \\ &= \gamma\!\!\!- (B_0 + G_z z) \end{aligned} \tag{2.45}$$

Subsequently, the desired frequency selection function becomes:

$$p(f) = \sqcap\left(\frac{f - f_c}{\Delta f}\right) \tag{2.46}$$

where $f_c = f_0 + \gamma\!\!\!- G_z z_0$ is the RF center frequency, and $\Delta f = \gamma\!\!\!- G_z \Delta z$ is the RF frequency range, and is illustrated in Figure 2.5. The RF center frequency is related to excitation frequency as $\omega_{rf} = 2\pi f_c$. Accordingly, by setting three parameters (z-gradient strength, RF center frequency, and RF frequency range), it is possible to control both the slice position z_0 and slice thickness Δz.

---

[2] This convention arises from physics literature, where the wave number k represents a spatial frequency (Prince and Links, 2015).

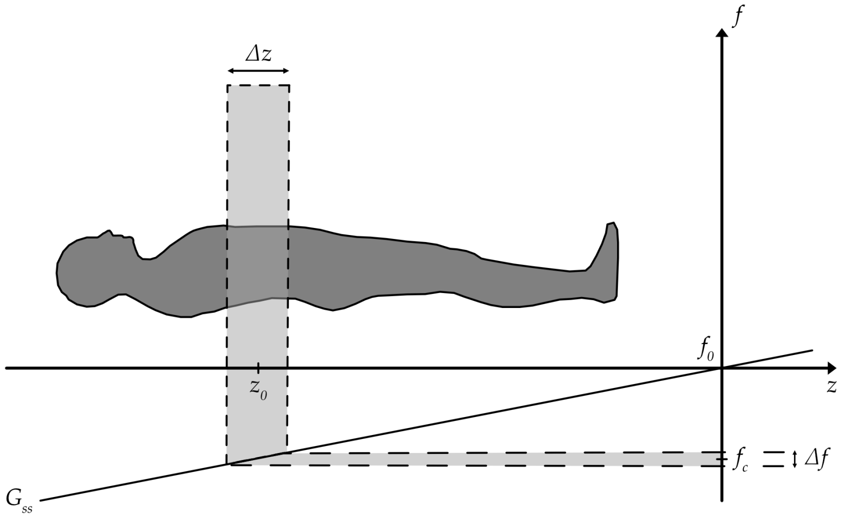

FIGURE 2.5: Desired slice is selected by application of a slice selection gradient and excitation with an appropriate RF pulse.

Spatial Information Encoding

Following the activation of a region by a selective or a non-selective pulse, spatial information can be encoded into the signal during the free precession period (Zhi-Pei Liang and Lauterbur, 2000). As a result of the complex exponential nature of the MR signal, spatial information can be encoded in two ways: *frequency encoding* and *phase encoding*.

Frequency Encoding

Without the loss of generality, consider an idealized homogeneous object with spin density $\rho(x)$ while omitting the relaxation effects. The magnetic field observed by the object after the excitation under homogeneous B_0 and a linear gradient field $G_x x$ can be described at position x as:

$$\omega(x) = \omega_0 + \gamma G_x x \tag{2.47}$$

The corresponding received signal from the object can be written as:

$$\begin{aligned} S(t) &= \int_{object} dS(x,t) \\ &= \int_{-\infty}^{\infty} A\rho(x) e^{-i\gamma(B_0+G_x x)t} dx \\ &= A\left[\int_{-\infty}^{\infty} \rho(x) e^{-i\gamma(G_x x)t} dx\right] e^{-i\omega_0 t} \end{aligned} \tag{2.48}$$

where A is a scaling constant representing different gain terms. The measured signal in Equation 2.48 is said to be *frequency-encoded* since the oscillation frequency of the signal is linearly dependent on the spatial location, and the gradient G_x is called *frequency encoding gradient*.

Phase Encoding

Similar to frequency encoding, consider the local signal after an RF pulse where a gradient G_x is applied for a short duration T_p and then turned off. In this case, the local signal can we written as:

$$dS(x,t) = \begin{cases} \rho(x)e^{-i\gamma(B_0+G_x x)t} & 0 \leq t \leq T_p \\ \rho(x)e^{-i\gamma G_x x T_p}e^{-i\gamma B_0 t} & T_p \leq t \end{cases} \tag{2.49}$$

Accordingly, the local signal for the time interval $0 \leq t \leq T_p$ is frequency-encoded. As a result, when the gradient is switched off, signals at different spatial locations have accumulated different phase angles. In other words, after the preparatory period, the received signal would contain location-dependent phase as:

$$\phi(x) = -\gamma G_x x T_p \tag{2.50}$$

Here, note that the accumulated phase is linearly dependent on the spatial location, and therefore the signal is said to be *phase-encoded*. Similarly, the gradient G_x is referred to as *phase encoding gradient*.

In MRI, 3D imaging can be achieved using multiple methods, where multi-slice imaging is the direct extension of 2D imaging. Nevertheless, true 3D imaging (volumetric imaging) can be achieved by using non-selective RF pulses for signal generation and spatially encoding all three dimensions. In practice, this is usually achieved by frequency-encoding in one dimension while the other two dimensions are phase-encoded.

Echoes

In the rotating frame of reference, the phase accrual due to off-resonance and applied gradient fields can be written as (Nishimura, 1996):

$$\begin{aligned} \phi(x,y,z,t) &= \int_0^t \omega(x,y,z,\tau)d\tau \\ &= \omega_E(x,y,z)t + \omega_{cs}t + \gamma \int_0^t G(\tau) \cdot r \, d\tau \end{aligned} \tag{2.51}$$

where the phase accrual with time can be comprised into three groups: inhomogeneity, chemical shift, and gradient fields. As the spatially-dependent phase accumulates over time, the signal amplitude decays at a faster rate due to dephasing. However, an interesting phenomenon is that, these space-variant phase shifts can be removed momentarily to improve the signal amplitude. The resulting signal is known as an *echo*, and a distinguishing feature of an echo signal compared to an FID signal is the "two-sidedness" of an echo, where one side is due to refocusing of the phase whereas the other side is from the dephasing (Zhi-Pei Liang and Lauterbur, 2000). An echo signal can be generated using two fundamental methods. In *spin echo* methods, multiple RF pulses are used for undoing the phase shifts occurring from field inhomogeneities and chemical shift effects. In *gradient echo* methods, gradient fields are reversed for undoing the phase shifts from gradient fields.

2.2.3 Sampling Requirements

Proper image formation in MRI depends on the appropriate coverage of k-space. Assuming a 2D Cartesian readout with highest sampled spatial frequencies k_{xmax} and k_{ymax} and sampling periods of Δk_x and Δk_y, the sampled signal $\hat{M}(k_x, k_y)$ can be written as (Nishimura, 1996):

$$\hat{M}(k_x,k_y) = M(k_x,k_y) \cdot (\frac{1}{\Delta k_x\, \Delta k_y})\, ^2\text{III}(\frac{k_x}{\Delta k_x}, \frac{k_y}{\Delta k_y}) \cdot\, ^2\sqcap(\frac{k_x}{W_{k_x}}, \frac{k_y}{W_{k_y}}) \tag{2.52}$$

where ^2III is 2D sampling function (2D Shah function), $^2\sqcap$ is 2D rect function and the k-space widths (W_{k_y}, W_{k_y}) are defined as:

$$\begin{aligned} W_{k_x} &= 2(k_{xmax} + \Delta k_x/2) \\ W_{k_y} &= 2(k_{ymax} + \Delta k_y/2) \end{aligned} \tag{2.53}$$

Here, note that the boundaries of the rect function lie a half sample period over the spatial frequency limits on each side. Consequently, the sampled signal can be expressed in the image domain as:

$$\hat{m}(x,y) = m(x,y) ** {}^2\text{III}(\Delta k_x x, \Delta k_y y) ** W_{k_x} W_{k_y}\, \text{sinc}(W_{k_x} x)\, \text{sinc}(W_{k_y} y) \tag{2.54}$$

where $**$ represents 2D convolution operation.

Field of View

From Equation 2.54, it can be observed that the convolution operation with the periodic sampling function leads to periodic replications of the sample in the image domain[3]. This convolution operation of $m(x,y)$ with $^2\text{III}(\Delta k_x x, \Delta k_y y)$ implies that replications of $m(x,y)$ would occur at intervals of $1/\Delta k_x$ in the x-direction and of $1/\Delta k_y$ in the y-direction.

Since the analog-to-digital converter (ADC) uses an anti-aliasing filter, the separation between these periodic replications effectively determines the field-of-view (FOV) in the image. This process is illustrated in Figure 2.6. As such, the FOV can be described as:

$$\begin{aligned} FOV_x &= \frac{1}{\Delta k_x} \\ FOV_y &= \frac{1}{\Delta k_y} \end{aligned} \tag{2.55}$$

Now assume that the ADC acquires samples with a sampling period of Δt with a readout gradient amplitude of G_x. Then the step size along the frequency-encoding direction can be written as:

$$\Delta k_x = \gamma G_x \Delta t \tag{2.56}$$

Along the phase encoding direction, the sampling period depends on the incremental gradient area determined by the incremental gradient amplitude of G_{yi} with a fixed phase-encoding duration of τ_y. Then the step size along the phase-encoding direction can be written as:

$$\Delta k_y = \gamma G_{yi} \tau_y \tag{2.57}$$

---

[3] A more detailed explanation of this is well-known relationship of sampling of continuous-time signals can be found in (Oppenheim, Schafer, and Buck, 1999).

Accordingly, the FOV can be expressed as:

$$\begin{aligned} FOV_x &= \frac{1}{\gamma G_x \Delta t} \\ FOV_y &= \frac{1}{\gamma G_{yi} \tau_y} \end{aligned} \tag{2.58}$$

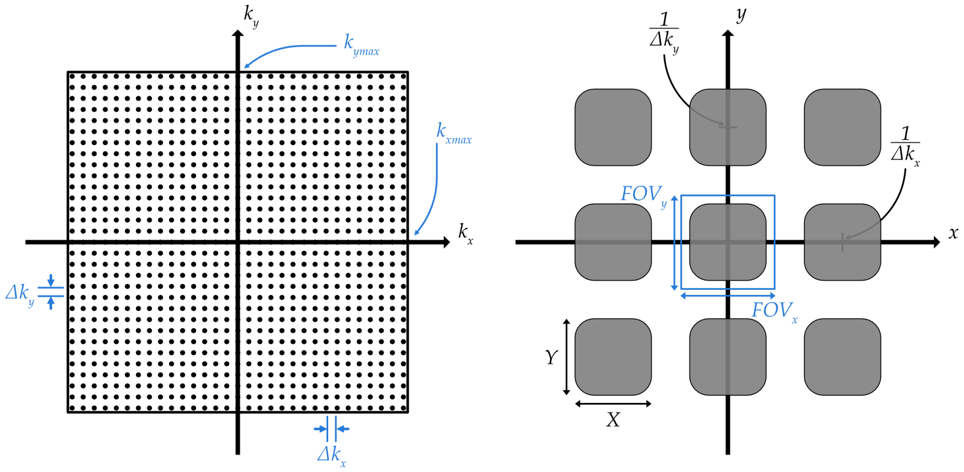

FIGURE 2.6: Sampling in k-space and corresponding replication in image domain.

Spatial Resolution

As evident from Equation 2.54, the sinc function limits the spatial resolution of the sampled image, depending on the highest sampled spatial frequencies k_{xmax} and k_{ymax}. By approximating the full width at half maximum (FWHM) of a sinc function as one half of the interval between first two zero crossings, and defining δ_x and δ_y as the spatial resolution, we can write:

$$\begin{aligned} \delta_x &= \frac{1}{W_{k_x}} = \frac{1}{\Delta k_x N_{re}} \\ \delta_y &= \frac{1}{W_{k_y}} = \frac{1}{\Delta k_y N_{pe}} \end{aligned} \tag{2.59}$$

where N_{re} and N_{pe} denote the number of samples in the readout and phase encoding directions, respectively. Assuming that the number of samples is large, we can simplify k-space widths as:

$$\begin{aligned} W_{k_x} &\approx 2k_{xmax} \\ W_{k_y} &\approx 2k_{ymax} \end{aligned} \tag{2.60}$$

and the spatial resolution expression can be simplified as:

$$\begin{aligned} \delta_x &= \frac{1}{2k_{xmax}} \\ \delta_y &= \frac{1}{2k_{ymax}} \end{aligned} \tag{2.61}$$

Noise Considerations

Like any other measurement system, the MR signals detected by the receiver coils contain an undesirable component that is referred to as *noise*. In imaging applications, noise characteristics and signal-to-noise ratio (SNR) levels are prominent measures of image quality. In MRI, analysis of SNR is complicated due to numerous dependencies (Nishimura, 1996). Nevertheless, the SNR considerations in MRI can be divided into two main categories: instrumental parameters (e.g., B_0 field, receiver coil geometry) and imaging sequence parameters (e.g., flip angle, spatial resolution).

In MRI, the dominant noise is thermal in origin. The Brownian motion of electrons or ions in a conductor, which predominantly arises from the electrolytes in the sample, results in random electrical fluctuations, and is often called *resistor noise* or *Johnson noise* (Nishimura, 1996; Prince and Links, 2015). The variance of this noise can be characterized as:

$$\sigma^2 = \frac{2kTR}{T_{ADC}} \tag{2.62}$$

where k is the Boltzmann constant, T is temperature, R is the effective electrical resistance, and T_{ADC} is the total readout time. Here, the effective resistance includes both the resistance associated with the receiver coil and the resistance associated with the sample. Since the control over sample temperature is limited, noise levels can be decreased by control of R and T_{ADC}.

Often, the resistance in RF coil and electronics can be neglected since it is much smaller compared to that of the body. When the body is approximated as a solenoid, the associated resistance can be calculated as (Prince and Links, 2015):

$$R = \frac{\pi^3\, \mu_0^2\, f_0^2\, N^2\, L\, r_0^4}{2\rho} \tag{2.63}$$

where the permeability constant is $\mu_0^2 = 4\pi \times 10^{-7}$ Wb/(A·m), f_0 is the Larmor frequency, N is the number of turns per unit length, L is the total length, r_0 is the radius, and ρ is the resistivity of the body. Although it can be observed from Equation 2.63 reducing the Larmor frequency would reduce the resistance, it would not improve the image quality since the NMR signal would reduce faster, resulting in a degradation of image quality (Prince and Links, 2015).

A useful and commonly used measure for image quality is *signal-to-noise ratio*. A commonly used definition of SNR is:

$$SNR = \frac{\mu}{\sigma} \tag{2.64}$$

where μ is the mean signal amplitude and σ is the standard deviation of noise. An important relationship can be observed between the SNR and B_0 field. It can be shown that the SNR is proportional to the main magnetic field as (Nishimura, 1996):

$$SNR \propto \frac{B_0^2}{\sqrt{\alpha B_0^{1/2} + \beta B_0^2}} \tag{2.65}$$

where the receiver coil noise is proportional to $B_0^{1/2}$, the noise from the sample is proportional to B_0^2, and α and β are constant terms. Therefore, if the primary source of noise is due to coil resistance, then:

$$SNR \propto \frac{B_0^2}{\sqrt{B_0^{1/2}}} = B_0^{7/4} \tag{2.66}$$

whereas when the primary source of noise is due to sample resistance (as in most cases), then:

$$SNR \propto \frac{B_0^2}{\sqrt{B_0^2}} = B_0 \tag{2.67}$$

However, note that other factors such as T_1 relaxation time also depend on B_0, leading to a complex relationship between field strength and image quality. For example, with increasing B_0, T_1 relaxation time also lengthens; thereby reduces the signal and contrast in imaging applications (Nishimura, 1996).

2.3 Pulmonary Physiology

The purpose of this section is to provide an overview of the structures and the functions of the respiratory system as well as congenital diaphragmatic hernia. For a more detailed description of pulmonary physiology, please see (West and Luks, 2016; Levitzky, 2018; Cloutier, 2019; Michael A. Grippi et al., 2015).

2.3.1 Overview of the respiratory system

The respiratory system is composed of the lungs, the upper and lower airways, the chest wall, the pulmonary circulation, and parts of central nervous system concerned with the regulation of respiration (Cloutier, 2019). The lungs are a pair of cone-shaped organs, separated from each other by the mediastinum, an area that contains heart and its large vessels, trachea (windpipe), esophagus, thymus and lymph nodes (Ionescu, 2013). The lungs have sections, called lobes; the right lung has three lobes (superior, middle and inferior) and the left lung has two lobes (superior and inferior). The chest wall consists of muscles of respiration (e.g., diaphragm) and the rib cage (Levitzky, 2018).

The development of the human lung starts at week-4 of gestation with the appearance of the tracheal outgrowth from the foregut and extends into early childhood (Mullassery and Smith, 2015). The alveolization begins approx. at week-30, and extends to the first few years of life until the growth of chest wall is finished around the age of 8 years (Keijzer and Puri, 2010). Currently, it is accepted that the number of airway generations is completed at birth, but over 85% of the alveoli are formed after birth (Mullassery and Smith, 2015). This means that the lungs are immature at birth, and lung parenchyma contains several generations of transitory ducts that end in saccules, which later develop into alveoli.

The main function of the respiratory system is to allow oxygen to move from the environment into the tissues, and remove carbon dioxide produced by the cellular metabolism from the body. In addition to the gas exchange, other functions of respiratory system include acid-base balance, pulmonary defense and metabolism, and handling of bio-active materials (Levitzky, 2018).

Airways

The breathed air enters the respiratory system through the nasopharynx when inhaled with nose or oropharynx when inhaled with mouth. From there, the air travels down the throat through the glottis, the larynx (voice box), enters the *tracheobronchial tree*, passes through *conducting airways* and ultimately reaches the *alveoli*, where it comes into contact with venous blood at the pulmonary capillaries (Levitzky, 2018). The structures starting from the nose to the larynx constitutes the *upper airways*, whereas the trachea, the bronchial structures and the alveolus constitutes the *lower airways*.

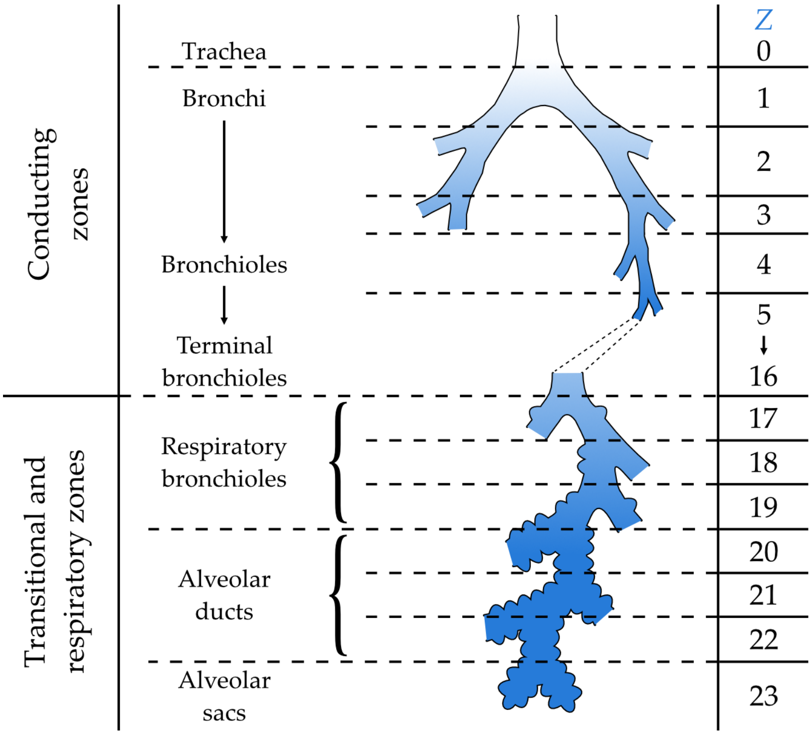

FIGURE 2.7: Modeling of airway generations in human lung according to Weibel's lung model. In adults, air may pass through between 10 to 23 generations on its way to alveoli.

The tracheobronchial tree is an arrangement of branching tubes, that begins at the larynx and terminates at the alveoli in the peripheral of the lungs. The trachea, which originates at the inferior edge of the larynx has been designated as *generation* 0 (denoted with Z) in Weibel's model, and at the carina it divides into the right and left main bronchus (Z=1), that penetrate lung *parenchyma* (tissue of the lung) (Cloutier, 2019). Main bronchi divide into lobar bronchi (secondary bronchi, Z=2), where right main bronchus subdivides into three, delivering air to the three lobes (superior, middle and inferior) of the right lung; whereas the left main bronchus subdivides into two, delivering air to the two lobes (superior and inferior) of the left lung (West and Luks, 2016; Cloutier, 2019). Roughly, in the first six generation, the number of airways doubles in every generation. Beyond the sixth generation, branching becomes asymmetric in branching number, angle, and size (Cloutier, 2019). Therefore, air may pass through as few as 10 or as many as 23 generations from trachea to the alveoli. A schematic representation of airway generations according to Weibel's model is illustrated in 2.7.

The airways starting from the nose and ending with the terminal bronchioles are known as the *conducting airways*. The conducting airways generally constitute the first 16 generations of airways and lead inspired air to gas-exchanging units, and contain no alveoli. As a result, they are incapable of gas exchange and constitute the *anatomic dead space*. The dead space refers to areas of lung that receive ventilation but no blood flow, and in normal individuals has a volume around 150 mL (West and Luks, 2016). The alveoli start to appear in respiratory bronchioles (Generations 17-19), which constitute the *transitional zone*, and increase in number, ending with *alveloar ducts* and *alveolar sacs* (Generations 19-23) (Michael A. Grippi et al., 2015; Levitzky, 2018). This alveolated region of the lung is referred to as the *respiratory zone*, has a volume around 3 L in adults during rest (West and Luks, 2016), and is the site of gas exchange. The portion of lung distal to a terminal bronchiole forms *acinus*, an anatomical unit where the alveoli are located (West and Luks, 2016), and is illustrated in Figure 2.8.

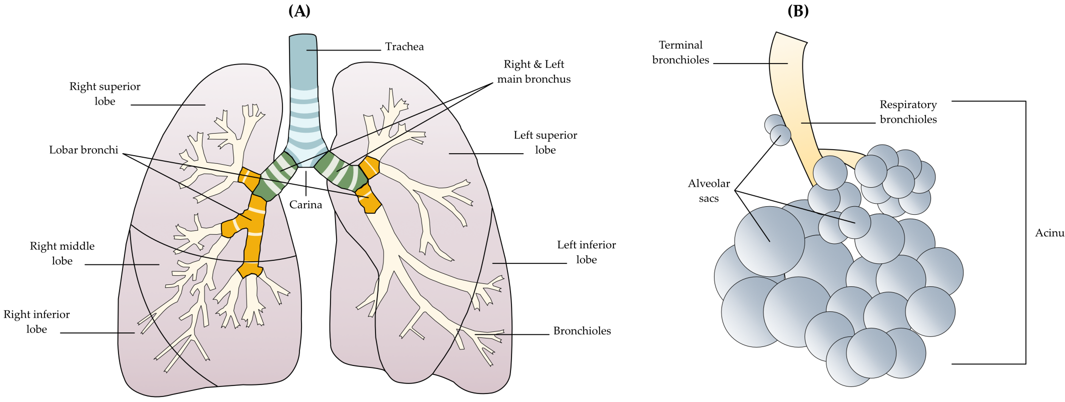

FIGURE 2.8: Schematics of the (A) lungs and (B) pulmonary acinus.

Alveolar-Capillary Unit

Gas exchange occurs in small polyhedral air sacs called alveoli, through a dense network of capillaries and the alveoli, called the *alveolar-capillary network* (Cloutier, 2019). In adults, it is estimated that there are approx. 400 million alveoli with a size of 250 μm, which are completely surrounded by capillaries, and 280 billion capillaries in the lung (Michael A. Grippi et al., 2015; Levitzky, 2018). Accordingly, there are roughly 1000 pulmonary capillaries per alveolus. As a result, a vast area of contact is present between alveoli and pulmonary capillaries for gas exchange; nearly a 100 m^2 of surface area within a space of 5 mm in length (Cloutier, 2019).

The barrier to gas exchange between the alveoli and pulmonary capillaries is about 1 μm in thickness (Cloutier, 2019) and consists of an endothelium lining the capillaries, an epithelium lining the airspaces, and an interstitial layer to house the connective tissue fibers (Michael A. Grippi et al., 2015). Via diffusion from an area of high partial pressure to low partial pressure, the oxygen from the inhaled air passes through the alveolar walls into the plasma and red blood cells, whereas the reverse occurs for carbon dioxide.

Pulmonary Circulation

Similar to the airways, pulmonary blood vessels also form a series of branching tubes from the pulmonary artery to the capillaries and back to the pulmonary veins

(Levitzky, 2018). The *pulmonary circulation* brings the deoxygenated blood from the right ventricle to the alveoli. The capillaries that surround the alveoli has a diameter around 7 μm, just enough for a red blood cell to pass through (West and Luks, 2016). In the capillaries, the red blood cells flow through in a single file order, which creates an efficient arrangement for gas exchange (Cloutier, 2019). When the gas exchange is complete, the oxygenated blood returns to the left side of the heart for systemic circulation. At resting heart rate, it takes a red blood cell about 5 seconds to travel through the pulmonary circulation, and about 0.75 seconds to travel through pulmonary capillaries (Levitzky, 2018). Overall, the pulmonary capillary bed is the largest vascular bed in the body (Cloutier, 2019).

Muscles of Respiration

The lungs are not capable of inflating themselves; the forces for lung inflation are generated by the *muscles of respiration*.

The muscles of inspiration help increase the volume of thoracic cavity, and include the diaphragm, the major muscle of respiration; external intercostal muscles, which pull the ribs upward and forward during inspiration; scalene muscles, which elevate the sternocleidomastoid; the alae nasi, which cause nasal flaring; small muscles in the neck and head; the trapezius; and the muscles of the vertebral (Levitzky, 2018; Cloutier, 2019).

Expiration during quiet breathing (i.e., tidal volume breathing) is passive, and no respiratory muscles contract. Nevertheless, active expiration occurs during active exercise, speech, expiratory phase of coughing or sneezing, or hyperventilation (Levitzky, 2018; Cloutier, 2019). The main muscles of expiration are the muscles of the abdominal wall (i.e., the rectus abdominis, the external and internal oblique, and the transversus abdominis); and the internal intercostal muscles, which pull the ribs downward and inward.

Among these, the diaphragm is the primary muscle of respiration. Diaphragm is a dome-shaped muscle with an approx. 250 cm^2 surface area that separates the thorax from the abdominal cavity (Levitzky, 2018). The contraction of the diaphragm causes the dome to descend into the abdominal cavity, resulting in an elongated thorax with increased volume. As such, on inhalation the diaphragm induces a negative pressure to help draw air into the lungs, and on exhalation the diaphragm helps to expel air by relaxation (Keijzer and Puri, 2010). During quiet breathing, the diaphragm moves approx. 1 cm, but during a deep inspiration, it can move as much as 10 cm (Cloutier, 2019). In adults, the diaphragm is responsible for about two-thirds of the air that enters the lung during tidal breathing in supine position, and about one-third to one-half in upright position (Levitzky, 2018).

Mechanics of Breathing

For air to move in and out of the lungs requires a pressure difference between the atmosphere and the alveoli. Under normal conditions, the inspiration is achieved by lowering the alveolar pressure below the atmospheric pressure (Levitzky, 2018). With the pressure difference, airflow occurs towards the lungs. This movement is controlled by the mechanical properties of the lung as well as the chest wall. The mechanics of the lung are composed of the combined mechanical properties of airways, lung parenchyma, interstitial matrix, alveolar surface and pulmonary circulation; whereas the mechanics of chest wall includes the properties all structures outside the lungs that move during breathing, such as the rib cage, diaphragm, abdominal cavity, and abdominal muscles (Cloutier, 2019). As such, the interaction between the lungs and the chest wall determines the lung volumes. Some of the important lung volumes and capacities are illustrated in Figure 2.9. Although here the inspiratory and expiratory phases in tidal breathing are shown with equal durations, the expiratory phase is usually two to three times longer than the inspiratory phase (Levitzky, 2018). An important aspect the lung volume is that, the measurement of lung volume can be used to detect and follow up disease progression.

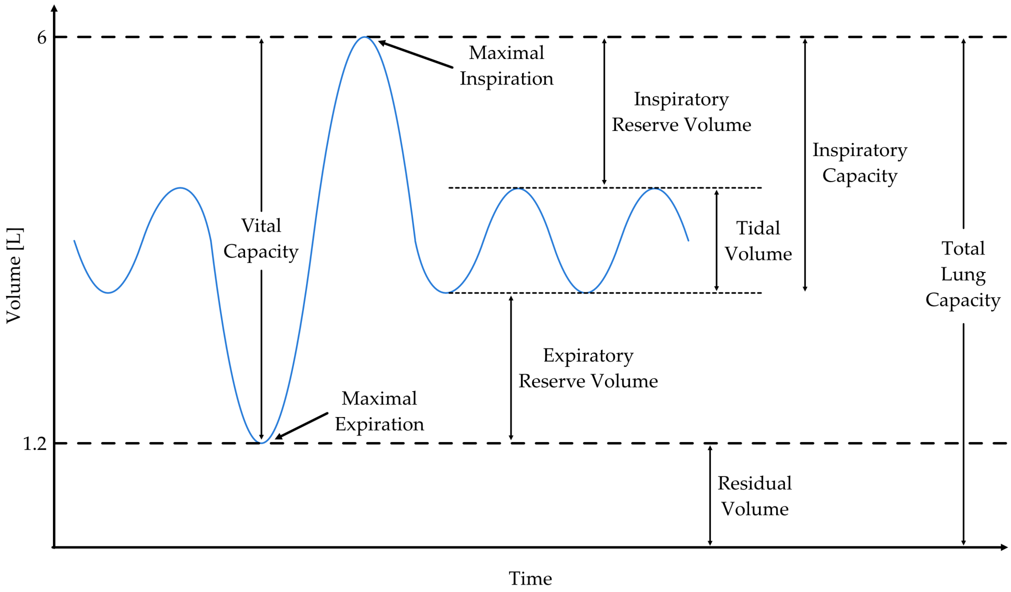

FIGURE 2.9: Various lung volumes and capacities. Inspiratory and expiratory phase in tidal breathing are shown equal durations for illustrative purposes.

Ventilation-Perfusion Relationships

Lung ventilation ($\dot{V}$) and perfusion ($\dot{Q}$) are essential elements in the primary function of the lung. Nevertheless, when analyzed individually, they are insufficient in ensuring normal gas exchange (Cloutier, 2019). The passive diffusion of oxygen and carbon dioxide across the alveolar-capillary barrier occurs according to their concentration differences. For successful gas exchange, these concentration differences have to be maintained by ventilation of the alveoli and perfusion of the pulmonary capillaries. Therefore the ratio of ventilation to perfusion ($\dot{V}/\dot{Q}$) is the major determinant in the assessment of gas exchange.

In healthy adults, the alveolar ventilation is around 4 L/min, and pulmonary blood flow is around 5 L/min, indicating an overall ratio of $\dot{V}/\dot{Q} \approx 0.8$ (Levitzky, 2018). In cases where there is a mismatch between the ventilation and perfusion, this would lead to impairment of both O_2 and CO_2 transfer.

Nevertheless, it should be noted that, a normal $\dot{V}/\dot{Q}$ ratio does not mean the ventilation and perfusion in the gas exchange unit is normal. A region with reduced ventilation and perfusion might still display a normal $\dot{V}/\dot{Q}$ ratio. Furthermore, regional differences in ventilation and perfusion are present in healthy individuals, due to gravitational effects as well as structural effects. For example, in the standing position, going from the top to the bottom of the lung, the perfusion increases more rapidly than ventilation. Meaning that, the $\dot{V}/\dot{Q}$ ratio at the top of the lung is higher compared to the bottom of the lung. As a results, a wide range of localized $\dot{V}/\dot{Q}$ ratios can be observed in healthy lungs, and $\dot{V}/\dot{Q}$ ratios between 0.8 to 1.2 are considered normal (Levitzky, 2018).

2.3.2 Congenital Diaphragmatic Hernia

Congenital diaphragmatic hernia (CDH) is a rare disease, which occurs in 1 in 2000-5000 live births (Oluyomi-Obi, Van Mieghem, and Ryan, 2017). CDH is a developmental defect, characterized by herniation of abdominal organs into the thoracic cavity and consequently, to impairment of lung development, followed by hypoplasia of the pulmonary parenchyma and vasculature, and persistent pulmonary hypertension (Keijzer and Puri, 2010; Weidner et al., 2014). A chest radiography acquired from an infant with CDH is displayed on Figure 2.10.

Although advances in understanding and treatment have improved survival rates, CDH remains to cause significant mortality and morbidity (Wong et al., 2018). A wide range of morbidities can be observed after CDH repair, such as neurocognitive delay, hearing loss, chest wall deformity, or hernia recurrence (Section on Surgery and the Committee on Fetus and Newborn, 2008). Furthermore, infants with large defects, those who have received extracorporeal membrane oxygenation (ECMO) support, or those with a patch repair are at the highest risk (Section on Surgery and the Committee on Fetus and Newborn, 2008). Therefore newborns with CDH, especially patients with heightened risk, are recommended to receive care in specialized centers with periodic follow-up programs to identify and treat the potential development of deformities (Weis et al., 2016b; Hollinger, Harting, and Lally, 2017).

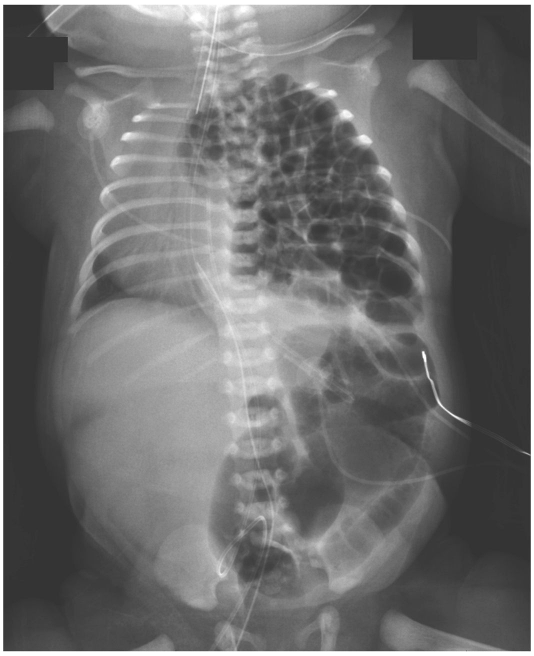

FIGURE 2.10: Chest radiography acquired from a female infant with congenital diaphragmatic hernia reveals multiple loops of bowel occupying the left hemithorax, which shifts the cardiothymic structures to the right. Reproduced with permission from (Klein and Sirota, 2017), copyright Massachusetts Medical Society.

Accordingly, being able to reliably identify high-risk patients, and routine follow-up of these patients remain critical in improving long-term patient outcome. To this end, many different follow-up programs have been established (Morini, Valfrè, and Bagolan, 2017). However, most follow-up schemes require compliance of the patients; therefore they are not feasible in younger children. Furthermore, most of the programs include chest radiographs, which provide limited information about morphological changes; computed tomography (CT) scans which provide tomographic images but limited functional information; spirometry and multiple-breath washout measurements which provide information on the overall pulmonary function only; or nuclear medicine techniques such as planar scintigraphy or single-photon emission computerized tomography (SPECT), which require injection and/or inhalation of radioactive tracers (Björkman et al., 2011; Lederlin et al., 2013; Morini, Valfrè, and Bagolan, 2017). Moreover, routine application of CT and SPECT in infants has been limited due to high radiation doses, lack of the tracers, and requirement for patient cooperation (Björkman et al., 2011).

To overcome the limitations arising from these imaging modalities, MRI based lung imaging has been developed as a radiation-free alternative(Zöllner et al., 2012). In addition, MRI based imaging offers the advantage of acquiring lung morphology and function during the same scanning session.

2.4 MRI of the Lung

The physical properties of the lungs are different compared to other tissue types present in the body. At total lung capacity, the lung fills the entire chest cavity, and can reach up to 6 L in volume, of which approx. 80% is air, 10% is blood and the remaining 10% is tissue (Michael A. Grippi et al., 2015). As a result, lungs have a low tissue density, approx. 0.1-0.3 gr/cm^3 (Schneider, Bortfeld, and Schlegel, 2000; Itoh, Nishino, and Hatabu, 2004; IT'IS Foundation, 2018). This means that lungs have an a priori low proton density compared to other body parts. Consequently, NMR signal level from the lung is approx. ten-fold lower compared to neighboring tissue types (Wild et al., 2012a). Moreover, multiple tissue-air and liquid-air interfaces present in the lungs lead to prominent susceptibility variations and local magnetic field inhomogeneities. These contribute to very short T_2^* relaxation times. Approximate relaxation times for lung tissue at various field strengths are given in Table 2.3. Apart from these, it is known that the gravitational effects as well as respiratory state can cause significant changes in the relaxation times in the lung parenchyma (Stadler et al., 2005; Hahn et al., 2020). Furthermore, thoracic organs are in continuous motion induced by the respiration and cardiac pulsation. Thus, MR-based imaging of the lung parenchyma becomes highly challenging.

TABLE 2.3: List of approximate T_1, T_2, and T_2^* relaxation times for lung parenchyma at various field strengths. Data in the table are adapted from (Nichols and Paschal, 2008; Yu, Xue, and Song, 2011; Campbell-Washburn et al., 2019).

Field Strength	T_1 (ms)	T_2 (ms)	T_2^* (ms)
0.55 T	971	61	10
1.5 T	1171	41	2.11
3 T	1374	-	0.74

Nevertheless, with recent developments, MRI of the lung is becoming an important tool for both research and clinical applications. MRI measurements are currently seen as either the first choice of modality or a supplementary modality to chest radiography and CT (Biederer et al., 2012b), and with improved robustness it may become the preferred modality in the diagnosis of pulmonary diseases. Furthermore, in cases where exposure to ionizing radiation is to be avoided, such as in children, pregnant patients, or patients who require frequent follow-up examinations, MRI is becoming an important tool for clinical applications (Biederer, 2018). In addition to the lack of ionizing radiation, MRI further benefits from the superior soft tissue contrast, the ability to generate dynamic images for studying respiratory dynamics and functional images to assess pulmonary functions.

It is known that pathological conditions in the lung change the parenchymal structure, resulting in either an increase in lung density (e.g., fluid accumulation inside the alveolar space), or a decrease in lung density (e.g., air trapping) (Biederer et al., 2012a). Since the MR signal is proportional to the tissue density, these changes in tissue density enables the diagnosis of pulmonary diseases. Furthermore, changes in the lung perfusion (e.g., pulmonary embolism) also results in a change in the MR signal, thus enables the detection of macro-vascular pathologies (Biederer et al., 2012a). To this end, many methods have been developed to detect parenchymal changes, and these methods can be roughly grouped in two based on the use of contrast agents as: contrast-enhanced methods and non-contrast-enhanced methods.

2.4.1 Contrast-Enhanced Lung Imaging

As a result of the challenges originating from significant susceptibility differences, long T_1 and short T_2 relaxation times, lung MRI methods based on contrast agents have received a great interest; such as dynamic contrast-enhanced (DCE) MRI, hyperpolarized (HP) noble gas imaging, oxygen-enhanced imaging (Molinari et al., 2008), Fluorine-19 (^{19}F) MRI (Neal et al., 2019), or aerosolized gadoliniumbased nanoparticle imaging (Crémillieux et al., 2019). Among these methods, DCE MRI and HP gas imaging has received much attention and clinical application.

Dynamic contrast enhanced (DCE) studies use intravenously injected contrast agent bolus to create a differentiation between the pulmonary arteries and lung parenchyma (Hui et al., 2005). Due to the short pulmonary transit time of the bolus, DCE-based perfusion studies require high temporal resolution, usually in the order of 1-3 seconds (Attenberger et al., 2009). With parallel imaging and other *k*-space acquisition strategies, such as view-sharing or partial Fourier acquisition, DCE-based techniques have been successfully utilized to assess pulmonary perfusion in both adult and pediatric patients, including CDH patients (Attenberger et al., 2009; Zöllner et al., 2012; Weidner et al., 2014; Groß et al., 2021). Nevertheless, safety concerns regarding the use of gadolinium-based contrast agents, the added cost involved with contrast administration, the potential technical issues such as mistimed contrast bolus injection, and non-repeatability of these measurements have limited the application of DCE-based studies (Edelman and Koktzoglou, 2019).

On the other hand, hyperpolarized imaging techniques utilize externally administered inhalative tracers as contrast agents. HP MRI of lung tissue has been initially demonstrated in 1994 by Alber et al. using hyperpolarized ^{129}Xe in mouse (Albert et al., 1994), followed by hyperpolarized ^{3}He imaging in guinea pig (Middleton et al., 1995). By 1996, researchers have successfully demonstrated the utility of hyperpolarized MR imaging for lung imaging in humans, first with volunteers (Ebert et al., 1996; Bachert et al., 1996) and then with patients (Kauczor et al., 1996). Since

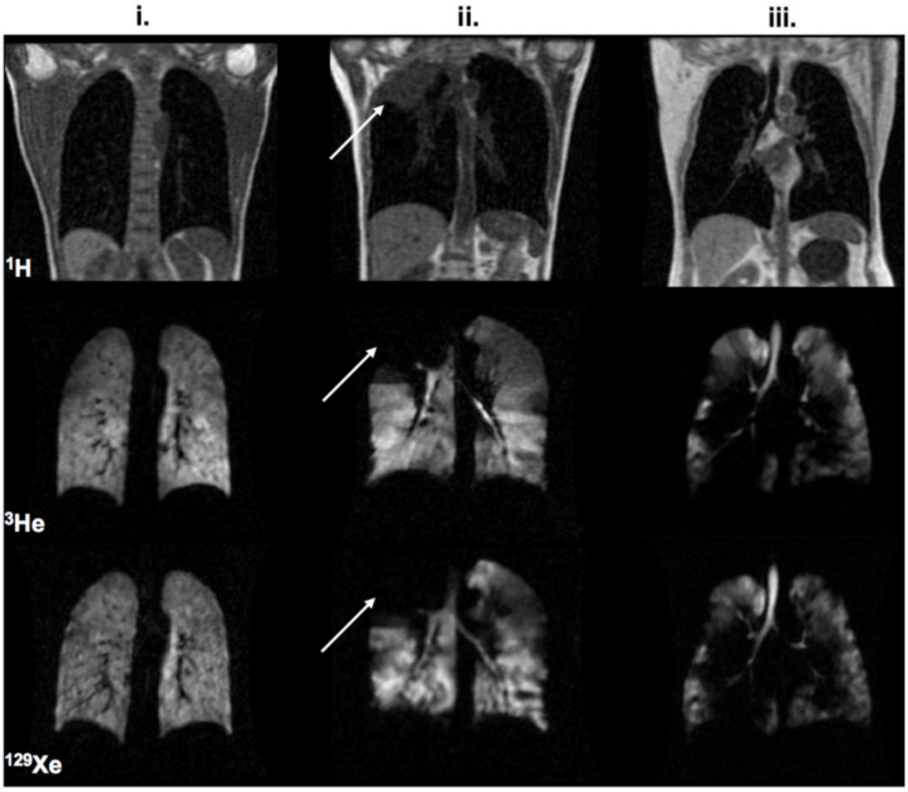

FIGURE 2.11: Representative ^{1}H, ^{3}He, and ^{129}Xe acquisitions from (i) healthy volunteer, (ii) non-small-cell lung cancer patient, and (iii) chronic obstructive pulmonary disease patient. Reproduced from (Stewart et al., 2018), used under Creative Commons CC-BY license.

then, many studies have demonstrated the usefulness of hyperpolarized imaging, and the summary of the current state of hyperpolarized imaging can be found in the following articles (Kruger et al., 2016; Ebner et al., 2017; Stewart et al., 2018). Representative images obtained with ^{1}H, ^{3}He, and ^{129}Xe are illustrated in Figure 2.11. Despite its advantages, the clinical adaption of hyperpolarized imaging has been limited due to numerous factors. Additional hardware and personnel requirements for the sophisticated polarization process, need for multinuclear RF hardware (Wild et al., 2012a), shortage of global ^{3}He supplies leading to high scan costs (Kruger et al., 2016), general anesthetic properties and short T_1 duration of the ^{129}Xe (Bachert et al., 1996), technical difficulties in delivering breathable concentrations of gas and oxygen to patients (Möller et al., 2002), and depletion of the polarization after excitation (Bachert et al., 1996; Möller et al., 2002) can be listed as a few.

2.4.2 Non-contrast-Enhanced Lung Imaging

In part because of the challenges and drawbacks associated with contrast-enhanced imaging, non-contrast-enhanced methods received a renewed interest as an alternative in lung imaging. Performance increases in gradient systems as well as advanced acquisition techniques and post-processing techniques improved the outlook of pulmonary MRI, while enabling high resolution structural imaging as well as functional imaging (Möller et al., 2002).

Compared to the mostly diamagnetic biological tissues, air is paramagnetic. This leads to a bulk magnetic susceptibility difference of $\Delta\chi = 9$ ppm (Bergin, Pauly, and

Macovski, 1991; Saritas, Holdsworth, and Bammer, 2014) at lung-air interfaces. As a result, the numerous air-tissue interfaces create highly inhomogeneous local magnetic field gradients, leading to a rapid dephasing, which is measured to be around 2 ms at 1.5 T, and below 1 ms at 3 T field strengths. Thus gradient echo-based imaging applications require pulse sequences to have short echo times to overcome this limitation arising from the short T_2^* relaxation time (Wild et al., 2012a). With modern MR systems equipped with gradient systems capable of generating gradient strengths up to 80 mT/m with slew rates of 200 mT/m/ms (Fischer and Eberlein, 2013), the usage of gradient echo (GRE) sequences with very short echo times is possible in addition to spin echo (SE) sequences and ultrashort echo time (UTE) sequences. A more detailed list of suggested protocols with respective clinical applications can be found in the following consensus article (Biederer et al., 2012a) or in the following book chapter (Biederer, 2018).

Spin Echo-Based Sequences

Spin echo-based techniques utilize 180° refocusing RF pulses to make the sequence relatively insensitive to magnetic field inhomogeneities and susceptibility effects present in the lungs (Hatabu et al., 1999). In addition, techniques such as *fast spin echo* (FSE, also known as turbo spin echo imaging) which utilize long echo trains with multiple 180°-pulses to acquire data from several *k*-space lines in a single 90°-excitation or *single-shot* methods that obtain data from all *k*-space lines with a single 90°-excitation can be utilized in conjunction with constrained reconstruction techniques (e.g., partial Fourier) to reduce acquisition time in SE imaging. As such T_2-weighted single-shot SE methods with partial Fourier acquisition[4] have been used for detecting infiltrates, masses and nodular lesions with high fluid content (Biederer et al., 2012a). However, due to T_2 blurring and low acquisition efficiency, finer pulmonary structures may not be depictable (Johnson et al., 2013); and the 180° refocusing pulses lead to high specific absorption rates (SAR) (Bieri, 2013).

Ultrashort Echo Time-based Sequences

Ultrashort echo time (UTE) pulse sequences have been suggested for imaging very short T_2 species (Pauly et al., 1989), where they commonly employ half-pulse RF excitations with a non-Cartesian radial readout scheme to cover central *k*-space regions almost immediately after the excitation (Bergin, Pauly, and Macovski, 1991). UTE sequences utilize free induction decay sampling instead of an echo, resulting in a center-out *k*-space trajectory (Johnson et al., 2013; Yang et al., 2020). This enables the acquisition of the signal with limited amount of T_2 and T_2^* decays, by reducing the echo time (TE) to be less that 200 μs (Torres et al., 2019). Here, it should be noted that, different echo time definitions may be used for UTE sequences (Weiger and Pruessmann, 2019). A commonly used definition is the time between center of RF pulse and the start of the data sampling (Hatabu et al., 2020).

UTE imaging has received a great interest for pulmonary imaging applications. Recently, UTE has been successfully applied in diagnosing of pulmonary diseases from neonatal to adult patients (Higano et al., 2017; Walkup, Higano, and Woods, 2019); and has been shown to perform similar diagnosing performance in diseases, such as non-small cell lung cancer or COVID-19, when compared with CT-based imaging (Lee et al., 2019; Yang et al., 2020). Furthermore, recent studies have displayed functional information obtained at 3 T with UTE-based acquisitions (Mendes

---

[4] Some vendor-specific implementations are: HASTE (Siemens), UFSE (Philips), SS-FSE (GE).

Pereira et al., 2019; Balasch et al., 2020). However, UTE sequences are prone to image artifacts and possess reduced sampling efficiency compared to Cartesian readouts (Bieri, 2013). In addition, to reduce respiratory motion in UTE imaging, many studies rely on single breath-holds; which may not be feasible for all patient groups (Balasch et al., 2020). Apart from these, the current 3D UTE approaches are not capable of detecting signal variations caused by inflow effects of unsaturated spins; and hence, unable to detect perfusion related information (Mendes Pereira et al., 2019).

Gradient Echo-Based Sequences

Gradient echo-based techniques can achieve fast acquisition times, because the excitation pulses typically utilize flip angles less than 90° and they do not have the 180° refocusing RF pulses. As a result, short echo times (TE) can be prescribed, while the usage of low flip angles permits most of the longitudinal magnetization to remain undisturbed, and therefore shortens the time for T_1 recovery (Bernstein, King, and Zhou, 2004). After the application of a sufficient and periodic sequence of RF pulses and gradients, the magnetization reaches a dynamic equilibrium called *steady-state*, and the time taken to reach a steady-state is called *transient-state* (Hargreaves et al., 2001). This concept of dynamic equilibrium has been first introduced by Carr in 1958 (Carr, 1958), and is called *steady-state free precession* (SSFP) (Scheffler and Lehnhardt, 2003). With SSFP sequences, different steady-states can be reached by applying different gradient switching patterns or with different RF pulse phases (Bieri and Scheffler, 2013). Broadly SSFP methods can be classified into two groups: the incoherent imaging, where the transverse magnetization is disrupted via *spoiling*; and coherent imaging, where the gradient-induced dephasing within a TR is exactly zero (all three gradient axes are balanced) to refocus magnetization (Scheffler and Lehnhardt, 2003; Bieri, 2013).

For pulmonary imaging, the most commonly used incoherent steady-state GRE imaging techniques are the T_1-weighted RF spoiled GRE imaging[5] and 3D T_1-weighted GRE imaging with view sharing[6]. These methods have been used for detecting small solid lesions and airspace diseases, obtaining high resolution angiograms and/or first pass lung perfusion, and respiratory mechanics (Fischer et al., 2014; Biederer, 2018; Serai et al., 2020).

Similarly, the coherent imaging technique called balanced SSFP[7] (bSSFP) with T2/T1-weighted contrast has been extensively used for pulmonary imaging. This method has been used including, but not limited to, detecting pulmonary fibrosis, embolism, solid legions, bright blood imaging, respiratory mechanics and functional information (Bauman et al., 2009; Rajaram et al., 2012; Serai et al., 2020).

2.4.3 Balanced Steady Steady-State Free Precession Imaging

Balanced steady steady-state free precession (bSSFP) is a coherent imaging technique (pulse sequence) that enables rapid imaging with high signal-to-noise ratio. In bSSFP, both the longitudinal and transverse components of the magnetization reach some steady-state value as a result of the quick succession of RF pulses, which prevents the magnetization from returning to thermal equilibrium.

The magnetization in this dynamic equilibrium is a superposition of different longitudinal and transversal states and can be characterized analytically (Lauzon and Frayne, 2009b). In general, the RF pulses are assumed to be quasi-instantaneous with flip angle α, and the magnetization is allowed to accumulate a resonance offset angle (also called as precession angle) β (in radians) within any TR. More specifically, $\beta = 2\pi(\delta_{CS} + \gamma \Delta B_0) \cdot TR - \phi_{RF}$; meaning that phase accrual over a single TR depends on the chemical shifts of the species, the B_0 field inhomogeneity, and phase increment of RF excitation in successive TRs (Lauzon and Frayne, 2009b). Here note that, because the measured signal is stemming from different transversal and longitudinal magnetization states, the measured signal depends not only on the precession angle ϕ, but also on tissue properties such as relaxation times T_1 and T_2, as well as sequence parameters such as α, TE, and TR (Bieri and Scheffler, 2013).

---

[5] Some vendor-specific implementations are: FLASH (Siemens), T1-FFE (Philips), SPGR (GE).

[6] Some vendor-specific implementations are: TWIST (Siemens), TRAK (Philips), TRICKS (GE).

[7] Some vendor-specific implementations are: TrueFISP, (Siemens), b-FFE (Philips), FIESTA (GE).

Following a transient phase, the time evolution of magnetization in bSSFP experiments reaches a steady state value, where the steady state value displays a strong dependence as a function of the precession angle (Bieri and Scheffler, 2013). The characteristic bSSFP profiles are illustrated for lung parenchyma and lipid tissue in Figure 2.12. Here, note that the maximum steady-state signal is not achievable at on-resonance condition ($\beta = 0$). Off-resonances lead to periodic modulations in the steady-state signal, leading to the characteristic bSSFP *frequency response* (Bieri and

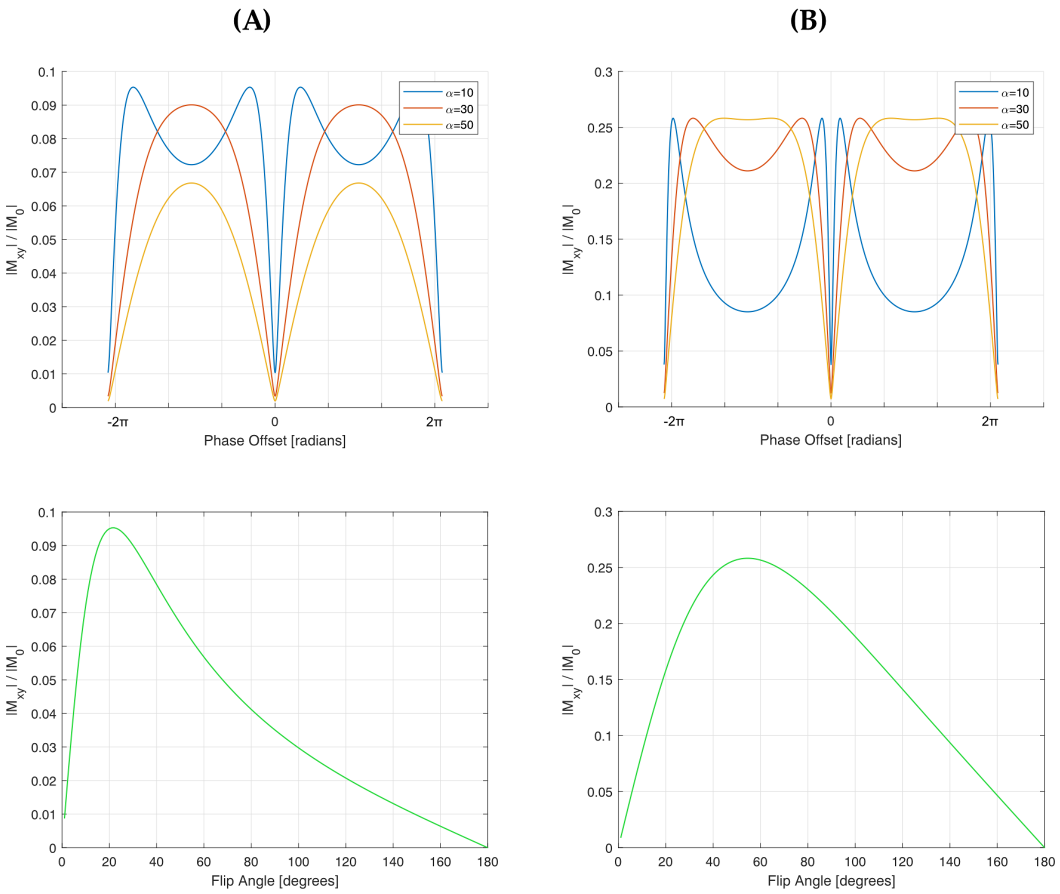

FIGURE 2.12: The characteristic bSSFP off-resonance signal profiles for (A) lung parenchyma and (B) lipid tissue at different flip angles. Shapes of the signal profiles are a strong function of T_2/T_1 and α, and the optimal flip angle depends on the tissue relaxation properties. The simulation parameters: TE/TR=1/2 ms; $T_1 = 1100$ and $T_2 = 40$ for lung parenchyma; $T_1 = 300$ and $T_2 = 80$ for lipid tissue. Notice the scale difference between the plots, indicating a difference in achievable signal level from different tissue types.

Scheffler, 2013). The high signal regions are commonly referred to as the *pass-band* region; whereas the low signal regions are referred to as the *stop-band* region. In the acquired image, the stop-band regions correspond to voxels with precession angles that are close to $\beta = \pm 2k\pi,\ k \in \mathbb{N}$, giving rise to dark bands also known as *banding artifacts*.

Despite its advantages, the bSSFP sequence is limited by its sensitivity to local field variations (Bangerter et al., 2004). Magnetic field inhomogeneities routinely encountered in practice cause signal voids (i.e., banding artifacts) (Cukur, 2015). These characteristic banding artifacts appear in areas of large field variations due to the strong dependence of signal strength on local resonant frequency (Bangerter et al., 2004). In the case of lung imaging, the paramagnetic nature of air and diamagnetic nature of biological tissues lead to bulk magnetic susceptibility differences (Saritas, Holdsworth, and Bammer, 2014), and a static local field gradient is formed at each air-tissue interface (Wild et al., 2012a). As a result, the multiple air-tissue interfaces present in the airways and alveoli in the lungs lead to prominent susceptibility differences and create highly inhomogeneous local magnetic field gradients. Consequently, this phenomena hinders the bSSFP-based rapid imaging of lung tissues.

2.4.4 Non-contrast-Enhanced Functional Lung Imaging

As aforementioned, the gas concentration differences in the lungs have to be maintained via ventilation and perfusion for successful gas exchange. In the presence of pulmonary diseases, varying degrees of ventilation and perfusion abnormalities can be observed in the lungs, such as reduced pulmonary perfusion in CDH patients (Weis et al., 2016b). As such, the evaluation of pulmonary functions has important clinical value for the assessment of prevalent lung diseases.

To this end, many non-contrast-enhanced MRI methods have been developed to acquire information on regional pulmonary functions. Initial studies at low field strengths showed the potential of proton-based MRI for obtaining ventilation information via dynamic acquisitions (Zapke et al., 2006; Deimling et al., 2008). These methods demonstrated the signal intensity changes associated with pulmonary functions during free breathing. In (Bauman et al., 2009), the dynamic acquisition strategy was extended to 1.5 T with non-rigid registration strategies, and it was demonstrated to reliably obtain ventilation and perfusion information using Fourier analysis in the temporal domain. This method, called Fourier Decomposition (FD), enabled the indirect measurement for regional ventilation and perfusion during free-breathing via fast bSSFP acquisitions without the administration of contrast agents. Thereafter, the Fourier Decomposition method was validated in both animal experiments and human patients against other imaging modalities (Bauman, Pusterla, and Bieri, 2016), and more advanced derivations of the method was developed to improve the robustness of the spectral analysis (Bauman and Bieri, 2017; Bondesson et al., 2019).

Besides the FD method, a self-gated approach based on spoiled GRE imaging called self-gated non-contrast-enhanced functional lung imaging (SENCEFUL) was demonstrated to perform reliably by respiratory gating and data binning according to respiratory and cardiac phases (Fischer et al., 2014). This idea was further improved by transferring the data binning strategy to individual images and creating synthesized respiratory and cardiac cycles to generate phase-resolved functional lung (PREFUL) images (Voskrebenzev et al., 2018). Overall, these methods have shown good agreement with other techniques such as hyperpolarized imaging and have shown promise for clinical use (Voskrebenzev and Vogel-Claussen, 2020).

Lastly, two recent studies (Mendes Pereira et al., 2019; Balasch et al., 2020) have displayed functional information obtained at 3 T with UTE-based acquisitions.

In addition to these acquisition techniques, quantification methods were proposed to improve the reliability of non-contrast-enhanced imaging techniques. In (Kjørstad et al., 2014b), a quantification method for ventilation maps was developed using the baseline signal (zero-frequency or DC component) in addition to the local parenchymal density changes. In (Kjørstad et al., 2014b), a method for perfusion quantification was proposed by utilizing the pulmonary blood flow in fully blood-filled voxels as a reference. Although these methods was demonstrated to be useful (Kjørstad et al., 2015; Ljimani et al., 2021), the quantification results can be effected by the underlying differences in tissue relaxation between field strengths. Therefore, it might be necessary to obtain relaxometric measurements (e.g., T_1 and T_2 maps for T2/T1-weighted bSSFP images) for robust quantification, especially at different field strengths. Although an efficient pulmonary relaxometry methods was previously proposed (Bauman et al., 2017), this method requires breath-holding, which may not be achievable by all patient groups. Furthermore, this method has not been demonstrated at 3 T field strength, with possible limitations arising from SAR constraints as well as increased susceptibility effects.

2.4.5 Challenges in Adaptations to Higher Field Strengths

While clinical 3T scanners are now widely available and scanner with even higher field strength are being introduced for clinical imaging (Ertürk et al., 2017; Sadeghi-Tarakameh et al., 2020), these systems create challenges for lung MR imaging. Moving to higher static magnetic field strengths can increase the intrinsic SNR; but the SNR gain comes at the expense of increased tissue heating, B_0 inhomogeneity, RF field inhomogeneity, increased T_1 relaxation time, reduced T_2^* relaxation time, and increased SAR in the tissue. Specifically, in biological tissues, the tissue susceptibility scales with B_0, leading to a degradation in B_0 homogeneity (Wiesinger et al., 2006); and the SAR is proportional to the square of magnetic field strength, meaning that it would quadruple when the field strength is doubled (Chang et al., 2008). In addition, the local magnetic field inhomogeneities arising from multiple air-tissue and air-liquid interfaces at the alveoli result in rapid dephasing of the signal with short T_2^* values, which further shortens at high field strengths; and therefore limits the available SNR. While it may be desirable to use higher receiver bandwidths to account for enhanced line broadening and image blurring stemming from the susceptibility related effects, usage of higher bandwidths also increases the noise levels, and nearly offsets the SNR gain at 3 T (Yu, Xue, and Song, 2011). For fast imaging techniques, such as echo planar imaging (EPI) or bSSFP pulse sequences, B_0 inhomogeneity results in distortions or signal losses in the form of band artifacts. Therefore, the extension of lung imaging to higher field strengths has been limited.

Another difficulty arises from the poor visualization of the lungs. In typical thoracic images, the signals from the muscle and fat tissues dominate the lung signal, which can hinder the visualization of the lungs and can degrade the image quality in parallel imaging reconstructions. These effects are heightened when the thorax is imaged at higher field strengths. As most studies have focused on increasing the available SNR from the lung parenchyma with short echo times, these also lead to a concomitant increase in surrounding tissue SNR. Therefore, suppression of signal contributions from surrounding tissues (e.g., fat or muscle) can improve the overall contrast and visualization of the lung parenchyma (Mai, Knight-Scott, and Berr, 1999), at the expense of increased measurement time.

In (Fink et al., 2007), a comparative study between 1.5 T and 3 T was carried to analyze five different pulse sequences for lung MRI. Here the authors imaged porcine lungs as well as four healthy volunteers with inspiratory breath-hold, and concluded that the imaging characteristics between different pulse sequences did not differ between field strengths. Although lung pathology was successfully visualized at 3 T, the authors also noted the image quality was inferior compared to 1.5 T. In another study (Attenberger et al., 2009), the authors compared contrast-enhanced pulmonary perfusion MRI at 1.5 T and 3 T using a 3D single-shot spoiled GRE sequence during inspiratory breath-hold. Here, the authors noted that at 3 T, SNR obtained from pulmonary vessels was significantly increased compared to 1.5 T; however, the SNR of the lung parenchyma was significantly lower. While the authors noted that the differences between two field strengths did not affect the quantitative perfusion parameters, they suggested 1.5 T as their preferred field strength for pulmonary MRI. Lastly, in (Chassagnon et al., 2019) the authors compared a prototype free-breathing UTE sequence at 1.5 T and 3 T field strengths. In this work, the authors observed that the overall image quality at 3 T was poorer compared to that at 1.5 T, with lower SNR and CNR, and reduced visibility of subsegmental bronchi.

2.4.6 Challenges in Pediatric Imaging

Pulmonary morbidity in infants and young children may arise from many sources, and due to the high rates of pulmonary morbidity in the population of admitted patients (Hahn et al., 2020), pulmonary imaging techniques stand to offer crucial benefit in the assessment and follow-up of pulmonary diseases (Zanette et al., 2022). Chest radiography is commonly utilized as the first-line imaging modality, but it lacks tomographic resolution (Walkup, Higano, and Woods, 2019); CT scans offer submillimeter in-plane image resolution, but concerns regarding the ionizing radiation limits its clinical value (Higano et al., 2017). Particularly for infants and children with chronic morbidities who require routine follow-up examinations, ionizing radiation associated with CT carries significant risk and hampers CT's usefulness for longitudinal studies (Walkup, Higano, and Woods, 2019). Therefore, radiation-free alternative modalities are desired for pediatric pulmonary imaging; and MRI is particularly appropriate for evaluating pulmonary diseases in pediatric patients, since it is a non-ionizing and tomographic modality.

However, there are multiple challenges for MRI-based pediatric pulmonary imaging. In addition to technical difficulties, such as low proton density or susceptibility artifacts, successful MRI acquisitions require significant patient cooperation. For diagnostic-quality images, patients are required to remain still during the entire examination, and breath-holding might be necessary for thoracic imaging. However, children are less likely to follow breathing maneuvers and are less likely to tolerate MRI examination conditions, including acoustic noise and being in a confined space (Janos et al., 2019). Furthermore, breath-hold imaging is commonly not feasible for children below the age of 6 due to the lack of ability to comply with breathing instructions (Biederer et al., 2012a). As such, sedation or general anesthesia is used in many pediatric imaging cases (Biederer et al., 2012a). Yet, due to rising concerns over the effects of anesthesia in children, it is desirable to reduce or eliminate the time spend under anesthesia (Walkup, Higano, and Woods, 2019); which necessitates faster protocols and overall shorter examination times.

A second characteristic feature of the pediatric setting is the large variability in patient physiology. Protocols have to be readjusted for FOV, slice thickness, and in-plane resolution depending on the patient's body size (Biederer et al., 2012a), which complicates protocol setups. Moreover, smaller body sizes of pediatric patients compared to adults lead to higher in-plane resolution requirements. To achieve higher spatial resolutions, stronger gradient fields are required. Yet, safety limitations may prevent the use of high gradient slew rates. Consequently this can lead to undesirable increases in achievable minimum echo times, resulting in a decrease in the signal level due to relaxation effects. Furthermore, the respiratory rates and heart rates in humans are known to vary with age (Fleming et al., 2011). For example, typical respiratory and cardiac rates for 2-year-old children are around 30 breaths per minute and 120 beats per minute, respectively; compared to 12 breaths per minute and 60 beats per minute in adults; which indicates a roughly two-fold difference. Consequently, this necessitates the need for higher temporal resolutions with the imaging protocols.

Lastly, commonly utilized pulse sequences with high in-plane resolutions require long acquisition times, which may become impractical in the lungs due to motion artifacts. Although gating approaches such as respiratory gating with respiratory bellows might be useful for motion compensation in adults, triggering or prospective gating methods increase acquisitions times (Biederer, 2018). Consequently, these techniques may not be desirable in pediatric patients, particularly in very small children, due to the use of anesthesia. Instead, fast image acquisition techniques, such as T_1-weighted spoiled GRE imaging or bSSFP imaging, are needed to compensate for motion effects during free breathing without needing any compliance from the patients, special breathing maneuvers, or increase in the overall scan session duration.

Chapter 3

Phase-cycled balanced SSFP imaging for non-contrast-enhanced functional lung imaging

This chapter is based on the following publication: Efe Ilicak, Safa Ozdemir, Lothar R. Schad, Meike Weis, Stefan o. Schoenberg, Frank G. Zöllner, Jascha Zapp. "Phase-cycled balanced SSFP imaging for non-contrast-enhanced functional lung imaging." *Magnetic Resonance in Medicine.* 2022 Oct; 88(4): 1764-1774. doi:10.1002/mrm.29302.

3.1 Introduction

Functional lung imaging is of great importance for diagnosis and follow-up of prevalent lung diseases (Bauman and Bieri, 2017; Bauman, Pusterla, and Bieri, 2016). To this end, novel non-contrast-enhanced MRI methods have been proposed to acquire regional pulmonary functions as well as morphological information without the use of ionizing radiation (Weis et al., 2016a; Zöllner et al., 2012) such as Fourier decomposition (FD)(Bauman et al., 2009; Kjørstad et al., 2015), self-gated non-contrast-enhanced functional lung imaging (Fischer et al., 2014), perfusion-weighted phase-resolved functional lung (Behrendt et al., 2020), or ultrashort TE-based techniques (Tibiletti et al., 2016; Feng et al., 2018; Delacoste et al., 2019; Balasch et al., 2020).

Fourier decomposition MRI provides regional perfusion and ventilation information by acquiring a series of 2D images during free breathing to capture periodic signal variations associated with perfusion and ventilation (Bauman et al., 2009). Originally developed using balanced SSFP sequence (bSSFP) due to its high SNR for short TRs (Bangerter et al., 2004), this technique can be used with other imaging sequences (Bauman, Pusterla, and Bieri, 2016; Bauman, Pusterla, and Bieri, 2019; Schönfeld et al., 2015; Corteville et al., 2015). Nevertheless, the bSSFP sequence provides higher SNR compared with other sequences (Bauman, Pusterla, and Bieri, 2019), and it has shown promise for clinical use (Capaldi et al., 2015; Bauman et al., 2013; Nyilas et al., 2017; Nyilas et al., 2019; Kaireit et al., 2018).

However, the bSSFP sequence is known to be sensitive to magnetic field inhomogeneities. Multiple lung-air interfaces presented by the airways as well as tissues outside the lung lead to prominent susceptibility differences and local magnetic field inhomogeneity (Wild et al., 2012b; Saritas, Holdsworth, and Bammer, 2014; Deppe et al., 2009; Kurz et al., 2021). This, in turn, creates regions with large off-resonant frequencies and results in local signal losses and signal inhomogeneity in bSSFP acquisitions, also known as banding artifacts (Scheffler and Lehnhardt, 2003; Cukur, 2015; Bieri and Scheffler, 2013; Çukur, Lustig, and Nishimura, 2008). As such, these signal inhomogeneities and artifacts can be misinterpreted and may cause misdiagnosis (Deppe et al., 2009; Sá et al., 2014; Heidenreich et al., 2020). Although dedicated pulse sequences with shortened TR or improved SNR performance have been previously proposed (Bauman, Pusterla, and Bieri, 2016; Corteville et al., 2015), these methods modify durations of excitation and spatial encoding toward scanner-specific hardware limits, hindering widespread clinical use. Moreover, the wider availability of clinical 3T scanners and the growing trend toward higher field strengths further limit the adoption of FD MRI due to more pronounced banding artifacts (Bauman, Pusterla, and Bieri, 2019).

Several methods were previously proposed to alleviate banding artifacts in different bSSFP imaging applications (Atiyah, Keith, and Fallone, 2010; Roeloffs et al., 2019; Hilbert et al., 2018; Çukur, 2016), with multiple-acquisition method being the most common (Cukur, 2015). In multi-acquisition bSSFP, multiple RF phase increments are used to alter the location of banding artifacts (Ilicak et al., 2017; Elliott et al., 2007), and obtained images are combined afterward to suppress the banding artifacts (Çukur, Lustig, and Nishimura, 2008). A common tradeoff associated with this method is the increase in number of acquisitions. In this regard, FD MRI becomes a natural candidate, as it depends on the acquisition of multiple images, usually in the order of hundreds (Bauman et al., 2009).

Here, we propose a new technique that improves robustness against field inhomogeneities in FD MRI by incorporating multiple RF phase cycle increments into bSSFP acquisitions (Ilicak et al., 2021). By changing the RF phase increments during the dynamic acquisition (hereafter referred to as phase-cycled acquisition), we are able to obtain images with spatially shifted banding artifacts. These images are then grouped and processed with FD MRI, and the generated functional maps are combined to improve robustness against banding artifacts. To this end, we compare the robustness against field inhomogeneities of the phase-cycled acquisitions to the conventional acquisitions by means of functional map homogeneity. In addition, we demonstrate results for in vivo functional lung imaging both at the commonly used field strengths of 1.5 T and at 3 T, where the adaption of FD MRI has been limited due to stronger banding artifacts.

3.2 Methods

3.2.1 Fourier decomposition MRI

In conventional FD MRI, 2D bSSFP sequence with single RF phase increment (hereafter referred to as single-phase acquisition) constitutes the basis of the time-resolved acquisitions to assess the signal variations arising from respiratory and cardiac cycles (Bauman et al., 2009). Conventionally, a total of K images are acquired with a frame rate of 3-4 images per second during free breathing (Bauman, Pusterla, and Bieri, 2019), and registered using a nonrigid registration software (Ljimani et al., 2021) to align lung structures, thus enabling the observation of regional parenchymal density changes. Thereafter, temporal Fourier transform is used to spectrally analyze and obtain the signal changes corresponding to respiratory and cardiac frequencies, resulting in ventilation-weighted and perfusion-weighted maps.

3.2.2 Phase-cycled bSSFP

In contemporary phase-cycled bSSFP, N images are acquired with different RF phase cycle increments $\Delta\phi_n$ with $n \in [1\ N]$ (Cukur, 2015; Lauzon and Frayne, 2009a) (see Section 3.6 for a detailed expression of acquired bSSFP signal). The goal of phase cycling is to take advantage of 2π-periodic spectral profile of bSSFP signal with respect to off-resonance. By changing the phase increment $\Delta\phi_n$ between $[0\ 2\pi)$, spatially shifted banding artifacts can be obtained across the FOV. Accordingly, each phase-cycled acquisition can be interpreted as an artifact-free image (S_0) multiplied by a respective bSSFP profile, resulting in $S_n = C_n \cdot S_0$ (Ilicak et al., 2017) (similar to spatial encoding achieved via receiver coil arrays).

3.2.3 Adaptation of phase-cycled bSSFP for FD MRI

In the case of phase-cycled FD MRI, each of the K images can be acquired with a different phase cycle increment, creating the possibility of $N = K$ different bSSFP profiles, at the expense of transient-state behavior. Regardless, these bSSFP profiles would act as a spatial encoding, and in the frequency spectrum of the time series, this would create an additional frequency peak corresponding to the rate of change in phase cycling.

In this work, a block-wise phase-cycling scheme was used with $N = 4$ different phase cycles (Benkert et al., 2015), in which phase increments were selected as $\Delta\phi = 0, \pi/2, \pi, 3\pi/2$. An overview of the acquisition scheme and postprocessing for phase-cycled FD MRI is shown in Figure 3.1. In this scheme, $K/4$ images are acquired for each phase cycle consecutively before changing the phase increment. Block-wise scheme was selected due to the transient-state behavior of the bSSFP signal (Bauman et al., 2009), and to make image registration less error prone to varying banding artifacts.

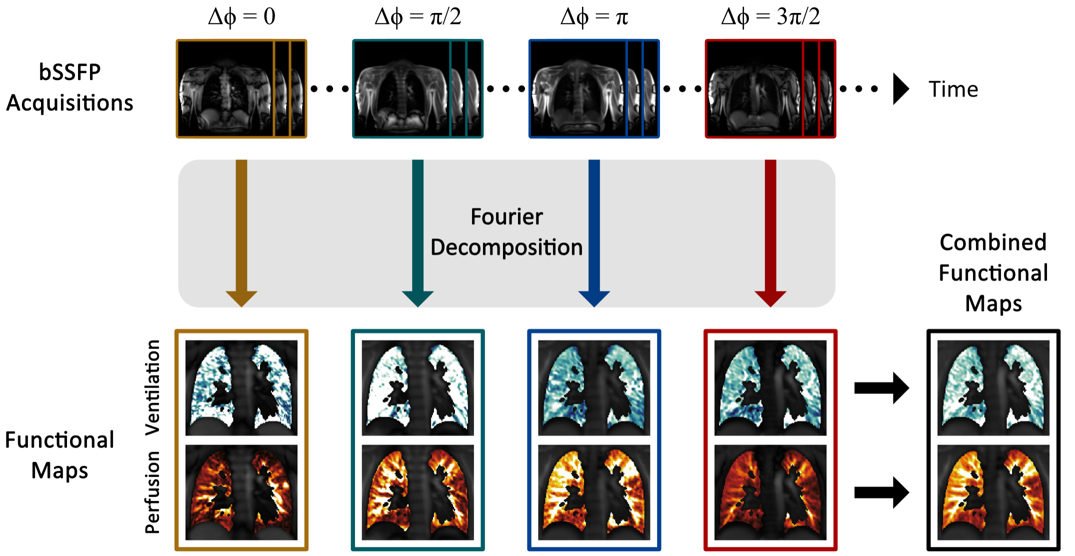

FIGURE 3.1: Overview of the proposed method. Phase-cycled Fourier decomposition MRI uses balanced SSFP (bSSFP) acquisitions with different RF phase increments during free breathing. Images acquired with different phase-cycle increments are then individually processed with Fourier decomposition MRI to obtain respective functional maps. Afterward, quantitative maps are generated and large vessels are excluded. Finally, individual functional maps are weighted-combined to obtain final functional maps.

To enable a careful comparison between single phase with phase-cycled acquisitions, manufacturer-provided bSSFP pulse sequence was modified to acquire K images with a single RF phase increment $\Delta\phi = \pi$, followed by K images acquired with $N = 4$ different phase increments during a single runtime with identical sequence parameters. Additionally, pause between measurements and slice thickness limitations were modified to have better control over temporal resolution and SNR (Bauman et al., 2009), without changing the durations of excitation or spatial encoding.

3.2.4 Data acquisitions

The MRI experiments were performed using a 1.5T and a 3T scanner (Magnetom Aera and Magnetom Skyra, Siemens Healthineers, Erlangen, Germany). Five healthy volunteers (ages 19-29; 3 female, 2 male) underwent free-breathing MRI scans in supine position after obtaining written informed consent. The sequence parameters at 1.5T (3T) consisted of TE/TR=0.80/1.88 (1.02/2.31) ms and acquisition time=174 (188) seconds. For each volunteer, a total of 560 images were acquired: 280 images using single RF phase increment followed by 280 images with phase cycling scheme. The rest of the parameters at both field strengths were as follows: slice thickness=15 mm, pause between measurements=200 ms, α=50°, FOV=450×450 mm^2, matrix=128×128 (scanner interpolated to 256×256), asymmetric echo readout, partial Fourier=6/8, bandwidth=1302 Hz/px, and parallel imaging with GRAPPA factor 3 using 24 integrated phase-encoding lines as the autocalibration region in each image.

3.2.5 Image postprocessing and analyses

Phase-cycled acquisitions were divided into four different subgroups (SGs) based on their RF phase-cycle increment. The initial six images of each subgroup were discarded to eliminate transient state behavior (Bauman et al., 2009). Subgroups were then registered using a prototype nonrigid registration software, fMRLung 3.0 (Siemens Corporate Research, Princeton, NJ, USA) (Chefd'Hotel, Hermosillo, and Faugeras, 2001; Chefd'hotel, Hermosillo, and Faugeras, 2002). A reference image of each subgroup was chosen as the image closest to the average signal intensity of that subgroup.

The FD analysis of the registered time-series data was performed voxel-wise to estimate signal modulations caused by the respiratory and cardiac cycles (denoted with FD_V and FD_Q, respectively). To reduce the variability of estimated ventilation amplitude (Bauman and Bieri, 2017), a Savitzky-Golay filter was used to truncate the time series into complete respiratory cycles (Fischer et al., 2014). Afterward, quantitative ventilation and perfusion maps were generated for individual SGs. The quantitative ventilation map (V Map) was calculated as follows:

$$V = \frac{FD_V}{FD_{DC} + FD_V/2 - BG} \cdot f_V \qquad \text{ml/min/ml} \tag{3.1}$$

where FD_{DC} is the DC component of the time series; BG is the average of background noise estimate (η) from a region containing air; and f_V is number of breaths per minute (Bauman and Bieri, 2017; Kjørstad et al., 2015). The quantitative perfusion map (Q Map) was calculated as:

$$Q = \frac{FD_Q}{FD_Q(blood)} \cdot \frac{f_Q}{2} \qquad \text{ml/min/ml} \tag{3.2}$$

where FD_Q is the whole perfusion-weighted image obtained via the FD analysis; $FD_Q(blood)$ is the perfusion amplitude measured in a voxel completely filled with blood; and f_Q is the number of heart beats per minute (Bauman and Bieri, 2017; Kjørstad et al., 2015). The combined functional maps were obtained from quantified functional maps of individual SGs by segmenting lung parenchyma with exclusion of large vessels, and combining maps via a linear weighted combination method, in which the weights were proportional to estimated SNR (i.e., maximal ratio combining) (Barrow, 1963) in the lung parenchyma. The lung segmentation was performed semi-automatically using a region-growing algorithm (Dirk-Jan Kroon, 2021), and if needed, the region of interests were corrected manually (Heidenreich et al., 2020). The air region was selected based on manual regions of interest (see Figure 3.5), and same regions of interest were assigned across all acquisitions. To ensure fair comparison, the single-phase acquisitions were processed identically to phase-cycled acquisitions by separating the block of 280 images into four different SGs and following the same postprocessing steps to obtain individual and combined functional maps.

To assess the image and functional map quality, we performed SNR, contrast-to-noise ratio (CNR), and coefficient of variation (CV) analyses. The SNR and CNR analyses were performed to ensure that phase-cycled acquisitions were able to obtain similar image and functional map quality compared with single-phase acquisitions, whereas the CV analysis was performed to assess the functional map homogeneity.

The SNR was estimated on registered image series using the power spectrum of the time-series signal (Bauman, Pusterla, and Bieri, 2019). For the noise estimate (η), frequency components above f=1.4 Hz were selected, as they did not include components from respiratory or cardiac cycles. As such, SNR was estimated voxel-wise as follows:

$$SNR_{Map} = \frac{\sqrt{P_0/K_{sg}}}{\eta} \tag{3.3}$$

where P_0 represents the DC component of the power spectrum (f=0 Hz), and K_{sg} represents the number of images in the subgroup. The obtained SNR_{Map} was smoothed using a 2D Gaussian filter, and then averaged over the region containing lung parenchyma to obtain parenchymal SNR estimate (SNR_L) (Bauman, Pusterla, and Bieri, 2019). The CNR of the lung parenchyma was calculated on ventilation-weighted and perfusion-weighted maps obtained from the FD method (Bauman, Pusterla, and Bieri, 2019). The CNR was defined as a ratio of mean functional amplitudes within the lung parenchyma ($FD_V(lung)$, $FD_Q(lung)$) and the region containing air ($FD_V(air)$, $FD_Q(air)$), as follows:

$$CNR_V = \frac{\mu(FD_V(lung))}{\mu(FD_V(air))}, CNR_Q = \frac{\mu(FD_Q(lung))}{\mu(FD_Q(air))} \tag{3.4}$$

Finally, to assess functional map homogeneity, CV was defined as the ratio of SD to mean functional amplitudes within the lung parenchyma obtained from the quantified functional maps ($V(lung)$,$Q(lung)$), as follows (Tedjasaputra et al., 2013; Stadler et al., 2005):

$$CV_V = \frac{\sigma(V(lung))}{\mu(V(lung))}, CV_Q = \frac{\sigma(Q(lung))}{\mu(Q(lung))} \tag{3.5}$$

For statistical analysis, the distributions of quantitative metrics were evaluated for normality using Kolmogorov-Smirnov test. When data were not normally distributed, paired Wilcoxon signed-rank test was used; otherwise, paired *t*-test was used. Differences were considered statistically significant when $p < 0.05$.

3.3 Results

Representative quantitative ventilation maps obtained from a volunteer at 1.5T and 3 T are shown in Figure 3.2, in addition to difference maps between individual SGs and combined maps. At both field strengths, ventilation maps of individual SGs, including the conventional $\Delta\phi = \pi$ acquisition, display local signal losses as well as inhomogeneity across the parenchyma. In comparison, the combined maps reduce the local signal losses and display more homogeneous ventilation values.

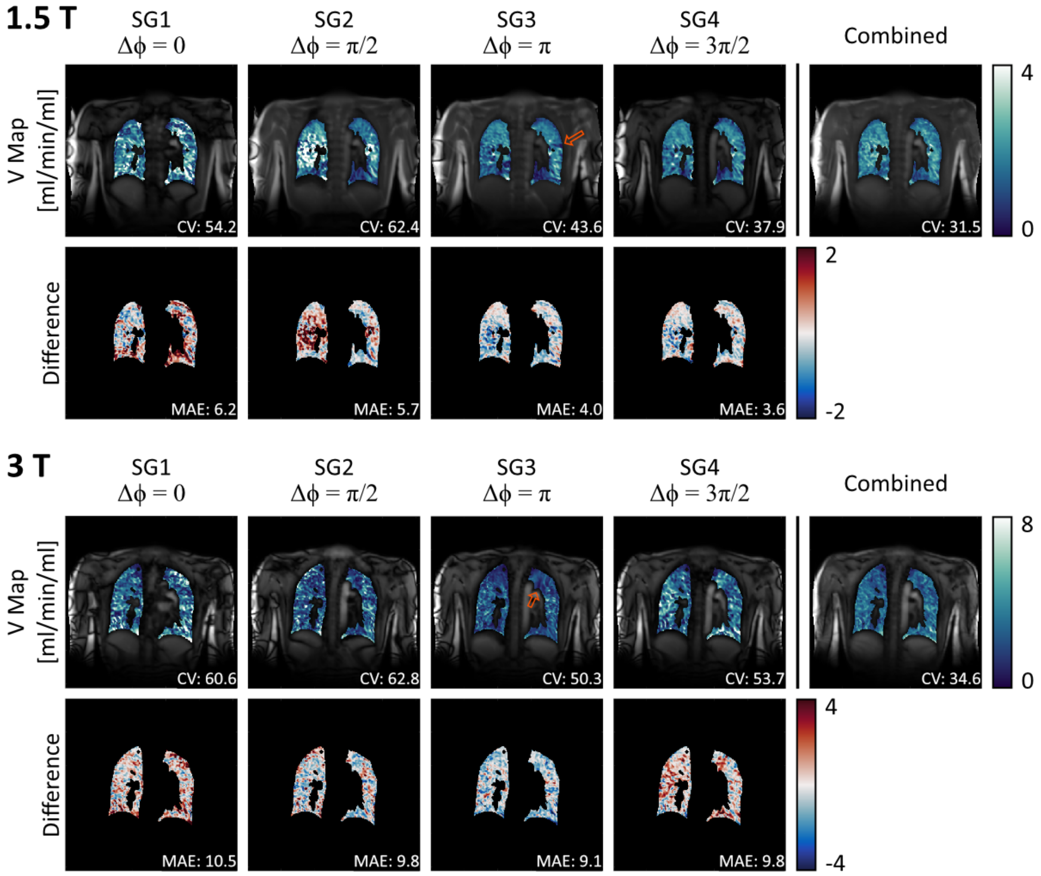
1.5 T
SG1 Δϕ = 0
SG2 Δϕ = π/2
SG3 Δϕ = π
SG4 Δϕ = 3π/2
Combined
V Map [ml/min/ml]
Difference
CV: 54.2
CV: 62.4
CV: 43.6
CV: 37.9
CV: 31.5
4
0
MAE: 6.2
MAE: 5.7
MAE: 4.0
MAE: 3.6
2
-2
3 T
SG1 Δϕ = 0
SG2 Δϕ = π/2
SG3 Δϕ = π
SG4 Δϕ = 3π/2
Combined
V Map [ml/min/ml]
Difference
CV: 60.6
CV: 62.8
CV: 50.3
CV: 53.7
CV: 34.6
8
0
MAE: 10.5
MAE: 9.8
MAE: 9.1
MAE: 9.8
4
-4

FIGURE 3.2: Quantitative ventilation maps (denoted as V Map) obtained from individual subgroups (SGs) and their combination are shown for a volunteer, overlaid on representative cross sections at 1.5T and 3T with respective CV (in units of 10^{-2}) values. In addition, difference maps between subgroups (SGs) and combined map and mean absolute error (MAE, in units of 10^{-2}) values are displayed. At both field strengths, local signal losses (orange arrows highlight for conventional $\Delta\phi = \pi$ acquisition) and signal inhomogeneity is observed across the SGs. In comparison, the combined maps reduce local signal losses while improving map homogeneity across lung parenchyma.

Representative quantitative perfusion maps obtained from a different volunteer at 1.5T and 3T are shown in Figure 3.3, in addition to difference maps between individual and combined maps. Although the combined maps at both field strengths suffer from reduced perfusion signal intensity compared with $\Delta\phi = \pi$ acquisitions, they are still able to display small vascular structures and parenchymal perfusion values. Additionally at 3 T, all SGs suffer from local signal losses due to stronger banding artifacts. In contrast, the combined map is able to improve robustness against these signal losses.

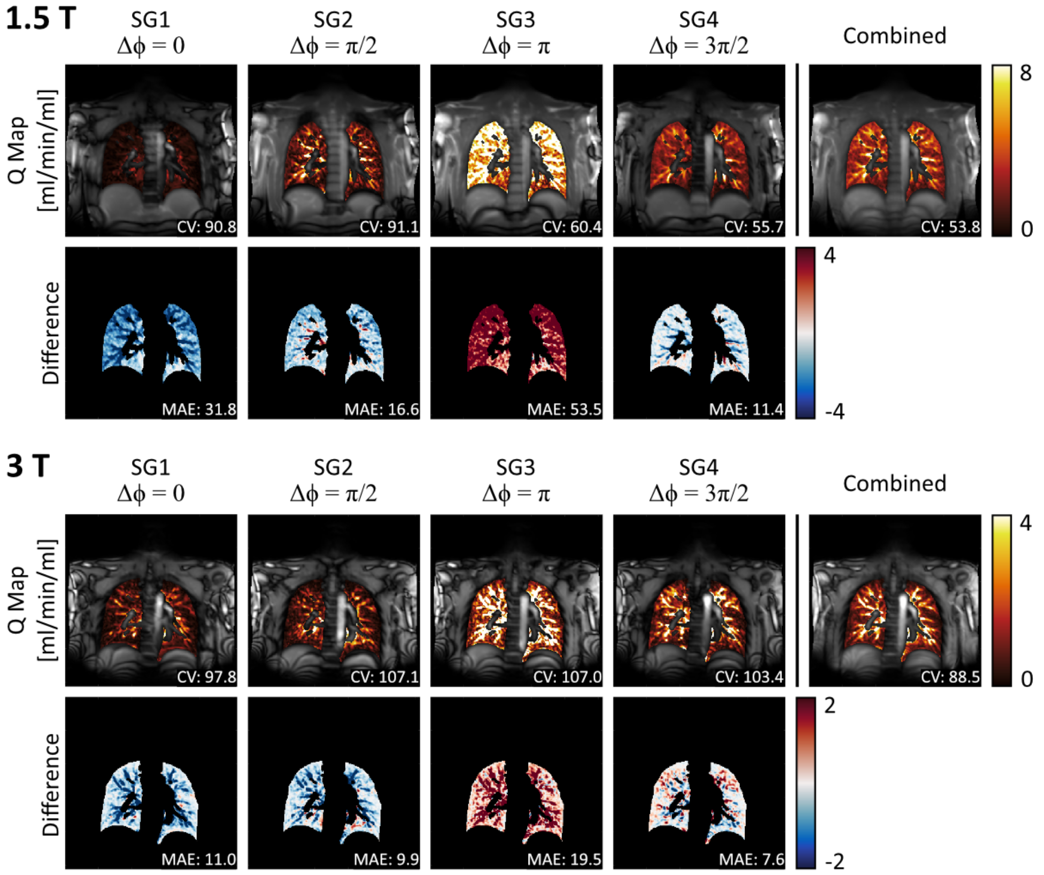
1.5 T
SG1 Δϕ = 0
SG2 Δϕ = π/2
SG3 Δϕ = π
SG4 Δϕ = 3π/2
Combined
Q Map [ml/min/ml]
CV: 90.8
CV: 91.1
CV: 60.4
CV: 55.7
CV: 53.8
8
0
Difference
MAE: 31.8
MAE: 16.6
MAE: 53.5
MAE: 11.4
4
-4
3 T
SG1 Δϕ = 0
SG2 Δϕ = π/2
SG3 Δϕ = π
SG4 Δϕ = 3π/2
Combined
Q Map [ml/min/ml]
CV: 97.8
CV: 107.1
CV: 107.0
CV: 103.4
CV: 88.5
4
0
Difference
MAE: 11.0
MAE: 9.9
MAE: 19.5
MAE: 7.6
2
-2

FIGURE 3.3: Quantitative perfusion maps (denoted as Q Map) obtained from individual SGs and their combinations are shown for a volunteer, overlaid on representative cross sections at 1.5T and 3T with respective CV (in units of 10^{-2}) values. In addition, difference maps between SGs and combined map and MAEs (in units of 10^{-2}) are displayed. At 3 T, individual SGs suffer from local signal losses within the lung parenchyma, as visible in the difference maps. In comparison, the combined maps reduce local signal losses while providing increased map homogeneity.

The corresponding SNR_L and CNR measurements are presented in Tables 3.1 and 3.2. At 1.5T, the $\Delta\phi = \pi$ acquisitions provide the highest mean SNR_L, whereas the $\Delta\phi = 0$ acquisitions perform the worst. Nevertheless, for combined measurements, SNR_L difference between acquisition methods is not significant ($p \geq 0.05$). Similarly, for combined measurements, CNR_V and CNR_Q differences between the two methods are not significant. At 3T, for each subgroup and method (except for SG1 of phase-cycled acquisition), SNR_L values are lower compared with 1.5T due to

TABLE 3.1: Parenchymal SNR of registered images and CNR measurements obtained from functional maps for individual subgroups (SGs) and for both methods at 1.5T and 3T field strengths. Metrics are reported separately for each subgroup as mean±std across 5 subjects.

1.5 Tesla

Single-Phase	*SG 1*	*SG 2*	*SG 3*	*SG 4*
SNR_L	40.7±9.8	39.1±6.3	38.3±5.6	41.8±8.3
CNR_V	28.9±12.8	30.3±14.6	33.5±18.2	26.0±11.1
CNR_Q	10.3±2.5	11.8±3.1	12.7±4.7	13.0±4.6

Phase-Cycled	*SG 1*	*SG 2*	*SG 3*	*SG 4*
SNR_L	12.1±4.0	20.6±7.3	35.5±7.2	29.4±4.0
CNR_V	21.5±10.6	24.3±14.3	31.6±17.7	31.7±14.2
CNR_Q	21.6±6.2	14.7±3.8	11.5±3.8	14.4±4.4

3 Tesla

Single-Phase	*SG 1*	*SG 2*	*SG 3*	*SG 4*
SNR_L	14.0±5.3	13.2±3.5	12.1±2.8	13.4±3.6
CNR_V	21.5±10.0	22.1±10.5	24.2±10.6	23.3±11.0
CNR_Q	19.2±6.3	16.2±3.4	15.2±2.2	17.9±4.4

Phase-Cycled	*SG 1*	*SG 2*	*SG 3*	*SG 4*
SNR_L	12.2±1.5	10.1±2.1	13.1±2.6	16.0±3.6
CNR_V	24.5±8.1	15.7±4.9	19.3±7.0	30.5±11.8
CNR_Q	19.4±3.4	14.4±2.8	15.1±2.1	19.4±3.5

increased susceptibility effects. For the combined measurements, the SNR_L, CNR_V, and CNR_Q differences between both methods are not significant, respectively. Taken together, these results suggest that phase-cycled acquisitions do not suffer from reduced bSSFP pass-band efficiency compared with single-phase acquisitions.

Figure 3.4 displays the combined functional maps overlaid on top of combined cross-sections at 1.5T and 3T for again a different volunteer. At both field strengths, the phase-cycled acquisitions are able to suppress local signal losses in ventilation maps more successfully compared with single-phase acquisitions. Regarding perfusion maps, phase-cycled acquisitions are able to display prominent structures at both field strengths, and at 3T, phase-cycled acquisition provides better depiction of parenchymal perfusion compared with single-phase acquisition.

Homogeneity assessments of combined functional maps are listed in Table 3.3. In terms of ventilation map assessments, CV values at both field strengths show that phase-cycled acquisitions significantly improve the ventilation map homogeneity compared with the conventional single-phase acquisitions ($p < 0.05$). In terms of perfusion map assessments, although we observe a tendency toward lower CV values at 3T for phase-cycled acquisitions, we do not observe a significant difference between the two methods at both field strengths.

TABLE 3.2: Parenchymal SNR and CNR measurements obtained from the combined measurements at 1.5T and 3T field strengths. For the combined SNR_L measurements, normalized registered images of individual subgroups were analyzed and weighted combined with respect to the estimated SNR. For the combined CNR measurements, individual functional maps (FD_V and FD_Q) were weighted combined with respected to estimated SNR and corrected for the number of breaths and heart beats per minute (f_V and f_Q), but were not quantified according to Equations 3.1 and 3.2 in order to avoid amplified signal levels in the air regions. Metrics are reported as mean±std across 5 subjects.

1.5 Tesla	*Single-Phase*	*Phase-Cycled*
SNR_L	40.7±5.1	34.4±4.5
CNR_V	30.0±14.3	29.7±14.0
CNR_Q	11.9±3.4	14.3±4.1

3 Tesla	*Single-Phase*	*Phase-Cycled*
SNR_L	13.5±4.0	14.1±2.4
CNR_V	22.8±10.2	22.7±6.4
CNR_Q	17.2±3.9	17.2±1.8

TABLE 3.3: Coefficient of variation (CV in units of 10^{-2}) measurements of combined functional maps are reported at 1.5T and 3T field strengths. Metrics are reported for each combined functional map as mean±std across 5 subjects, * and ** denotes significant differences ($p < 0.05$) between respective groups.

Ventilation - CV_V		
1.5T	*Single-Phase*	39.9±5.2*
	Phase-Cycled	29.7±2.6*
3T	*Single-Phase*	49.5±3.7**
	Phase-Cycled	37.5±3.1**
Perfusion - CV_Q		
1.5T	*Single-Phase*	54.0±5.2
	Phase-Cycled	55.3±4.9
3T	*Single-Phase*	95.8±15.3
	Phase-Cycled	84.5±6.7

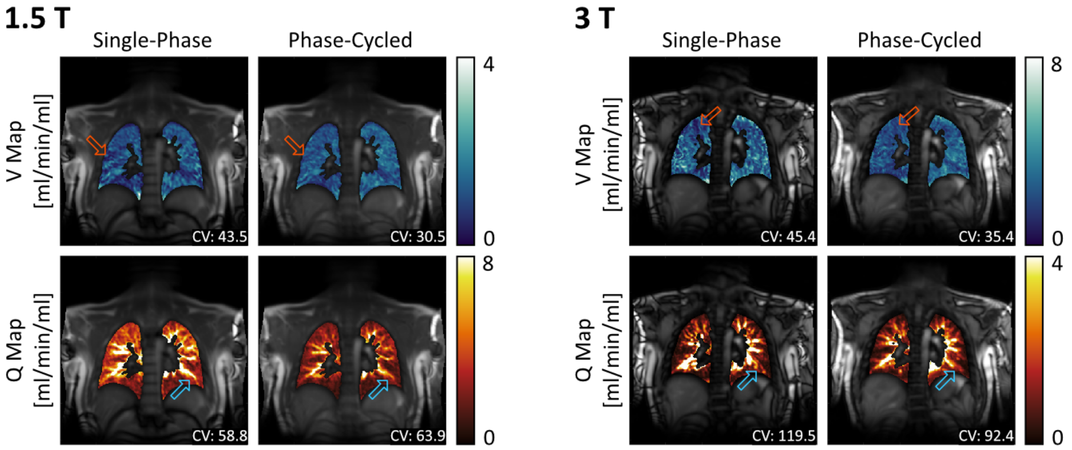

FIGURE 3.4: Combined functional maps of SGs for both methods overlaid on combined cross section at 1.5T and 3T. At both field strengths, the quantitative ventilation maps (denoted as V Map) obtained from phase-cycled acquisitions show robustness against local signal losses (orange arrows) compared with single-phase acquisitions. Regarding perfusion maps (denoted as Q Map), phase-cycled acquisitions display slightly reduced signal levels compared with single-phase acquisitions, due to averaging of multiple phase cycles, including acquisitions with suboptimal SNR. Nevertheless, phase-cycled acquisitions are able to reproduce prominent structures (teal arrows) at both field strengths and improve parenchymal perfusion depiction at 3T.

3.4 Discussion

In this work, phase-cycled bSSFP acquisitions were investigated for functional lung imaging at 1.5 T and 3 T field strengths. As demonstrated, magnetic field inhomogeneities can cause signal losses in the bSSFP-based FD MRI technique, resulting in inhomogeneous functional maps. By using RF phase cycling, the spatial location of these signal losses can be shifted, resulting in robustness against field inhomogeneities in combined maps. Our results indicate that, compared with the conventional acquisition, phase-cycled acquisitions show improved robustness against field inhomogeneities while significantly improving ventilation map homogeneity at both field strengths.

The reduced mean $\mathrm{SNR_L}$ values for phase-cycled acquisitions compared with single-phase acquisitions at 1.5 T can be explained by the frequency response of bSSFP, as the conventional $\Delta\phi = \pi$ acquisitions shift the center of pass band to achieve the highest steady-state signal (Bieri and Scheffler, 2013). Nevertheless, this reduction in $\mathrm{SNR_L}$ is not statistically significant at both field strengths. Also, note that with increased field inhomogeneity and susceptibility effects at 3 T, the single-phase acquisition is not able to achieve center-of-pass-band consistently across lung parenchyma, as indicated by the reduced differences of $\mathrm{SNR_L}$ values between acquisitions with different phase increments. Regarding the limited improvement in $\mathrm{CV_Q}$ values, one possible explanation is the continuous flow of unsaturated blood into the imaging slice. The inflowing blood would be in the transient state compared with the steady state reached in pulmonary parenchyma (Scheffler and Lehnhardt, 2003); thus, phase cycling would have limited effect on blood and hence on perfusion maps.

In this work, quantitative maps obtained with different field strengths are displayed for different scales for better visualization. Although our quantitative ventilation and perfusion values at both field strengths are in agreement with previous studies (Bauman, Pusterla, and Bieri, 2019; Glandorf et al., 2020), the scaling was done to partially overcome the limitations arising from the quantification methods. The ventilation quantification method developed by Zapke et al. (Zapke et al., 2006) models the relative proton density change but omits tissue relaxation differences. Similarly, the perfusion quantification method developed by Kjørstad et al. (Kjørstad et al., 2014a) neglects the differences between blood and lung relaxation (Fischer et al., 2008). However, even when the influence of respiratory state on tissue relaxation parameters is ignored (Stadler et al., 2005), the image contrast (eg, T2/T1 weighting for bSSFP) would affect the quantification results, leading to a bias depending on field strength and sequence parameters (eg, TE, TR, flip angle). We speculate that the significantly higher quantitative perfusion results observed by Behrendt et al. (Behrendt et al., 2020) compared with dynamic contrast-enhanced MRI, and the poor reproducibility of quantitative ventilation and perfusion values between 1.5 T and 3 T stated by Glandorf et al. (Glandorf et al., 2020) are also due to the omission of tissue-relaxation terms in the quantification step. To overcome this problem, further studies are needed to develop quantification methods that take tissue-relaxation properties into account.

A possible limitation of the phase-cycling scheme stems from the transient behavior observed in the received bSSFP signal. To alleviate this, the initial six images in every subgroup were excluded as previously suggested (Bauman et al., 2009). This equates to a loss of about 2 s of acquisition time per phase-cycle increment (i.e., an additional 6 s of excluded acquisition time compared with conventional acquisitions). For this reason, the phase-cycled FD method suffers from a lower scan efficiency compared with the conventional FD method. Please note that for successful applications of FD MRI, multiple respiratory and cardiac cycles are needed to be captured with sufficient temporal resolution (Ilicak et al., 2019a) and commonly, images in the order of hundreds are acquired for FD-MRI applications (Bauman and Bieri, 2017; Ljimani et al., 2021). Here, the total number of acquisitions prescribed was within the range of values previously used for conventional acquisition studies (Bondesson et al., 2019), and no additional time was required to accommodate additional phase cycle increments. Another limitation of the current implementation originates from the phase cycle increments used in this study. Here, we selected the commonly used equispaced phase increments across $[0\ 2\pi)$ (Benkert et al., 2015). As our observations indicate, this phase cycling scheme might be suboptimal for lung imaging, and future investigations are warranted to improve signal characteristics at different field strengths. Finally, this study was limited to a small sample size of healthy subjects, and further investigations might be needed to determine the sensitivity of the phase-cycled acquisition scheme to clinically relevant ventilation and perfusion abnormalities.

Several different approaches were previously proposed for improving 2D functional lung imaging. Recently, spoiled gradient echo-based acquisitions displayed favorable results (Bauman, Pusterla, and Bieri, 2019; Voskrebenzev et al., 2017). Nevertheless, the SSFP-based techniques should yield higher SNR compared with these techniques (Bauman, Pusterla, and Bieri, 2019). Another strategy, termed as uf-SSFP, aims to reduce durations of excitation and spatial encoding to achieve very short TE and TR (Bauman, Pusterla, and Bieri, 2016; Bieri, 2013). While this pulse sequence has shown improved results compared with bSSFP sequence, field inhomogeneity artifacts at 3 T still hinder its usability.

The proposed strategy can be advanced along several lines. First, the pulse sequence optimization procedures of uf-SSFP can be combined with phase cycling to further improve robustness against field inhomogeneities, while improving parenchymal signal intensity (Bieri, 2013). Second, here we used the conventional FD approach to obtain functional maps. Instead, more advanced methods can be used to improve the postprocessing (Bauman and Bieri, 2017; Bondesson et al., 2019). Third, we did not analyze the V/Q ratio due to inherent issues arising from the quantification techniques. Nevertheless, with improved quantification methods, MRI-based V/Q imaging may become a viable alternative for detecting V/Q abnormalities (Björkman et al., 2011) and pulmonary diseases (Le Roux, Le Gal, and Salaun, 2020). Finally, because this study focused on obtaining functional maps, banding artifact correction was not implemented on the time-resolved images. In cases in which banding artifacts cause notable errors, such as during nonrigid image registration, more sophisticated techniques can be leveraged for artifact suppression before FD analysis (Biyik, Ilicak, and Çukur, 2018). Nevertheless, the weighted combination of functional maps acts as a method to mitigate the effects stemming from field inhomogeneities (Bangerter et al., 2004), and although more sophisticated combination techniques have been previously suggested (Çukur, Lustig, and Nishimura, 2008), the combination method was used to preserve the linearity in quantified functional maps.

3.5 Conclusions

In this work, we have proposed an alternative acquisition scheme for non-contrast-enhanced functional lung imaging. The method uses RF phase cycling during acquisition to obtain multiple images with different signal characteristics. Although the phase-cycled acquisition suffers from lower scan efficiency compared with single-phase acquisition, it improves robustness against local signal losses, and significantly improves ventilation map homogeneity at both field strengths. Overall, phase-cycled acquisition demonstrates improved robustness against magnetic field inhomogeneities at both field strengths, and may serve as a valuable tool in the clinical adaptation of FD MRI at 3 T field strength.

3.6 Appendix

MRI signal acquired at spatial location r for n^{th} phase cycled increment can be expressed as (Cukur, 2015):

$$S_n = M(r)\frac{e^{i(\phi(r)+\Delta\phi_n)TE/TR} \cdot (1 - A(r)e^{-i(\phi(r)+\Delta\phi_n)})}{1 - B(r)cos(\phi(r) + \Delta\phi_n)} \tag{3.6}$$

where TE is the echo time, TR is the repetition time, $\phi(r)$ is the phase accrual over a single TR due to off-resonance, and $\Delta\phi_n$ is the RF phase cycle increment. The terms $M(r)$, $A(r)$, and $B(r)$ are defined as (Cukur, 2015):

$$M(r) = \frac{iM_0e^{-TE/T_2(r)}(1 - E_1(r))sin\alpha}{1 - E_1(r)cos\alpha - (E_1(r) - cos\alpha)E_2^2(r)} \tag{3.7}$$

$$A(r) = E_2(r) \tag{3.8}$$

$$B(r) = \frac{E_2(r)(1 - E_1(r))(1 + cos\alpha)}{1 - E_1(r)cos\alpha - (E_1(r) - cos\alpha)E_2^2(r)} \tag{3.9}$$

where M_0 is the equilibrium magnetization, α is the flip angle, $E_1(r) = e^{-TR/T_1(r)}$, $E_2(r) = e^{-TR/T_2(r)}$, $T_1(r)$, and $T_2(r)$ denote longitudinal and transverse relaxation times, respectively. Note that in Equation 3.6, the terms M, A, B depend on sequence and tissue relaxation parameters, but do not depend on off-resonance or phase increments (Biyik, Ilicak, and Çukur, 2018).

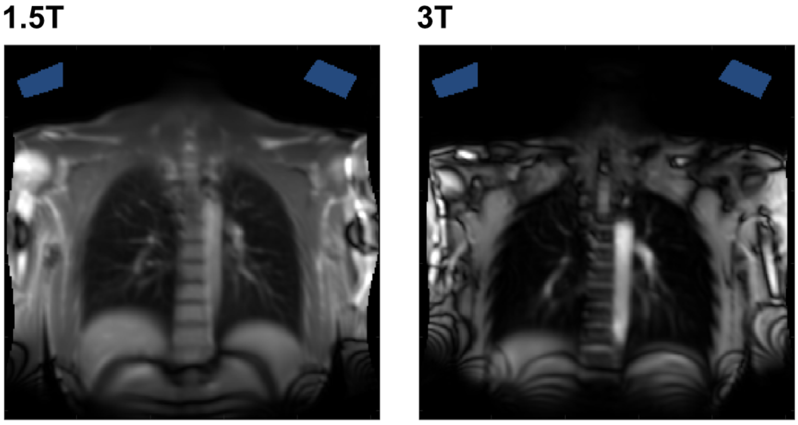

FIGURE 3.5: For the selection of air region, manual ROIs were used. The selected ROIs are displayed in color blue, overlaid on representative magnitude images in grayscale. Same ROIs were assigned for all subjects and at both field strengths.

Chapter 4

Dynamic mode decomposition of dynamic MRI for assessment of pulmonary ventilation and perfusion

This chapter is based on the following publication: Efe Ilicak, Safa Ozdemir, Jascha Zapp, Lothar R. Schad, Frank G. Zöllner. "Dynamic Mode Decomposition of Dynamic MRI for Assessment of Pulmonary Ventilation and Perfusion." *Magnetic Resonance in Medicine.* 2023 Aug; 90(2): 761- 769. doi:10.1002/mrm.29656.

4.1 Introduction

Fourier decomposition (FD) (Bauman et al., 2009) and related methods such as self-gated non-contrast-enhanced functional lung imaging (SENCEFUL) (Fischer et al., 2014) or phase-resolved functional lung imaging (PREFUL) (Voskrebenzev et al., 2018) have been demonstrated as viable options for obtaining regional pulmonary ventilation and perfusion information during free-breathing and without the use of contrast agents (Ljimani et al., 2021). These methods make use of the periodic signal changes associated with proton density changes due to respiration (Zapke et al., 2006) and flow of unsaturated spins due to pulsation (Risse and Bauman, 2016). In order to identify regional ventilation and perfusion related signal changes, these methods combine nonrigid registration of dynamic acquisitions with either spectral analysis based on temporal Fourier transform (Bauman et al., 2009) or synthetization of complete respiratory and cardiac cycles via sorting and interpolation (Voskrebenzev et al., 2018).

Previous studies have successfully implemented Fourier transform-based techniques to obtain local pulmonary functions for diagnostic purposes, such as in cystic fibrosis (Nyilas et al., 2017) or chronic obstructive pulmonary disease patients (Behrendt et al., 2020). More recently, modifications to the FD approach have been proposed to improve functional image quality. These include nonuniform Fourier-based approach to improve robustness against frequency variations (Bondesson et al., 2019); respiratory and cardiac phase estimation methods, such as self-gating approaches to achieve *k*-space based phase estimation with data binning (Fischer et al., 2014; Mendes Pereira et al., 2019), or image-domain based phase estimation with fitting of images onto a single sine wave (Voskrebenzev et al., 2018; Behrendt et al., 2020). While these methods have shown improved image quality compared to the original FD technique, these approaches require multi-step post-processing with multiple filtering operations followed by the temporal Fourier analysis. Moreover, the Fourier transform of incomplete time-series is known to cause spectral distortions (Lin et al., 1997), which can lead to erroneous estimation of signal amplitudes. As such, these methods can suffer from the amplitude and frequency estimation issues (Bondesson et al., 2019).

To improve the robustness of amplitude and frequency estimation, modifications to the FD method such as truncation of acquisitions into complete time-series (Ilicak et al., 2022b); and more advanced techniques such as matrix pencil (MP) decomposition (Bauman and Bieri, 2017) which rely on Hankel matrix structure have been previously proposed. Yet, the truncation method decreases the scan efficiency by excluding collected measurements during post-processing; whereas the MP implementation described previously (Bauman and Bieri, 2017) requires a multi-step approach with low-pass and high-pass filtering operations before the spectral analysis. Moreover, the MP technique is not capable of estimating frequencies and amplitudes simultaneously (Pogorelyuk and Rowley, 2018), and is not capable of obtaining the dynamic system matrix (Alassaf and Fan, 2021).

Here, we propose a new technique based on dynamic mode decomposition (DMD) to identify dominant spatiotemporal features from the registered dynamic images. Compared to other techniques, a unique advantage of DMD is its ability identify system matrix, which provides a matrix representation of the underlying dynamics (Kutz et al., 2016). As such, DMD is able to extract physically interpretable spatiotemporal features (Kutz et al., 2016). To demonstrate the proposed approach, comprehensive evaluations were performed across phantom simulations and in vivo volunteer measurements.

4.2 Methods

4.2.1 DMD

Originally proposed by the fluid mechanics community to decompose complex flow fields, the DMD is a relatively new data-driven method for modal analysis of time-series acquisitions (Schmid et al., 2011). More broadly, it has been successfully demonstrated in various fields ranging from power systems analysis (Alassaf and Fan, 2021) to medical imaging (Groun et al., 2022; Tirunagari et al., 2017), to identify dominant spatiotemporal coherent structures.

DMD is a data-driven method, which relies on measurements (also called snapshots) collected from a dynamic system. More specifically, consider measurement of a discrete-time dynamic system that is sampled with fixed sampling rate Δt, so that samples x_k are collected at regular time intervals as $x_k = x(k \cdot \Delta t)$ where $x \in \mathbb{R}^n$, $k = 1, 2, ..., m$, and m is the number of measurements. The sequential measurements x_k and x_{k+1} are assumed to be related by a linear operator as:

$$x_{k+1} = Ax_k \tag{4.1}$$

where the operator $A \in \mathbb{R}^{n \times n}$ is the linearized dynamics matrix which maps the relationship between the sequential measurements. The DMD algorithm constructs a low-rank approximation of A that minimizes $||x_{k+1} - Ax_k||_2$ for samples $k = 1, 2, ..., m-1$, which can be identified from the given measurements (Kutz et al., 2016; Proctor, Brunton, and Kutz, 2016).

To reduce the errors in this approximation, it is possible to arrange the m measurements into two large data matrices as:

$$X = \begin{bmatrix} | & | & & | & | \\ x_1 & x_2 & \dots & x_{m-2} & x_{m-1} \\ | & | & & | & | \end{bmatrix}, X' = \begin{bmatrix} | & | & & | & | \\ x_2 & x_3 & \dots & x_{m-1} & x_m \\ | & | & & | & | \end{bmatrix} \tag{4.2}$$

where X' is the time-shifted measurement matrix of X. The mapping operator between these rearranged matrices can be defined as:

$$A = X'X^{\dagger} \tag{4.3}$$

where $(\cdot)^{\dagger}$ is the Moore-Penrose pseudoinverse, and this solution minimizes $||X' - AX||_F$, with $||\cdot||_F$ denoting Frobenius norm (Tu et al., 2014). The DMD of data pair (X, X') is given by the eigendecomposition of A, where the DMD modes and eigenvalues are the eigenvectors and eigenvalues of A, respectively (Tu et al., 2014).

However, in practice it may be difficult to compute the eigendecomposition of matrix A when its dimension n is large. Instead, the DMD can be efficiently obtained without an explicit representation of A (Tu et al., 2014). For this, rank-reduced representation can be accurately obtained via singular value decomposition (SVD). First, the rank-r approximation of X can be obtained with SVD as $X \approx U\Sigma V^*$, where $(\cdot)^*$ denotes the conjugate transpose, $U \in \mathbb{C}^{n\times r}$, $\Sigma \in \mathbb{C}^{r\times r}$, $V \in \mathbb{C}^{m\times r}$, and $n \gg r$. Subsequently, an approximation of the mapping operator can be defined as:

$$A \approx \tilde{A} \overset{\Delta}{=} U^*AU = U^*X'X^{\dagger}U = U^*X'V\Sigma^{-1} \tag{4.4}$$

where $\tilde{A} \in \mathbb{R}^{r\times r}$ defines a low dimensional representation the dynamic system matrix. Following, the eigendecomposition of $\tilde{A}$ defined by $\tilde{A}W = W\Lambda$ is carried out, where columns of $W \in \mathbb{C}^{r\times r}$ are the eigenvectors and $\Lambda \in \mathbb{C}^{r\times r}$ is a diagonal matrix containing eigenvalues. Last, the eigendecomposition of full-dimensional A can be reconstructed using W and Λ. In particular, the eigenvalues of A and $\tilde{A}$ are equivalent and the dynamic modes of A can be computed as (Tu et al., 2014):

$$\Phi = X'V\Sigma^{-1}W \tag{4.5}$$

As such, DMD allows for the efficient analysis of underlying system properties such as oscillation frequencies and amplitudes of each mode, without explicitly computing the full-dimensional operator A.

4.2.2 DMD of the Respiratory Signal and Image Analyses

In non-contrast-enhanced functional lung imaging, dynamic images of the lungs are obtained with fast acquisition methods. Conventionally, images in the order of hundreds are acquired with a frame rate of three to four images per second during free breathing to capture signal variations arising from respiration and cardiac pulsation. Afterward, the lung structures are aligned using non-rigid registration, enabling the observation of regional signal changes. Here, the non-rigid registrations were accomplished using fMRLung 3.0 software (Siemens Corporate Research) (Chefd'Hotel, Hermosillo, and Faugeras, 2001; Chefd'hotel, Hermosillo, and Faugeras, 2002).

For the application of DMD in functional imaging, each frame of the m measurements with $n_X \times n_Y = n$ pixels are vectorized, resulting in m vectors with size $n \times 1$.

Here, to further improve the noise resilience and to prevent rank deficiency limitations (Tu et al., 2014), DMD was implemented with data stacking. In data stacking, multiple time-shifted copies of the data are stacked into a larger augmented matrix to increase the rank of the measurement matrix. As such, data stacking helps mitigate rank deficiencies (Rot, Horvat, and Kosec, 2022) and can improve the accuracy of the reduced-order system in extraction of information (Alassaf and Fan, 2021). Afterward, $r = 15$ most dominant modes were identified with DMD, and the signal modulations caused by ventilation and perfusion were obtained as:

$$S_{vent} = \sum_{k=1}^{v} b_k \phi_k, \quad S_{perf} = \sum_{k=1}^{q} b_k \phi_k \tag{4.6}$$

where v and q indicate the number of identified respiratory and cardiac frequencies, b_k is the respective DMD mode amplitude, and ϕ_k is the respective DMD mode. Exemplary DMD modes obtained from a volunteer measurement are displayed in Figure 4.1 with their respective frequencies and mode amplitudes. Last, fractional ventilation map (hereafter referred to as ventilation map) and normalized perfusion map (hereafter referred to as perfusion map) were calculated as previously explained (Ilicak et al., 2022b; Kjørstad et al., 2014b). In this work, perfusion maps were normalized using the 99th percentile of voxels inside an area encompassing lungs including large vessels.

To comparatively demonstrate the performance of DMD, same dynamic acquisitions were processed using conventional FD and MP decompositions. For the FD method, scanner-reconstructed images were processed as previously described (Bauman et al., 2009), without the additional Hann filtering. For the MP method a reduced-rank MP decomposition was implemented to improve its robustness against noise described (Sarkar and Pereira, 1995). The input signal of MP was obtained from the summation of center of the images (Bauman and Bieri, 2017) without the low-pass and high-pass filtering operations. The MP rank was selected automatically (Sarkar and Pereira, 1995) and pencil parameter was set as $L = m/2$ to approach Cramér-Rao bound (Trinh and Overbye, 2019). For quantitative comparisons, mean functional map values over the lung parenchyma were calculated to assess dependency on the number of measurements. To this end, functional maps were obtained from measurement sets with varying lengths ℓ, where $\ell \in [50\ m]$ and the sets included measurements between $[1\ \ell]$. Then, the mean functional values were calculated over regions of interest (ROIs) encapsulating the lung parenchyma. The ROIs were obtained semi-automatically from magnitude images (Dirk-Jan Kroon, 2021), and if needed, were manually corrected. Differences between the dispersions of the mean values were assessed using Ansari-Bradley test (Ansari and Bradley, 1960) and were considered significant when $p < 0.05$.

4.2.3 Phantom Simulations

Simulations were performed on a digital lung phantom to assess the accuracy of the mean functional map amplitudes using different decomposition methods. To this end, the phantom was generated for $m = 480$ measurements and with three tissue types: background, large vessels, and lung parenchyma. For parenchymal tissue, ventilation and perfusion related signal variations were simulated according to modified Lujan formulation as described previously (Bauman and Bieri, 2017); whereas for large vessels only perfusion related signal variations were simulated. The phantom was evaluated for two cases: (i) a noise-free case with fixed respiratory

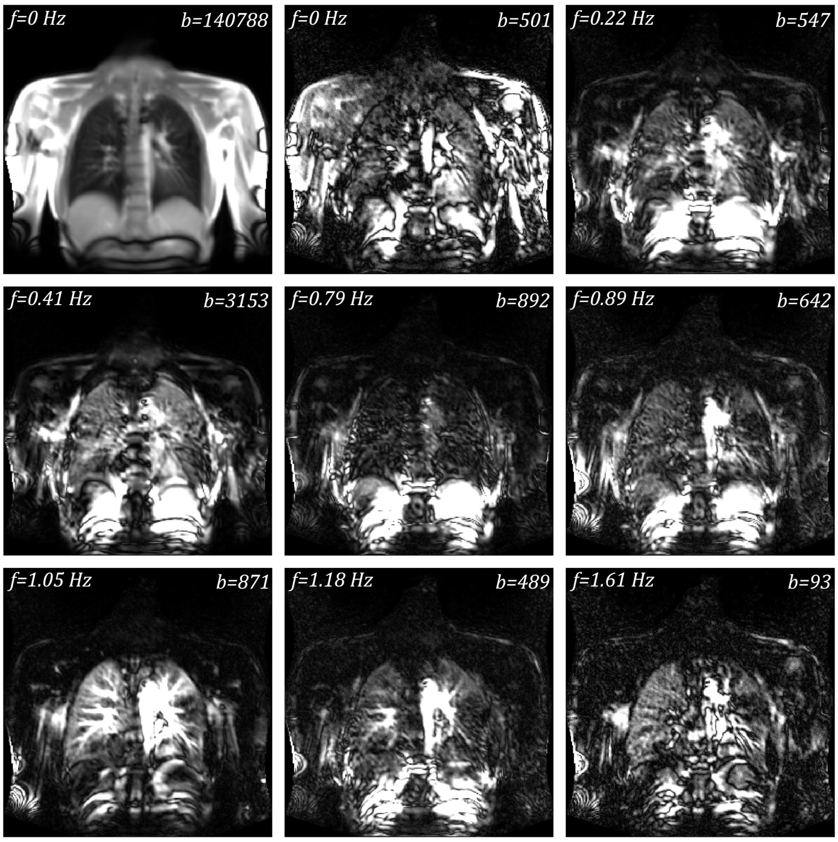

FIGURE 4.1: Representative DMD modes obtained from a volunteer measurement. The modes are obtained from a rank-15 approximation. Here, only a single component of complex conjugate pairs is displayed. The corresponding mode frequencies (f) and mode amplitudes (b) are also displayed overlaid on the modes. The DMD algorithm provides physically interpretable results while identifying dominant spatiotemporal features; such as ventilation and perfusion related signal variations together with secondary motions or harmonics. Here, mode with $f = 0.41$ Hz was associated with ventilation related signal changes, whereas modes with $f = 1.05$ Hz and $f = 1.18$ Hz were associated with perfusion related signal changes.

and cardiac frequencies at $f_V = 0.2$ Hz and $f_Q = 1.0$ Hz; respectively, to replicate an idealized case, and (ii) a noisy case with varying respiratory and cardiac frequencies to replicate a more realistic acquisition. For the second case, separate noise instances with a bivariate Gaussian distribution were added to simulated magnitude images to attain acquisition SNR=50 for parenchymal tissues (Ilicak et al., 2017; Bauman, Pusterla, and Bieri, 2019). To create varying frequencies, the simulations started with a section at $f_V = 0.2$ Hz and $f_Q = 1.0$ Hz and and ended with a section at $f_V = 0.18$ Hz and $f_Q = 0.9$ Hz. Between these sections of constant frequencies, a linear decrease in respiration and cardiac frequencies was prescribed for a duration of 20 samples. The generated phantoms and the simulated signals for lung parenchyma are displayed in Figure 4.2.

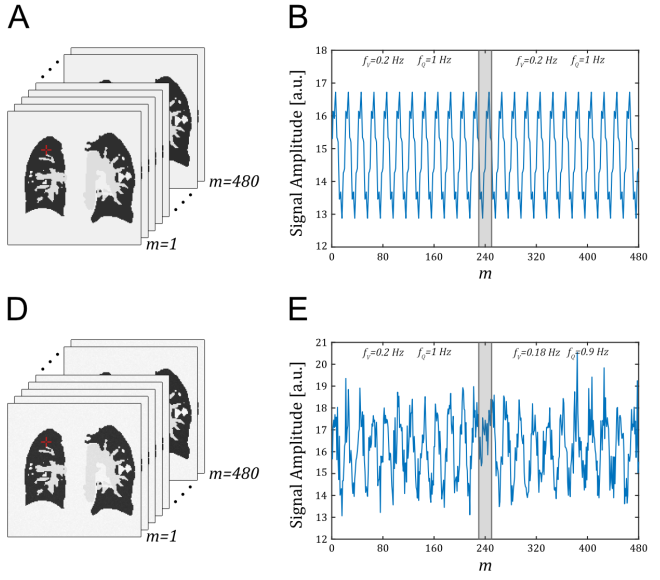

FIGURE 4.2: (A) A noise-free digital phantom was generated with three different tissue types for $m = 480$ different measurements. Signal changes associated with ventilation and perfusion were simulated in parenchymal tissues, whereas for large vessel structures, perfusion related signal changes were simulated. (B) Signal changes across m are shown for a pixel in the parenchymal tissue (shown in (A) with red crosshair). (C) Ventilation and perfusion values were estimated using FD, MP, and DMD for measurement sets with different lengths, $\ell \in [50\ 480]$, and the mean values were obtained by averaging across parenchymal tissues. (D) For a more realistic case, bivariate Gaussian noise was added to the phantom, and respiratory and cardiac frequencies were varied. (E) Frequencies were linearly decreased during a 20-sample duration (shown with gray zone). The signal changes across m are shown for a pixel in parenchymal tissue (shown in (D) with red crosshair). (F) Ventilation and perfusion values were estimated using FD, MP, and DMD for measurement sets with $\ell \in [50\ 480]$, and mean values were obtained by averaging across parenchymal tissues.

4.2.4 MRI Data Acquisitions

All volunteer measurements were performed on a 1.5T scanner (Magnetom Aera, Siemens Healthineers, Erlangen, Germany) using a conventional 2D bSSFP pulse sequence. Five healthy volunteers underwent free breathing MRI scans in supine position after obtaining written informed consent, and the imaging protocols were approved by the local ethics committee. A single slice location was imaged in coronal orientation for each volunteer, and the slices were positioned posterior to the heart. The sequence parameters consisted of FOV=450×450 mm^2, 15 mm slice thickness, TE/TR=0.80/1.88 ms, α=50°, matrix size = 128×128 (256×256 with scanner interpolation), parallel imaging with GRAPPA factor 3 with 24 integrated calibration lines, asymmetric echo readout, partial Fourier=6/8, bandwidth=1302 Hz/px. The overall acquisition rate was 3.2 images/s with a 200 ms pause between measurements. The initial six images were omitted to eliminate transient state behavior (Bauman et al., 2009), and the remaining 250 images were analyzed to generate ventilation and perfusion maps.

4.3 Results

The proposed method is first demonstrated on simulated phantom measurements. Mean ventilation and perfusion amplitudes estimated with FD, MP, and DMD using varying ℓ are shown in Figure 4.2. We observe that even under idealistic conditions without frequency variations or noise, the FD method shows dependency on ℓ. In comparison, both MP and DMD are able to extract amplitude information successfully without showing such a dependency. However, under more realistic conditions, we observe that MP method is not able to estimate the amplitudes successfully, resulting in erroneous estimation of ventilation and perfusion values. In comparison, DMD is able to extract both of these values more robustly compared to both FD and MP methods. In particular, we observed that DMD significantly reduced variations in estimated amplitude in ventilation maps ($p < 0.05$), and significantly reduced variations in perfusion maps after the shift in cardiac frequency ($p < 0.05$).

Next, we demonstrated DMD on in vivo bSSFP measurements. Representative mean ventilation and perfusion amplitudes estimated with FD, MP, and DMD across ℓ are shown for a volunteer in Figure 4.3. As expected, FD method shows a clear dependence on ℓ which leads to oscillations in the estimated amplitudes. The MP reduces this dependency; yet it suffers from inconsistencies across different ℓ, leading to sudden deviations in the estimated amplitudes. In contrast, DMD methods yields noticeably improved ventilation and perfusion estimation and further reduces the variations due to differences in ℓ.

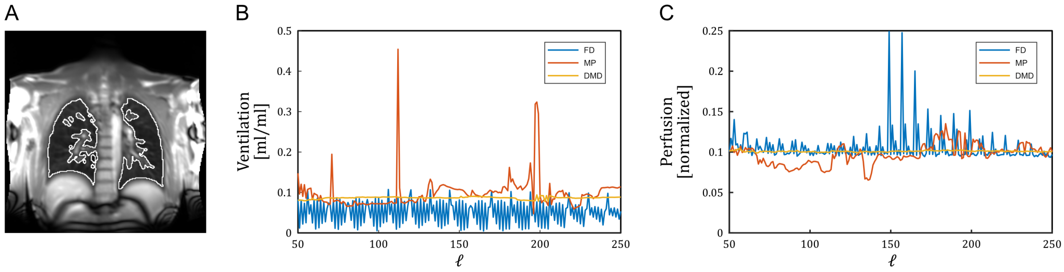

FIGURE 4.3: Mean ventilation and perfusion results from a volunteer were calculated over the lung parenchyma across measurement sets with different lengths $\ell \in [50\ 250]$. (A) The selected ROI (displayed in white) encapsulating the lung parenchyma is shown overlaid on a representative bSSFP magnitude image. The mean ventilation and perfusion results are displayed in (B) and (C), respectively. FD shows a dependency on ℓ, resulting in oscillations in estimated amplitudes. MP decreases this dependency on ℓ and reduces the associated oscillations; however, it occasionally manifests sudden inconsistencies along consecutive measurements in the estimation of amplitudes. In contrast, the proposed DMD method further reduces the oscillatory behavior, and can estimate respective amplitudes robustly across different ℓ.

Figure 4.4 depicts ventilation and perfusion maps obtained from a volunteer for $\ell = 174, 175, 176$ to show functional map consistency across measurements with sequential lengths. Maps obtained with FD shows a dependence on , which results in inconsistent estimation of ventilation values. Furthermore, for ℓ perfusion map suffers from deteriorated image quality. The MP reduces the variations observed in FD, yet it suffers from inconsistencies in amplitude estimations, as observed in the ventilation map for $\ell = 176$. In contrast, the proposed DMD method reliably obtains ventilation and perfusion maps and displays consistent amplitudes across sequential ℓ.

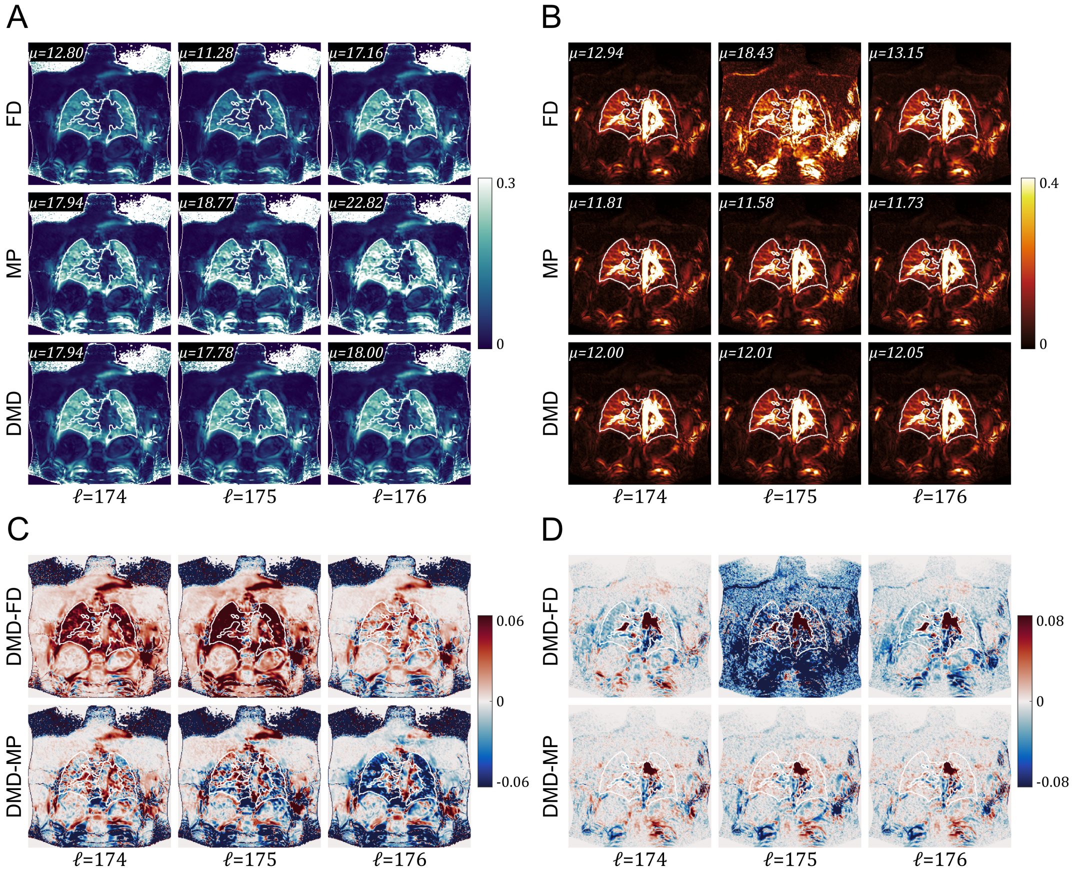
A
FD
MP
DMD
μ=12.80
μ=11.28
μ=17.16
μ=17.94
μ=18.77
μ=22.82
μ=17.94
μ=17.78
μ=18.00
0.3
0
ℓ=174
ℓ=175
ℓ=176
B
FD
MP
DMD
μ=12.94
μ=18.43
μ=13.15
μ=11.81
μ=11.58
μ=11.73
μ=12.00
μ=12.01
μ=12.05
0.4
0
ℓ=174
ℓ=175
ℓ=176
C
DMD-FD
DMD-MP
0.06
0
-0.06
ℓ=174
ℓ=175
ℓ=176
D
DMD-FD
DMD-MP
0.08
0
-0.08
ℓ=174
ℓ=175
ℓ=176

FIGURE 4.4: (A) Ventilation and (B) perfusion maps obtained from a volunteer for three sequential ℓ. Additionally, the mean ventilation and perfusion values are calculated over lung parenchyma (shown in white) and displayed overlaid on respective maps (mean values are scaled by a factor of 100 for better visualization). Similarly, ventilation map differences (C) and perfusion map differences (D) are illustrated to highlight the spatial differences between DMD and competing methods. Functional maps obtained with FD leads to stability issues in estimated amplitudes depending on ℓ; and maps obtained with MP indicate inconsistent estimation of amplitudes, as evident in the ventilation map for $\ell = 176$. In comparison, DMD displays consistent results in both ventilation and perfusion maps across all ℓ.

The mean ventilation and perfusion values obtained using FD, MP, and DMD averaged over ℓ are listed for all volunteers in Table 4.1. Overall, we observe that DMD can reduce the variations in estimated amplitudes in both ventilation and perfusion maps. In particular, employing the DMD resulted in significantly lower dispersion in both ventilation and perfusion map amplitudes (except for perfusion values of Volunteer 3) when compared with MP ($p < 0.05$).

4.4 Discussion

Here, DMD algorithm was investigated to obtain regional pulmonary ventilation and perfusion information from dynamic acquisitions. Our results indicate that

TABLE 4.1: Mean and standard deviation across different measurement lengths $\ell \in [50\ 250]$ of average ventilation and perfusion values estimated with FD, MP and DMD methods for all volunteers. The average functional values at each ℓ are calculated over ROIs encompassing lung parenchyma, and the values are scaled by a factor of 100 for better visualization of differences.

Mean Ventilation [ml/ml×100]

Volunteer	FD	MP	DMD
1	4.20±2.20	7.74±2.00	12.43±0.65
2	5.86±2.94	15.81±8.10	11.11±2.13
3	6.95±3.79	10.55±9.91	11.87±0.31
4	9.80±5.24	25.31±21.19	15.99±2.00
5	5.21±2.93	9.89±4.21	8.67±0.29

Mean Perfusion [normalized×100]

Volunteer	FD	MP	DMD
1	10.45±0.61	12.45±0.59	10.55±0.43
2	11.33±1.75	9.23±1.90	9.35±0.51
3	12.35±2.22	12.89±2.71	13.74±2.67
4	13.78±2.59	13.28±3.93	11.57±0.63
5	10.63±1.95	9.76±1.25	10.18±0.08

DMD is capable of successfully estimating functional information across different number of measurements, while significantly reducing variations in estimated map amplitudes. Additionally, our results suggest that DMD can generate functional maps consistently for lower values of ℓ, which may potentially reduce scan times. Nonetheless, this study focused on healthy volunteers; therefore, further investigations are needed to assess the lower limits of ℓ for diagnostic image quality in clinical populations.

Regarding the performance differences between MP and DMD, under specific conditions the MP and DMD methods are expected to produce the same results (Pogorelyuk and Rowley, 2018). An example of this can be seen in the noise-free phantom with constant frequencies in Figure 4.2. Nevertheless, under more realistic conditions, we observe that DMD can estimate respective amplitudes and frequencies more robustly, which can be explained by the differences in the input data. While the DMD method is able to utilize the complete measurements in the vectorized form, the MP method requires the summation of a central portion of the image, leading to reduction in the available information.

Despite the linearity assumption between sequential measurements, DMD has been linked to nonlinear dynamics via Koopman operator theory (Proctor, Brunton, and Kutz, 2016). More specifically, it has been shown that the DMD algorithm is capable of approximating the modes of infinite-dimensional linear Koopman operator, which can be defined to represent the dynamics of any nonlinear system (Kutz et al., 2016; Mohapatra and Overbye, 2016). Therefore, for a nonlinear dynamic system, the DMD algorithm provides a linear mapping that best approximates the nonlinear dynamics (Schmid et al., 2011; Rot, Horvat, and Kosec, 2022). As such, DMD can be utilized to analyze a nonlinear system (Tu et al., 2014), as it might be the case for in vivo ventilation and perfusion measurements (Bondesson et al., 2019).

In this work, the DMD was utilized with a fixed rank to identify dominant modes. While the implementation of DMD with $r = 15$ was able to identify ventilation and perfusion related changes in all volunteers, higher rank values might be needed to identify spatiotemporal patterns in more complex breathing and/or cardiac patterns. Therefore, future investigations are warranted to adaptively adjust the rank value based on the input data.

The DMD algorithm is known to have limitations in characterizing transient time phenomena (Kutz et al., 2016). While the DMD algorithm is able to provide accurate assessment during continuous respiration and cardiac pulsation, it is important to note that breath holding maneuvers may affect the results. Additionally, DMD is computationally more intensive than FD or MP methods. Despite this, DMD analysis of an in vivo dataset with 250 measurements lasts approximately 5 seconds, and remains shorter than the computing times required for non-rigid registration (Ljimani et al., 2021).

Regarding the pulse sequence selection, the proposed method was demonstrated on dynamic images obtained using the conventional 2D balanced SSFP (bSSFP) pulse sequence due to its wide availability. Nevertheless, the DMD algorithm is independent of the underlying pulse sequence and can be utilized with other pulse sequences capable of dynamic acquisition, such as standard or transient spoiled gradient echo (GRE) (Voskrebenzev et al., 2018; Bauman, Pusterla, and Bieri, 2019), ultrafast SSFP (Bauman, Pusterla, and Bieri, 2016), tiny golden angle UTE (Balasch et al., 2020), or multi-acquisition bSSFP (Ilicak et al., 2022b).

Last, the proposed method can be advanced by incorporating additional priors to DMD. Recently, extensions to DMD have been proposed to improve the eigenvalue prediction, such as forward-backward algorithm (Dawson et al., 2016) to improve noise resilience, multiresolution DMD algorithm to sift out information at different time-scales (Kutz, Fu, and Brunton, 2016) akin to low-rank plus sparse methods (Otazo, Candès, and Sodickson, 2015; Ilicak, Saritas, and Çukur, 2022), or compressed sensing DMD algorithms (Jovanović, Schmid, and Nichols, 2014; Bai et al., 2020) to relax sampling requirements. These extensions can be incorporated to exploit the low-rank and sparsity properties present in the dynamic lung MR images (Ilicak et al., 2019b; Ilicak et al., 2020) to further improve the performance of DMD algorithm.

4.5 Conclusion

We have presented a data-driven method for obtaining regional pulmonary ventilation and perfusion information from a series of dynamic acquisitions. The proposed method employs DMD to robustly identify dominant coherent spatiotemporal features. Compared to FD and MP methods, it improves the accuracy in the estimation of ventilation and perfusion related signal changes. Overall, DMD method is demonstrated to be a viable option for spectral analysis in dynamic MR acquisitions and may advance the diagnostic potential of non-contrast-enhanced pulmonary functional imaging.

4.6 Appendix

The DMD algorithm for functional lung imaging and simulated phantom data is openly available at https://github.com/EfeIlicak/DMD_Lung.

Chapter 5

Functional lung imaging of 2-year-old children after congenital diaphragmatic hernia repair using dynamic mode decomposition

This chapter is based on the following manuscript submitted to *European Radiology* on 19.04.2023: Efe Ilicak[1], Greta Thater[1], Safa Ozdemir, Jascha Zapp, Lothar R. Schad, Stefan O. Schoenberg, Frank G. Zöllner[2], Meike Weis[2]. "Functional lung imaging of 2-year-old children after congenital diaphragmatic hernia repair using dynamic mode decomposition."

5.1 Introduction

Congenital diaphragmatic hernia (CDH) belongs to rare diseases and is caused by a developmental defect, which occurs in 1 of 2000-5000 live births (Oluyomi-Obi, Van Mieghem, and Ryan, 2017). CDH is characterized by herniation of abdominal organs into the thoracic cavity and results in impaired lung development, followed by irreversible hypoplasia of the pulmonary parenchyma and vasculature (Weidner et al., 2014). Although advances in understanding and treatment have improved survival rates, CDH remains to cause significant morbidity and mortality (Wong et al., 2018; IJsselstijn et al., 2018). Since lung morbidity can show a wide range of severity after CDH repair, periodic structured follow-up programs in specialized centres are strongly recommended to identify and treat the development of functionally significant deformities to extend the patients life expectancies (Section on Surgery and the Committee on Fetus and Newborn, 2008; Lewis et al., 2022).

To obtain pulmonary functional information, several studies have suggested the use of scintigraphical measurements (Hayward et al., 2007; Okuyama et al., 2006). With scintigraphy, regional distribution of ventilation (V), perfusion (Q), and their mismatch in CDH patients can be quantified (Hayward et al., 2007; Björkman et al., 2011; Dao et al., 2020). In these studies, it has been demonstrated that lung perfusion is significantly reduced in the affected ipsilateral lung in comparison to the contralateral lung, and ventilation/perfusion (V/Q) mismatch continues to worsen after CDH repair. Therefore, many centres recommend scintigraphical V/Q measurements to predict long-term pulmonary morbidity and functional outcome (Dao et al., 2020; Sanchez-Crespo, 2019). However, scintigraphical measurements do not offer morphological information and impose a radiation burden on patients. Subsequently, safety concerns regarding repeated radiation exposure and the need for childrens cooperation in the administration of radioactive gases have limited the application of scintigraphy imaging in pediatric patients (Sanchez-Crespo, 2019).

---

[1] Efe Ilicak and Greta Thater contributed equally to this work.

[2] Frank G. Zöllner and Meike Weis contributed equally to this work.

Other studies have recommended using MRI scans to evaluate the degree of structural damage and grade lung function morbidity without the need for ionizing radiation (Abolmaali et al., 2010; Zöllner et al., 2012; Walkup, Higano, and Woods, 2019; Zanette et al., 2022). With dynamic contrast-enhanced (DCE) MRI, quantitative lung perfusion parameters, such as pulmonary blood flow (PBF) or pulmonary blood volume (PBV) can be measured in addition to morphological imaging during the same examination (Weidner et al., 2014). In DCE-based studies (Weidner et al., 2014; Weis et al., 2016b; Groß et al., 2021), it has been shown that the affected lung displays impaired perfusion after CDH repair. More specifically, restricted lung development is reflected by lower PBF and PBV values in the ipsilateral lung, and perfusion differences between ipsilateral and contralateral lungs are observable. Although DCE-based studies have shown promising results, growing concerns about the safety of gadoliniumbased contrast agents and the inability to repeat measurements in cases of patient motion or technical difficulties limit the usefulness of DCE-based imaging (Edelman and Koktzoglou, 2019).

As an alternative to the DCE-based methods, non-contrast-enhanced methods have been developed to evaluate lung function by exploiting periodic signal intensity changes associated with ventilation and perfusion (Bauman et al., 2009; Bauman and Bieri, 2017; Klimeš et al., 2019). Recently, these methods have been utilized to investigate lung function in adults (Kunz et al., 2021) and in pediatric patients with cystic fibrosis (Nyilas et al., 2019; Nyilas et al., 2017; Couch et al., 2021). However, these techniques have not been investigated in CDH patients.

The aims of this study are twofold. First, we investigate the feasibility of a non-contrast-enhanced MRI method for obtaining ventilation and perfusion values in 2-year-old patients after CDH repair. To this end, we use commonly available 2D balanced steady-state free precession (bSSFP) pulse sequence to acquire dynamic acquisitions together with a recently developed post-processing method called dynamic mode decomposition (DMD) to obtain pulmonary functional maps. Second, we investigate whether there are observable differences between the ipsilateral and contralateral sides with the DMD MRI method. Furthermore, we identify whether there is a relationship in perfusion ratios of lungs between DMD-based perfusion imaging and DCE-based perfusion imaging.

5.2 Materials and methods

5.2.1 Patients

Fifteen patients after CDH repair were investigated in our department according to the local follow-up program, in which an MRI examination is included at the age of two years. Detailed patient demographics are listed in Table 5.1. For all children, written informed consent was obtained from the parents. The study was approved by the local research ethics committee. The non-contrast-enhanced protocols were added to the end of the follow-up procedure before the contrast-enhanced acquisitions. Among the patient population, four were measured with Protocol A, two were measured with Protocol B, and nine were measured with both protocols (see below for protocol details).

TABLE 5.1: Patient demographics.

Patient No.	CDH Location	ECMO Status	Protocol	Sex	Age (weeks)	Weight (kg)	Height (cm)
1	Left	No	A	Female	101	11.4	84
2	Left	Yes	A	Female	104	7.7	80
3	Left	Yes	A & B	Male	115	19	106
4	Right	Yes	A	Female	108	9.5	85
5	Left	Yes	A & B	Male	105	12.8	86
6	Left	Yes	A & B	Female	109	11.6	83
7	Left	No	A & B	Female	107	11.7	93
8	Left	Yes	A	Female	109	10	92
9	Left	Yes	A & B	Male	106	15	93
10	Right	No	A & B	Female	103	10.3	83
11	Left	No	A & B	Female	103	9.6	83
12	Left	No	A & B	Female	116	11	85
13	Right	Yes	A & B	Male	117	10	68
14	Left	No	B	Female	109	13.5	120
15	Right	Yes	B	Male	105	10.7	88

5.2.2 DMD-based Functional Pulmonary MRI

Non-contrast-enhanced functional lung imaging methods rely on dynamic acquisitions to capture signal variations arising from respiration and cardiac pulsation. To this end, imaging protocols with sufficiently high temporal resolution are employed during free-breathing to enable the observation of periodic signal variations. As such, ventilation- and perfusion-weighted information can be obtained without breathing manoeuvres or administration of contrast agents. Commonly, 2D bSSFP or gradient echo-based pulse sequences are used for rapidly acquiring lung images, and afterwards, lung structures are aligned using non-rigid registration software (Ljimani et al., 2021). Subsequently, registered time-series images are analysed to obtain regional ventilation and perfusion information.

In this work, a recently developed publicly available method based on DMD is utilized to analyse the time-series data to obtain functional maps robustly from dynamic acquisitions (Ilicak et al., 2023). In essence, DMD is a data-driven modal decomposition algorithm capable of identifying dominant spatiotemporal structures latent within time-series data (Tu et al., 2014; Kutz et al., 2016; Kunert-Graf et al., 2019). As such, DMD can determine the underlying oscillation frequencies and amplitudes in dynamic MR acquisitions, rendering it suitable for the identification of ventilation- and perfusion-related signal changes. With DMD MRI, dynamic MR images are analysed to identify ventilation and perfusion modes, and the ensuing fractional ventilation and normalized perfusion maps are calculated as previously explained (Ilicak et al., 2023). The overall workflow is illustrated in Figure 5.1.

5.2.3 MRI Protocols

MRI examinations were performed using a 1.5T system (Magnetom Aera, Siemens Healthineers, Germany). A combination of spine array, head-neck coil, and body phased-array coil was used. Patients underwent free-breathing MRI scans in supine position after an anaesthetist, who was present during the whole examination, has performed sedation using propofol. The lung function was assessed using a DMD

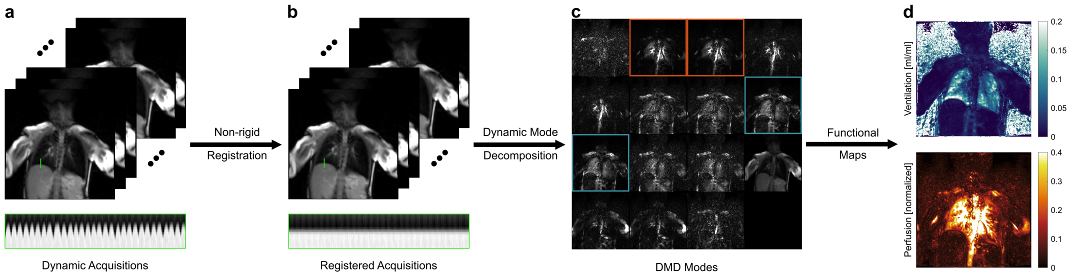

FIGURE 5.1: Workflow of the DMD MRI method. (**a**) Dynamic acquisitions are obtained during free-breathing to capture signal variations stemming from respiration and pulsation. (**b**) Lung structures are aligned using a non-rigid registration technique to enable the observation of regional parenchymal signal changes. Movements across measurements for a region (displayed with green line) before and after registration are also shown below acquisitions. (**c**) Registered time-series images are analysed using dynamic mode decomposition (DMD), and modes related to ventilation (displayed with blue boxes) and perfusion (displayed with red boxes) are identified. (**d**) Using these identified modes, ventilation and perfusion maps are calculated. Overall, functional maps can be obtained from dynamic acquisitions without the need for breathing manoeuvres or administration of contrast agents.

MRI, as well as DCE-based perfusion imaging. For DMD MRI, dynamic images of the lung were acquired using bSSFP sequences adapted to accommodate pediatric patients with smaller field-of-view (FOV) and higher temporal resolution requirements; whereas for the DCE method, images were acquired using time-resolved angiography with stochastic trajectories (TWIST) sequence as previously described (Weidner et al., 2014).

For non-contrast-enhanced imaging, two different bSSFP protocols (Table 5.2) were utilized to image at a single location. Protocol A was acquired using a larger FOV to improve the SNR characteristics and to maximize temporal resolution, whereas Protocol B was using a smaller FOV with a higher in-plane resolution, at the expense of SNR and temporal resolution. For both protocols, acquired slices were positioned posterior to the heart in the anterior-posterior dimension. The following parameters were common between protocols: flip angle $\alpha = 50^\circ$, pause between measurements=0.07 s, phase partial Fourier=6/8, parallel imaging with GRAPPA factor 3 using 24 integrated autocalibration lines. For both protocols, the initial six images were discarded due to transient state effects (Bauman et al., 2009), and the remaining 274 images were analysed to obtain functional maps. Image registration was performed using a prototype non-rigid registration software, fMRLung 3.0 (Siemens Corporate Research, Princeton, NJ, USA) (Chefd'Hotel, Hermosillo, and Faugeras, 2001; Chefd'hotel, Hermosillo, and Faugeras, 2002).

DCE-based perfusion imaging was performed after the bSSFP acquisitions, using TWIST sequence with the following parameters: FOV=416×416 mm^2, voxel resolution = 1.9×1.9 mm^2, slice thickness=2 mm, TE/TR=0.86/2.94 ms/ms, $\alpha = 30^\circ$, 56 slices per slab, view-sharing of 17% in the central and 20% in the outer region, parallel imaging with GRAPPA factor 2 in both phase encoding directions using 24 integrated autocalibration lines, temporal resolution of 1.5 s. Contrast agent (Dotarem, Guerbet) was administered after the acquisition of five baseline images, with a dosage of 0.05 mmol/kg body weight, diluted with the same volume of

TABLE 5.2: Relevant parameter list of two different bSSFP protocols used for imaging. *Voxel resolution with interpolation.

	Protocol A	**Protocol B**
FOV (mm×mm)	384×384	280×280
Voxel Resolution* (mm×mm)	1.5×1.5	1.1×1.1
Slice Thickness (mm)	12	12
TE/TR (ms/ms)	0.90/2.12	0.99/2.31
Acquisition Rate (images/s)	5.14	4.87

sodium chloride and followed by a sodium chloride bolus of 10 mL. Perfusion quantification was done using deconvolution approach with an in-house certified OsiriX plugin (Zöllner et al., 2016) as previously described (Groß et al., 2021).

5.2.4 Data Analyses

To investigate image quality, quantitative analyses were performed on the magnitude images and functional maps. To this end, regions of interest (ROIs) containing lung parenchyma were manually segmented from magnitude images while excluding large vessels, and the quantitative metrics were calculated from the ROIs. The bSSFP protocols were compared using signal-to-noise ratio (SNR) and contrast-to-noise ratio (CNR) analyses. The SNR values were estimated on registered magnitude images based on the power spectrum of the time-series (Bauman, Pusterla, and Bieri, 2019), and frequencies above 2.2 Hz were considered noise. The CNR values were calculated on ventilation and perfusion maps and were defined as the ratio of mean functional amplitudes within the lung parenchyma and a homogeneous background region selected within liver tissue.

To investigate functional differences between lungs, ventilation and perfusion ratios between the ipsilateral and contralateral lungs (denoted as V_{Ratio} and Q_{Ratio} respectively) were calculated. For this purpose, mean functional values within the ROIs were obtained for each lung (Kassner et al., 2018), and the ratios between the ipsilateral and contralateral lungs were calculated. Additionally, linear correlations and agreements between V_{Ratio} and Q_{Ratio} values obtained with Protocol A and Protocol B were assessed.

TWIST-based pulmonary perfusion was analysed by manually segmenting both lungs separately for each slice, while leaving out the mediastinal structures. The arterial input function was derived from a ROI placed in the main stem of pulmonary artery and the quantitative pulmonary blood volume (PBV) and pulmonary blood flow (PBF) parameters were calculated cumulatively from the segmented slices.

Lastly, DMD-based perfusion results were compared with TWIST-based PBF values to investigate the agreement between these methods. For this purpose, linear correlations, and agreements between TWIST-based perfusion ratio PBF_{Ratio} and DMD-based perfusion ratio values (Q_{Ratio}) obtained with both protocols were assessed.

5.2.5 Statistical Analyses

For statistical analysis, all data were evaluated using the Kolmogorov-Smirnov test to check for normality. Subsequently, the differences in SNR, CNR, and functional ratios between Protocol A and Protocol B were compared using the Wilcoxon-Mann-Whitney test. The differences in DMD-based functional values between ipsilateral and contralateral lungs, as well as differences between DMD-based perfusion and

TABLE 5.3: Quantitative measurements obtained from acquisition Protocol A. The average values are reported as mean ± standard deviation across patients.

Patient No.	SNR	CNR_{Vent}	CNR_{Perf}	V_{Ratio}	Q_{Ratio}
1	49.49±17.32	7.52	2.07	0.63	0.62
2	60.22±25.61	5.72	6.43	0.55	0.87
3	79.56±37.62	16.26	8.35	0.73	0.82
4	31.49±12.83	15.09	3.05	0.93	0.71
5	32.99±14.49	14.73	5.32	0.57	0.75
6	32.04±16.17	13.47	5.71	0.75	0.61
7	38.32±13.63	14.56	9.46	0.94	1.38
8	25.14±10.28	10.71	4.23	0.88	0.69
9	33.41±11.56	12.27	5.84	0.93	0.65
10	33.47±13.56	3.83	4.87	0.93	0.47
11	47.27±16.74	10.06	5.40	0.85	0.56
12	47.43±21.70	9.88	6.82	1.15	0.43
13	39.30±12.86	7.08	5.05	1.11	0.60
Average	42.32±14.71	10.86±3.95	5.58±1.97	0.84±0.19	0.70±0.24

TWIST-based perfusion ratios were compared using paired two-sided Wilcoxon signed rank tests. To assess linear correlations and agreements between functional ratios, Pearsons correlation and Bland-Altman analyses were performed, where the biases were assessed using t-test. In all tests, $p < 0.05$ was considered to be statistically significant. The resulting correlation coefficient (r) was interpreted as: 0.00-0.19 negligible; 0.20-0.39 weak correlation; 0.40-0.59 moderate correlation; 0.60-0.79 strong correlation; and 0.80-1.00 very strong correlation. All statistical analyses were performed using MATLAB (MathWorks, Natick, MA, USA).

5.3 Results

5.3.1 Feasibility of pediatric DMD MRI

Representative cross-sections of bSSFP acquisitions obtained using both protocols are shown in Figure 5.2 for a patient with left-sided herniation and extracorporeal membrane oxygenation therapy (ECMO) treatment. Additionally, frequency spectrums calculated from registered images using the mean signal intensity are also displayed. As illustrated, both protocols can distinguish frequency peaks associated with respiratory and cardiac cycles. The SNR and CNR values of protocols are listed in Tables 5.3 and 5.4 for Protocol A and Protocol B, respectively. As expected, Protocol A results in higher SNR values compared to Protocol B; nonetheless, SNR and CNR differences between the protocols are not significant.

Figure 5.3 depicts exemplary modes obtained with the DMD from a patient measurement using Protocol A. Respective mode frequencies and mode amplitudes are also displayed overlaid on the modes. In our study cohort, ventilation frequencies ranged between 0.25-0.59 Hz, and perfusion frequencies ranged between 1.40-2.13 Hz. Overall, DMD analysis successfully identified dominant spatiotemporal features such as ventilation- and perfusion-related signal changes in all patients.

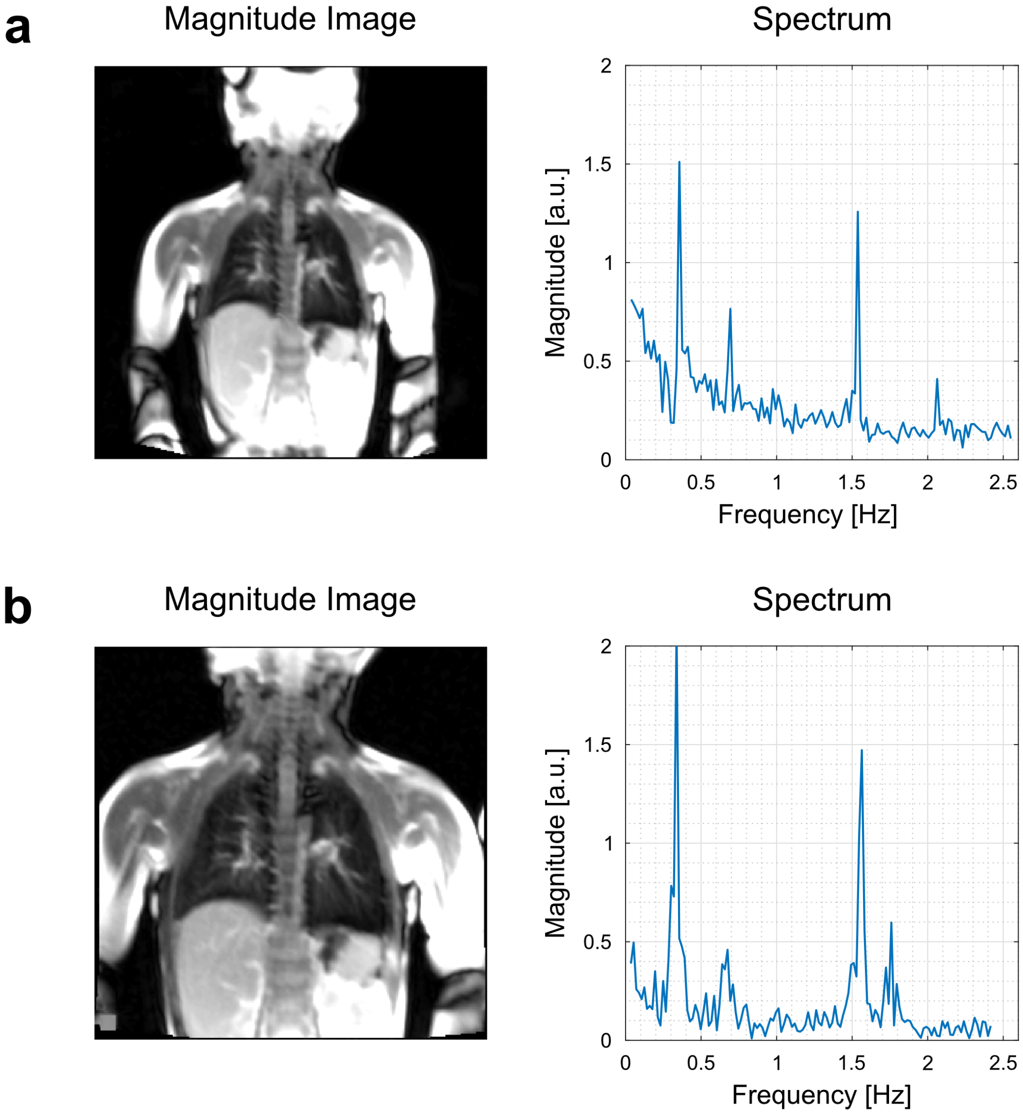
a
Magnitude Image
Spectrum
Magnitude [a.u.]
2
1.5
1
0.5
0
0
0.5
1
1.5
2
2.5
Frequency [Hz]
b
Magnitude Image
Spectrum
Magnitude [a.u.]
2
1.5
1
0.5
0
0
0.5
1
1.5
2
2.5
Frequency [Hz]

FIGURE 5.2: Exemplary magnitude images and frequency spectrums calculated from the acquisitions obtained with (**a**) Protocol A, and (**b**) Protocol B, from a CDH patient with left-sided hernia and ECMO treatment. The magnitude images are scaled to better visualize lung parenchyma. Both protocols are able to successfully detect frequency peaks associated with respiration ($\sim$ 0.35 Hz) and cardiac pulsation ($\sim$ 1.55 Hz).

5.3.2 DMD MRI-based pulmonary functional parameters

Illustrative ventilation and perfusion maps obtained from a patient are shown in Figure 5.4 for both protocols. Additionally, violin plots of functional values are presented to illustrate the distribution differences between ipsilateral and contralateral lungs. For both protocols, functional maps are successfully obtained using DMD analysis and differences between ipsilateral and contralateral lungs are visible. Nevertheless, when the bSSFP protocols are compared, Protocol B is able to display finer structures owing to its higher spatial resolution.

The ipsilateral to contralateral ventilation (V_{Ratio}) and perfusion (Q_{Ratio}) ratios obtained with DMD MRI are reported in Tables 5.3 and 5.4. The mean fractional

TABLE 5.4: Quantitative measurements obtained from acquisition Protocol B. The average values are reported as mean ± standard deviation across patients.

Patient No.	SNR	CNR_{Vent}	CNR_{Perf}	V_{Ratio}	Q_{Ratio}
3	41.44±17.42	18.63	3.92	0.70	0.83
5	24.05±13.82	11.87	3.96	0.51	0.77
6	19.37±11.01	13.39	5.27	0.75	0.70
7	27.01±10.32	10.35	9.77	1.05	1.24
9	27.90±12.43	11.75	5.25	0.95	0.54
10	33.13±20.61	5.37	4.21	0.88	0.50
11	39.61±16.54	5.44	5.71	0.79	0.64
12	35.34±18.96	7.98	4.25	1.13	0.44
13	32.58±12.28	9.48	8.70	0.95	0.57
14	36.13±10.36	15.77	7.36	0.89	0.92
15	24.31±11.75	16.07	4.41	1.02	0.71
Average	30.99±6.99	11.46±4.31	5.71±2.02	0.88±0.18	0.72±0.23

ventilation and normalized perfusion values obtained with DMD MRI for ipsilateral and contralateral lungs are reported in Tables 5.5 and 5.6 for Protocol A and B, respectively. On average, V_{Ratio} and Q_{Ratio} values are below 1, indicating reduced pulmonary functions in the ipsilateral lung compared to contralateral lung. Specifically, the V_{Ratio} values for Protocol A and Protocol B are 0.84±0.19 and 0.88±0.18, respectively. Similarly, the Q_{Ratio} values for Protocol A and Protocol B are 0.70±0.24 and 0.72±0.23. Moreover, our results indicate that for both protocols the ventilation and perfusion reductions observed in the ipsilateral lungs are statistically significant.

The Pearsons correlation and Bland-Altman analyses of functional ratios obtained through DMD MRI with Protocol A and Protocol B are visualized in Figure 5.5. For both V_{Ratio} and Q_{Ratio}, we observe a very strong correlation ($r = 0.92$ for ventilation ratios, and $r = 0.97$ for perfusion ratios) and a close agreement between two protocols without a significant bias or systematic difference.

5.3.3 TWIST-based pulmonary perfusion parameters

PBV and PBF parameters of ipsilateral and contralateral lungs as well as their ratios (PBV_{Ratio} and PBF_{Ratio}) obtained through TWIST method are reported in Table 5.7. Overall, the PBV_{Ratio} is 0.68±0.19, and PBF_{Ratio} ratio is 0.68±0.17, and both values indicate significantly lower perfusion in the ipsilateral lungs.

5.3.4 Comparisons between DMD-based perfusion and TWIST-based perfusion

A comparison of the DMD-based perfusion maps and the TWIST-based perfusion map is provided in Figure 5.6 for a patient with left-sided herniation with ECMO therapy. Additionally, ventilation maps obtained with DMD MRI are also displayed. For both methods, the reduction of perfusion values in the ipsilateral lung can be observed visually and quantitatively.

Pearsons correlation and Bland-Altman analyses between Q_{Ratio} and PBF_{Ratio} are visualized in Figure 5.7. Correlation coefficients are $r = 0.89$ for Protocol A, and $r = 0.90$ for Protocol B, indicating very strong correlations between Q_{Ratio} and

TABLE 5.5: Mean fractional ventilation (V, scaled by a factor of 100 for better visualization) and normalized perfusion (Q) results calculated over ipsilateral (V_{Ipsi}, Q_{Ipsi}) and contralateral (V_{Cont}, Q_{Cont}) lungs from images obtained with Protocol A. Their ratios (V_{Ratio} and Q_{Ratio}) are also reported. The average values are reported as mean ± standard deviation across patients.

Patient No.	V_{Ipsi} [ml/ml×100]	V_{Cont} [ml/ml×100]	V_{Ratio}
1	6.40±5.27	10.17±3.93	0.63
2	1.85±1.30	3.37±2.48	0.55
3	5.12±2.59	7.02±3.39	0.73
4	5.28±2.98	5.65±2.16	0.93
5	6.09±2.92	10.75±3.99	0.57
6	4.98±2.33	6.63±2.91	0.75
7	5.11±2.15	5.45±3.28	0.94
8	7.03±3.22	7.99±3.84	0.88
9	7.54±4.21	8.09±4.39	0.93
10	7.68±5.54	8.25±2.93	0.93
11	7.28±3.01	8.53±4.67	0.85
12	5.56±2.41	4.85±2.55	1.15
13	6.01±2.35	5.39±2.03	1.11
Average	5.84±1.54	7.09±2.14	0.84±0.19

Patient No.	Q_{Ipsi} [normalized]	Q_{Cont} [normalized]	Q_{Ratio}
1	0.11±0.07	0.17±0.10	0.62
2	0.27±0.23	0.31±0.19	0.87
3	0.26±0.20	0.32±0.14	0.82
4	0.24±0.13	0.34±0.25	0.71
5	0.27±0.16	0.36±0.16	0.75
6	0.27±0.15	0.45±0.13	0.61
7	0.35±0.16	0.25±0.13	1.38
8	0.24±0.15	0.34±0.17	0.69
9	0.37±0.20	0.56±0.19	0.65
10	0.13±0.08	0.27±0.14	0.47
11	0.26±0.19	0.46±0.15	0.56
12	0.22±0.15	0.50±0.20	0.43
13	0.38±0.17	0.63±0.21	0.60
Average	0.26±0.08	0.38±0.13	0.70±0.24

TABLE 5.6: Mean fractional ventilation (V, scaled by a factor of 100 for better visualization) and normalized perfusion (Q) results calculated over ipsilateral (V_{Ipsi}, Q_{Ipsi}) and contralateral (V_{Cont}, Q_{Cont}) lungs from images obtained with Protocol B. Their ratios (V_{Ratio} and Q_{Ratio}) are also reported. The average values are reported as mean ± standard deviation across patients.

Patient No.	V_{Ipsi} [ml/ml×100]	V_{Cont} [ml/ml×100]	V_{Ratio}
3	4.81±2.57	6.84±3.52	0.70
5	5.48±2.44	10.72±4.25	0.51
6	8.07±3.73	10.82±5.39	0.75
7	8.05±3.55	7.65±5.10	1.05
9	7.50±4.16	7.87±4.09	0.95
10	7.66±4.92	8.69±3.19	0.88
11	13.75±5.98	17.46±6.61	0.79
12	8.05±3.65	7.11±3.67	1.13
13	10.05±4.59	10.56±3.56	0.95
14	5.69±2.08	6.37±2.69	0.89
15	8.74±4.13	8.58±4.63	1.02
Average	7.98±2.45	9.33±3.12	0.88±0.18

Patient No.	Q_{Ipsi} [normalized]	Q_{Cont} [normalized]	Q_{Ratio}
3	0.13±0.11	0.16±0.06	0.83
5	0.15±0.09	0.19±0.11	0.77
6	0.18±0.11	0.26±0.10	0.70
7	0.22±0.11	0.17±0.09	1.24
9	0.22±0.13	0.41±0.16	0.54
10	0.09±0.08	0.19±0.09	0.50
11	0.19±0.19	0.29±0.10	0.64
12	0.15±0.12	0.33±0.13	0.44
13	0.26±0.13	0.45±0.18	0.57
14	0.21±0.18	0.22±0.09	0.92
15	0.14±0.10	0.20±0.16	0.71
Average	0.18±0.05	0.26±0.10	0.72±0.23

TABLE 5.7: Perfusion parameters obtained through DCE-based TWIST protocol.

Patient No.	PBV_{Ipsi} [ml/100ml]	PBV_{Cont} [ml/100ml]	PBV_{Ratio}
1	7.93±4.76	13.95±6.67	0.57
2	6.55±3.85	8.67±5.41	0.76
3	19.29±16.40	19.56±9.02	0.99
4	12.54±8.15	26.76±13.97	0.47
5	6.65±6.77	13.10±10.06	0.51
6	9.49±5.85	16.40±8.61	0.58
7	15.27±5.99	13.15±7.06	1.16
8	4.91±3.90	9.64±6.72	0.51
9	8.10±5.10	11.85±6.48	0.68
10	9.75±6.74	13.59±6.51	0.72
11	8.23±5.30	12.86±6.70	0.64
12	8.57±4.88	13.73±6.72	0.62
13	10.13±7.32	16.94±8.37	0.60
14	13.96±5.67	17.08±7.69	0.82
15	7.22±4.26	12.06±5.03	0.60
Average	9.91±3.84	14.62±4.40	0.68±0.19

Patient No.	PBF_{Ipsi} [ml/100ml/min]	PBF_{Cont} [ml/100ml/min]	PBF_{Ratio}
1	99.58±54.97	175.57±81.57	0.57
2	83.61±45.24	110.90±58.64	0.75
3	193.21±89.47	250.67±115.46	0.77
4	282.69±185.67	390.96±242.15	0.72
5	106.92±101.01	176.95±163.59	0.60
6	138.05±77.94	234.64±111.30	0.59
7	158.77±66.57	131.78±66.26	1.20
8	43.31±36.40	95.19±6.54	0.45
9	52.84±35.05	84.94±48.18	0.62
10	50.55±34.85	83.38±42.84	0.61
11	59.14±38.75	102.06±53.98	0.58
12	78.08±45.39	133.47±69.82	0.59
13	100.26±55.57	163.72±77.59	0.61
14	157.74±65.67	195.50±81.92	0.81
15	70.72±40.23	99.24±42.75	0.71
Average	111.70±65.17	161.93±82.61	0.68±0.17

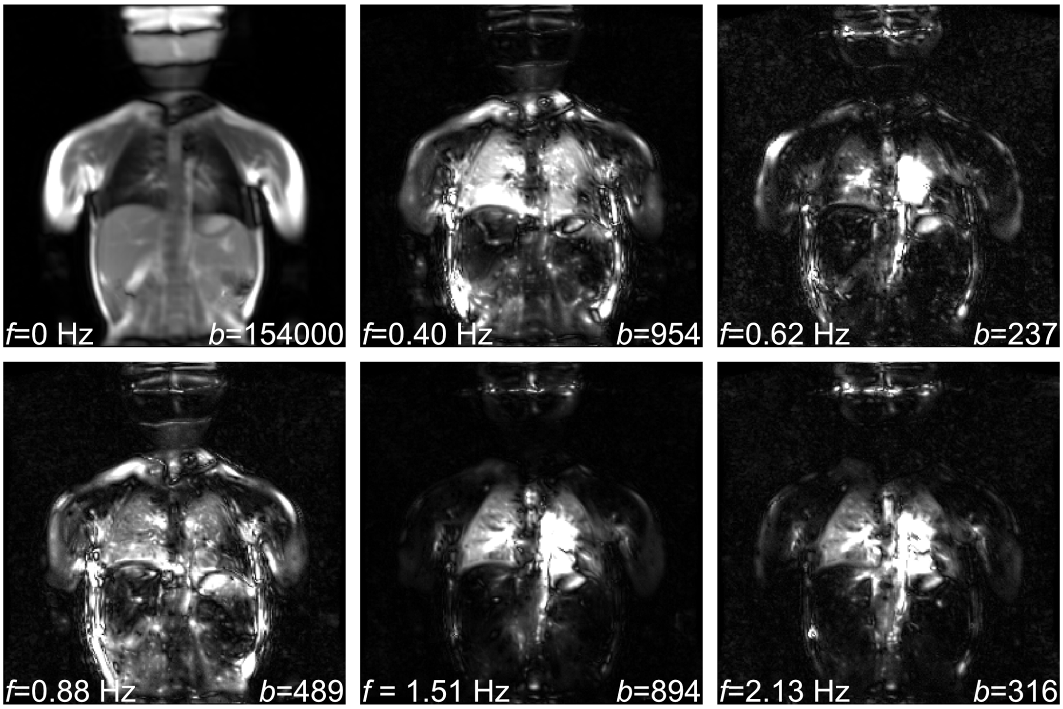

FIGURE 5.3: Exemplary dominant modes obtained with the DMD analysis from measurements of a patient with left-sided herniation and ECMO treatment. Here, the dynamic images are obtained with Protocol A, and non-rigid registration is completed before the DMD analysis. The mode frequencies (f) and mode amplitudes (b) associated with the individual modes are also displayed overlaid on the modes. The DMD analysis identifies coherent spatiotemporal structures in the dynamic acquisitions, such as signal variations caused by respiration and pulsation, as well as secondary motions or harmonics. For this patient, modes related to pulmonary ventilation (mode with $f = 0.40$ Hz) and perfusion (mode with $f = 1.51$ Hz) were selected and used for the calculation of fractional ventilation and normalized perfusion maps.

PBF_{Ratio} for both protocols. Bland-Altman plots demonstrate a close agreement between Q_{Ratio} and PBF_{Ratio}, with reproducibility coefficient (RPC) $RPC = 0.22$ for Protocol A, and $RPC = 0.20$ for Protocol B, and without a significant bias or systematic difference for both protocols.

5.4 Discussion

Currently, pediatric lung MRI studies mainly focus on structural abnormalities, and only a limited number of studies have investigated pulmonary functions (Dyke et al., 2023; Weis et al., 2016a). A crucial constraint is that pediatric patients typically exhibit faster cardiac and respiratory rates (Fleming et al., 2011), necessitating faster pulse sequences. Moreover, a reduced FOV is required for imaging pediatric patients, which limits the minimum achievable echo time (Ljimani et al., 2021), and thereby reduces the attainable SNR. Nevertheless, our results indicate that pulmonary functional imaging of 2-year-old CDH patients can be achieved at 1.5T field strength using bSSFP protocols.

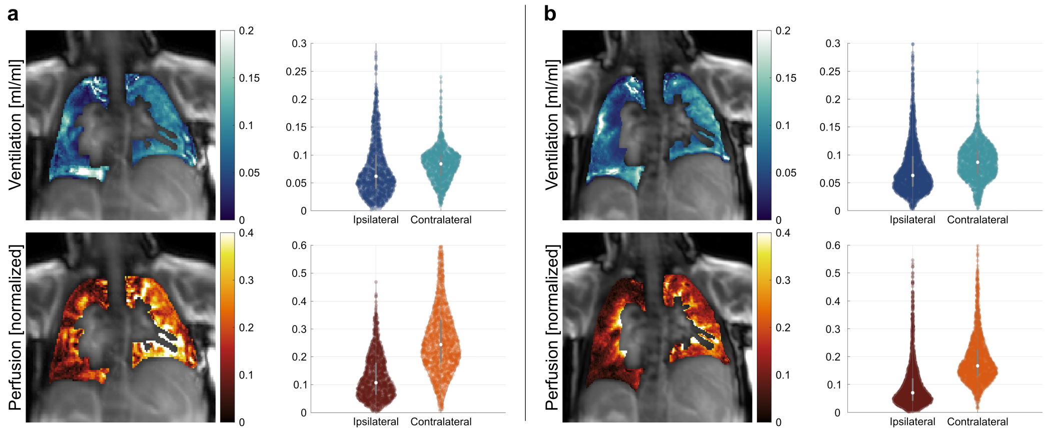

FIGURE 5.4: Exemplary fractional ventilation and normalized perfusion maps obtained through DMD MRI of a patient with right-sided herniation and without ECMO therapy obtained with (**a**) Protocol A, and (**b**) Protocol B. The maps are cropped to the region of interest for visualization purposes. Next to the maps, violin plots depict the distribution of functional values of each lung. For both protocols, differences between ipsilateral and contralateral lungs are discernible in both ventilation and perfusion maps, as well as the accompanying violin plots, which imply impaired lung function in the ipsilateral lung relative to the contralateral lung.

A key advantage of DMD MRI is its ability to generate both ventilation and perfusion maps from the same acquisition without any radiation burden or administration of intravenous contrast agents (Weidner et al., 2014; Sanchez-Crespo, 2019). Consequently, unlike SPECT or DCE MRI, DMD MRI can be repeated in cases where images are rendered non-diagnostic due to patient motion or technical difficulties (Edelman and Koktzoglou, 2019). Furthermore, it allows more frequent imaging in patients needing special care and can enable the safer investigation of longitudinal trends of pulmonary ventilation and perfusion (Dao et al., 2020). Thus, it may improve our understanding of disease progression.

Our results indicate that both bSSFP protocols can acquire temporal features with success, and the trade-offs associated with Protocol B do not compromise the functional image quality. A possible explanation for the poorer CNR performance of Protocol A, despite its better SNR performance, is the partial volume effects, which may result in the blurring of features. Nevertheless, we propose the use of Protocol B due to its higher in-plane resolution in future studies.

Our results indicate that the V_{Ratio} values are higher than other ratios calculated between ipsilateral and contralateral lungs. A possible explanation for this could be the sensitivity of bSSFP pulse sequences to magnetic field inhomogeneities. Recently, it was shown that functional maps obtained via conventional bSSFP acquisitions suffer from banding artefacts, resulting in inhomogeneous ventilation maps (Ilicak et al., 2022b). To overcome this, more advanced techniques can be utilized during acquisitions (Ilicak et al., 2022b; Bauman, Pusterla, and Bieri, 2016). Nevertheless, our results indicate that the ventilation differences between the ipsilateral and contralateral lungs are still significant. Additionally, ventilation of ipsilateral lung seems to be less affected after CDH than perfusion, underlying the hypothesis that lung vessels are affected by CDH associated lung hypoplasia.

Here, we were not able to compare the DMD MRI-based V_{Ratio} and Q_{Ratio} values

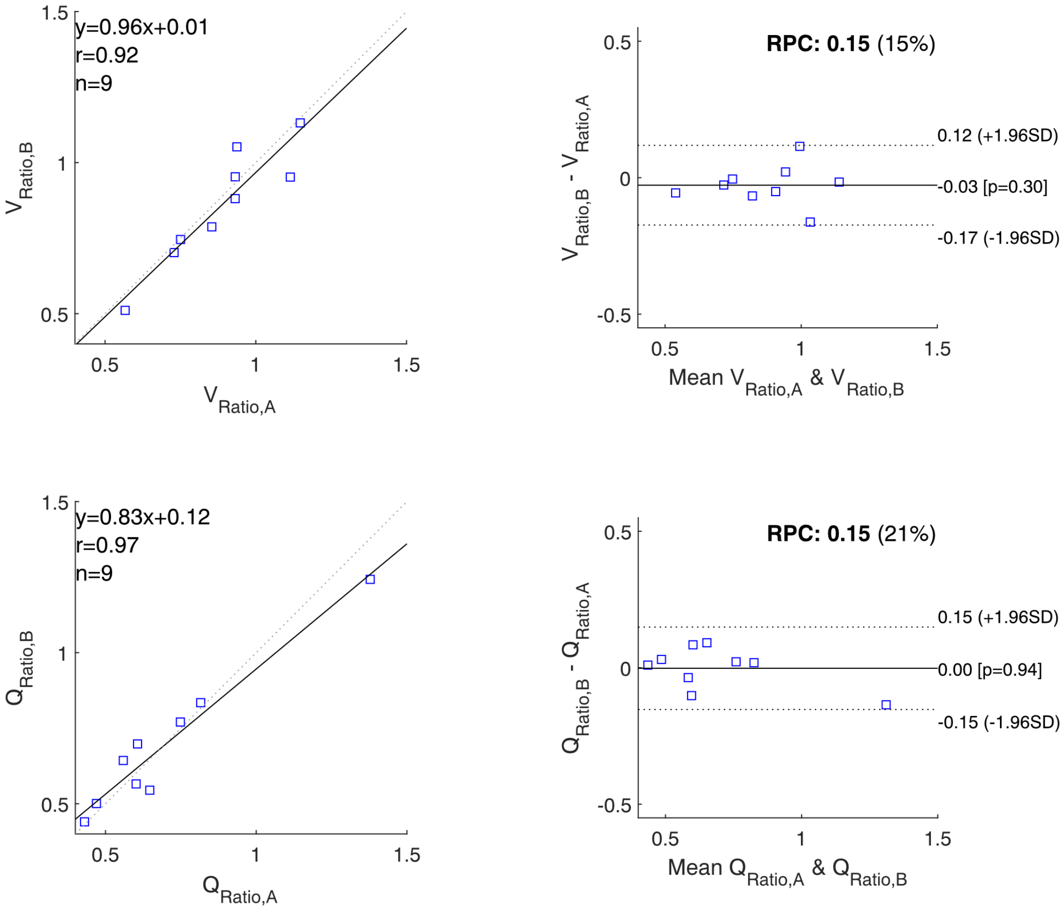

FIGURE 5.5: Pearsons correlation and Bland-Altman analyses of functional ratios obtained through DMD MRI with Protocol A and Protocol B. V_{Ratio} and Q_{Ratio} values obtained with two non-contrast-enhanced bSSFP protocols display a very strong correlation and a close agreement with each other without any systematic differences.

with a healthy cohort, and the contralateral lungs were assumed to be relatively normal (Björkman et al., 2011). Previous studies with CDH patients have reported similar results when comparing ipsilateral lung to the contralateral lung using scintigraphy (Stefanutti et al., 2004; Muratore et al., 2001), SPECT (Björkman et al., 2011; Sanchez-Crespo, 2019), and DCE MRI (Weidner et al., 2014; Weis et al., 2016b; Groß et al., 2021). The V_{Ratio} and Q_{Ratio} results reported in this study are in line with those observations. Additionally, when compared with the DCE method, we have observed a very strong agreement between Q_{Ratio} and PBF_{Ratio} values obtained from the same patients.

In the current study, the bSSFP acquisitions were limited to a single slice position due to scan time constraints. In future work, multiple slice locations could be acquired using a single protocol to increase lung volume coverage. Additionally, thinner slices may be required to offset the partial volume effects at the expense of SNR. To this end, recent developments incorporating low-rank priors during image reconstruction (Ilicak, Saritas, and Çukur, 2022) showed promising results in functional lung imaging (Ilicak et al., 2022a). Another limitation of the study arises from the inherent issues associated with the quantification methods (Ilicak et al., 2022b);

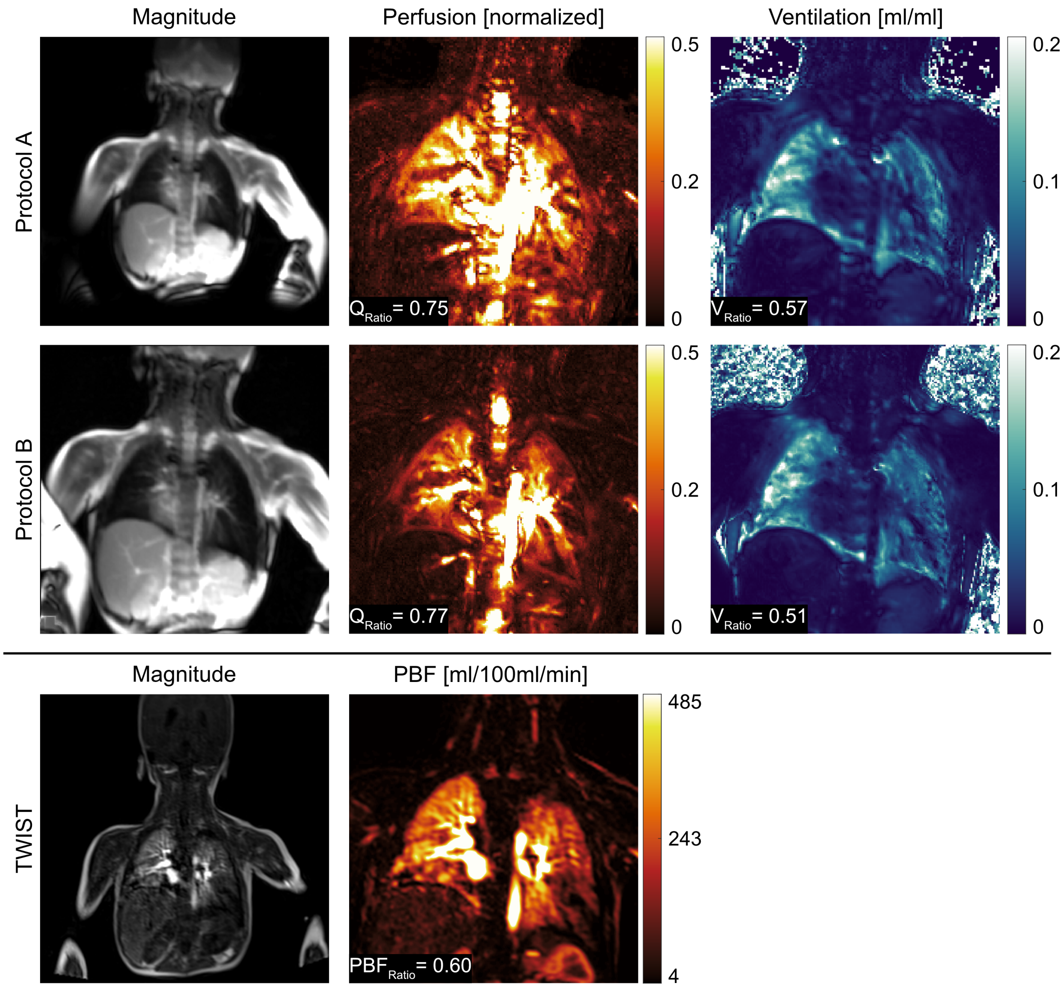
Magnitude
Perfusion [normalized]
Ventilation [ml/ml]
Protocol A
Protocol B
TWIST
0.5
0.2
0
0.2
0.1
0
Q_{Ratio} = 0.75
V_{Ratio} = 0.57
Q_{Ratio} = 0.77
V_{Ratio} = 0.51
Magnitude
PBF [ml/100ml/min]
485
243
4
PBF_{Ratio} = 0.60

FIGURE 5.6: Representative magnitude images from bSSFP protocols, along with normalized perfusion, and fractional ventilation maps obtained through DMD MRI from a patient with left sided hernia and ECMO therapy. Additionally, a representative magnitude image and PBF map obtained from TWIST protocol for the same patient from a similar slice location are displayed. For visualization purposes, all functional maps are cropped to the region of interest. Overall, reductions in the ipsilateral lung can be observed visually, and can be confirmed by the resulting quantitative ratios (displayed overlaid on functional maps). Although the TWIST-based method can generate quantitative PBF maps, DMD MRI does not require the administration of contrast agents and is also capable of generating ventilation maps.

consequently, V/Q maps were not calculated. While improved quantification methods are warranted, DMD MRI can become a useful tool for analysing V/Q mismatch associated with CDH (Hayward et al., 2007; Okuyama et al., 2006; Dao et al., 2020; Dassios et al., 2022).

In summary, we have successfully demonstrated the ability to measure pulmonary functional information in 2-year-old CDH patients. Our approach involved analysing free-breathing dynamic bSSFP acquisitions through DMD to obtain ventilation and perfusion maps, without the need for ionizing radiation or exposure to contrast

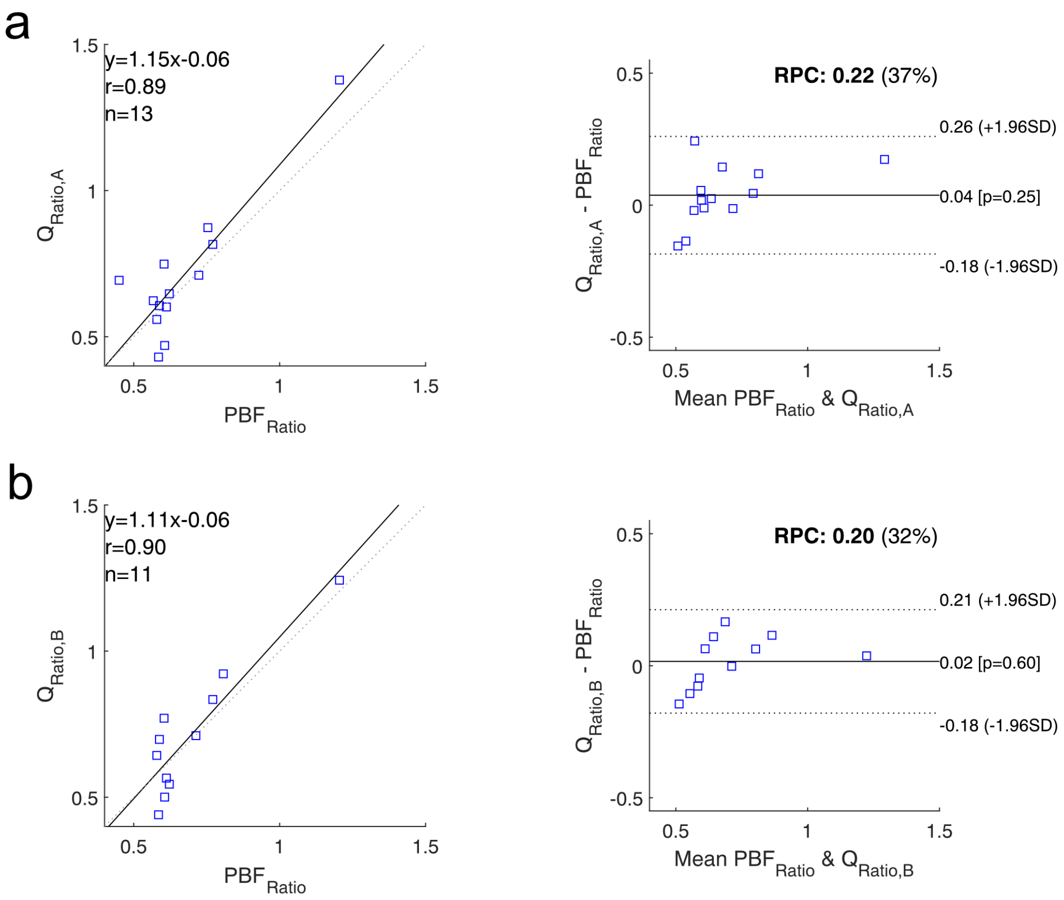

FIGURE 5.7: Pearsons correlation and Bland-Altman analyses between perfusion ratios obtained via TWIST (PBF_{Ratio}) and DMD MRI (Q_{Ratio}) for (**a**) Protocol A and (**b**) Protocol B. For both protocols, we observe a very strong correlation without any significant bias or systematic difference. (r, Pearsons correlation coefficient; RPC, reproducibility coefficient.)

agents. Our results are in line with previously reported values obtained with different modalities. Moreover, DMD-based perfusion results reported here demonstrate a very strong agreement with the perfusion results obtained through the TWIST method. Overall, DMD MRI is a promising tool for the analysis of pulmonary function in pediatric CDH patients and may be used for longitudinal assessments of pulmonary functional changes.

Chapter 6

Summary

The measurement of pulmonary ventilation and perfusion without the use of contrast agents is highly valuable for the diagnosis and monitoring of prevalent lung diseases. To this end, non-contrast-enhanced MRI is an emerging alternative to scintigraphical measurements, computed tomography, and contrast-enhanced MRI. Although non-contrast-enhanced MRI methods enable the acquisition of both structural and functional information in the same scan session, they suffer from robustness issues associated with imaging artifacts and post-processing techniques. As such, there has been limited clinical utilization of these methods.

The aim of this thesis was to improve the robustness of non-contrast-enhanced functional lung imaging and to showcase its capabilities in the assessment of in 2-year old congenital diaphragmatic hernia patients after patch repair. In Chapter 3, a robust alternative acquisition framework for non-contrast-enhanced functional lung imaging was presented. In Chapter 4, a new analysis method was presented for improved accuracy in the estimation of pulmonary ventilation and perfusion related signal changes. In Chapter 5, the analysis method developed in Chapter 4 was demonstrated for obtaining pulmonary functional information in 2-year-old CDH patients after patch repair.

In the following paragraphs, a comprehensive overview of each study is presented in detail.

Phase–cycled balanced SSFP imaging for non-contrast-enhanced functional lung imaging,
Magnetic Resonance in Medicine, doi:10.1002/mrm.29302.

In Chapter 3, a multiple-acquisition bSSFP acquisition framework based on RF phase cycling was developed as an alternative in Fourier decomposition MRI for improved robustness against field inhomogeneities. Here, 2D dynamic lung images were obtained from 5 healthy volunteers at 1.5T and 3T field strengths using a bSSFP pulse sequence with $N = 4$ different RF phase increments. These images were then compared to those obtained using conventional bSSFP acquisitions with a single RF phase increment. For a fair comparison, both acquisitions were divided into four subgroups, and subgroups were post-processed identically.

At both field strengths, functional maps obtained from individual subgroups displayed local signal losses as well as inhomogeneities across the lung parenchyma. Nevertheless, when the subgroups were combined, we observed more homogeneous functional maps and improved robustness against signal voids for phase-cycled acquisitions. To quantitatively assess functional map homogeneity, coefficient of variation (CV) analysis was performed. The CV values of combined ventilation maps resulted in 29.7 ± 2.6 at 1.5T and 37.5 ± 3.1 at 3T for phase-cycled acquisitions, compared with 39.9 ± 5.2 at 1.5T and 49.5 ± 3.7 at 3T for conventional acquisitions. The CV values of combined perfusion maps resulted in 55.3 ± 4.9 at 1.5T and 84.5 ± 6.7 at

3T for phase-cycled acquisitions, compared with 54.0 ± 5.2 at 1.5T and 95.8 ± 15.3 at 3T for conventional acquisitions. Overall, our results indicate that phase-cycled acquisitions improve robustness against field inhomogeneity artifacts and significantly improve ($p < 0.05$) ventilation map homogeneity.

Dynamic mode decomposition of dynamic MRI for assessment of pulmonary ventilation and perfusion,
Magnetic Resonance in Medicine, doi:10.1002/mrm.29656.

In Chapter 4, a new technique based on dynamic mode decomposition (DMD) is proposed to robustly identify dominant spatiotemporal features latent within the dynamic images. To this end, pulmonary fractional ventilation and normalized perfusion maps were obtained from digital lung phantoms as well as dynamic acquisitions of 5 healthy volunteers. The performance of the DMD method was compared with conventional Fourier decomposition (FD) and matrix pencil (MP) methods. Mean functional map values within the lung parenchyma were calculated across varying number of measurements to assess the methods' accuracy.

The mean ventilation and perfusion amplitudes estimated from simulated phantom measurements displayed that DMD significantly reduced variations in estimated amplitude in ventilation maps ($p < 0.05$), and significantly reduced variations in perfusion maps after the shift in cardiac frequency ($p < 0.05$). Similarly, results obtained from the in vivo measurements demonstrated that DMD noticeably improved ventilation and perfusion estimation, and mitigated amplitude inconsistencies across different number of measurements. In particular, DMD was shown to display significantly lower dispersion in both ventilation and perfusion map amplitudes when compared with MP ($p < 0.05$). In conclusion, the DMD method is demonstrated to be a viable option for robust spectral analysis in dynamic MR acquisitions.

Functional lung imaging of 2-year-old children after congenital diaphragmatic hernia repair using dynamic mode decomposition,
Submitted to European Radiology on 19.04.2023.

In Chapter 5, we demonstrated that pulmonary ventilation and perfusion information can be obtained in 2-year-old patients after CDH repair, without the need for ionizing radiation or contrast agents. This was achieved by utilizing free-breathing non-contrast-enhanced MRI acquisitions together with DMD analysis to obtain pulmonary functional maps. Moreover, two different bSSFP protocols were prescribed, and ventilation and perfusion ratios of ipsilateral to contralateral lungs were obtained to evaluate functional differences between the lungs. The functional ratio results were then compared using Pearson's correlation and Bland-Altman analyses. These analyses were done between bSSFP protocols, and between DMD-based perfusion ratios and perfusion parameters obtained using contrast-enhanced MRI.

The ipsilateral to contralateral ventilation and perfusion ratios were 0.84 ± 0.19 and 0.70 ± 0.24 for Protocol A, and 0.88 ± 0.18 and 0.72 ± 0.23 for Protocol B, indicating reduced functional results on the ipsilateral side. Furthermore, a close agreement between two bSSFP protocols was observed without a significant bias or systematic difference with $r = 0.92$ for ventilation ratios, and $r = 0.97$ for perfusion ratios. More importantly, a very strong positive correlation and close agreement between DMD MRI-based perfusion values and DCE MRI-based perfusion parameters were observed for both protocols with $r = 0.89$ for Protocol A, and $r = 0.90$ for Protocol B. Overall, DMD MRI holds great promise as a tool for analyzing pulmonary function in pediatric patients and has the potential to be used for longitudinal assessments of pulmonary functional changes.

Chapter 7

Outlook

A major limitation for non-contrast-enhanced functional lung imaging stems from the inherent problems associated with the quantification techniques. In the work of (Zapke et al., 2006), ventilation information is extracted via the signal differences between expiration and inspiration. However, this model excludes the tissue relaxation differences between expiration and inspiration (Stadler et al., 2005). Moreover, the ventilation quantification methods developed by (Kjørstad et al., 2014b) and (Bauman and Bieri, 2017) utilize the zero frequency component together with the signal differences to obtain fractional ventilation maps. However, both of these methods neglect the effects of image contrast in the zero frequency image. Similarly, the quantitative lung perfusion method developed in (Kjørstad et al., 2014a) uses a modified version of the model developed in (Buxton et al., 1998) for arterial spin labeling (ASL). Nevertheless, the original model includes a correction factor "q", that accounts for the differences of blood and tissue relaxation times. While this factor can be assumed as $q = 1$ in ASL methods (Buxton et al., 1998; Fischer et al., 2008), this might not be correct for other acquisition techniques. As such, the underlying image contrast would affect the quantified perfusion results. Consequently, these ventilation and perfusion quantification methods not only display a dependence on field strength, but also on acquisition parameters such as the prescribed pulse sequence (e.g., bSSFP, GRE, etc.) or pulse sequence parameters (e.g., flip angle, TE, TR, etc.). Therefore, further studies are needed to develop quantification methods that take image contrast and tissue relaxation into account.

In Chapter 3, an RF phase cycling strategy was demonstrated to increase the robustness against field inhomogeneity artifacts and to improve the functional map homogeneity. While this method was evaluated using acquisitions from healthy volunteers, its application in the imaging of patients with pulmonary diseases remains an open problem. Furthermore, the phase cycling scheme with four equispaced phase increments might be suboptimal for lung imaging. Subsequently, acquisitions with additional phase increments and their combinations should be investigated to improve the image quality.

The post-processing method introduced in Chapter 4 was demonstrated to perform more reliably compared to conventional methods such as Fourier decomposition and matrix pencil decomposition methods. Nevertheless, DMD algorithm is known to have limitations in characterizing transient time phenomena (Schmid et al., 2011), such as sharp breath-holding maneuvers. To overcome this limitation, a multiresolution DMD algorithm was recently proposed (Kutz, Fu, and Brunton, 2016). Here, the dynamic system is iteratively decomposed using shorter measurement windows, and the DMD modes are extracted from slow to increasingly fast time scales. This recursive sampling structure enables a better analysis of high frequency features; therefore, it might enable a better representation of transient state behavior. Another limitation of the DMD arises from its sensitivity to rank deficiencies (Tu et al., 2014). While the method described in Chapter 4 incorporated data stacking to mitigate rank deficiency limitations, more advanced methods such as forward/backward DMD can be implemented to further improve the performance of DMD MRI (Dawson et al., 2016). In forward/backward DMD, the measurement matrices X and X' are swapped to compute the an additional DMD on data pair (X', X), meaning that a mapping operator A^b is estimated for the backward dynamic system. By using a combination of the forward and backward mapping operators, the robustness against rank deficiencies, and noise resilience of DMD algorithm can be increased; and accordingly, the accuracy of eigenvalue estimation can be further improved.

Lastly, in previous conference abstracts (Ilicak et al., 2019b; Ilicak et al., 2020), we have displayed that the dynamic lung acquisitions can benefit from sparse reconstruction techniques. Specifically, in (Ilicak et al., 2019b) it was shown that compressibility of lung images can be exploited through compressed sensing reconstructions, allowing for higher undersampling ratios during acquisition. Consequently, temporal resolution of free-breathing non-contrast-enhanced acquisitions can be improved without compromising image quality. Thereafter, in (Ilicak et al., 2020), low-rank and locally low-rank reconstruction techniques were demonstrated to further improve the image quality in compressed sensing reconstructions by incorporating spatial sparsity terms in addition to temporal sparsity terms. While both of these studies were done retrospectively on dynamic acquisitions obtained from healthy volunteers, more detailed analyses are warranted to explore the limitations of compressed sensing reconstructions. In particular, the regularization parameter selection during the reconstructions, and the optimization of k-space sampling trajectories in functional lung imaging remains open problems. To this end, stochastic greedy algorithms (Sanchez et al., 2020) or deep learning frameworks (Bahadir et al., 2020) could be employed for sampling pattern optimization, and automated parameter selection strategies might be deployed for regularization parameter selection (Shahdloo et al., 2019; Ilicak, Saritas, and Çukur, 2022).

Bibliography

Abolmaali, Nasreddin et al. (2010). Lung volumes, ventricular function and pulmonary arterial flow in children operated on for left-sided congenital diaphragmatic hernia: Long-term results. *European Radiology* 20.7, pp. 1580–1589. ISSN: 09387994. DOI: 10.1007/s00330-010-1723-9.

Alassaf, Abdullah and Lingling Fan (2021). Randomized Dynamic Mode Decomposition for Oscillation Modal Analysis. *IEEE Transactions on Power Systems* 36.2, pp. 1399–1408. ISSN: 0885-8950. DOI: 10.1109/TPWRS.2020.3012419.

Albert, M. S. et al. (1994). Biological magnetic resonance imaging using laser-polarized 129Xe. *Nature* 370.6486, pp. 199–201. ISSN: 0028-0836. DOI: 10.1038/370199a0.

Ansari, A. R. and R. A. Bradley (1960). Rank-Sum Tests for Dispersions. *The Annals of Mathematical Statistics* 31.4, pp. 1174–1189. ISSN: 0003-4851. DOI: 10.1214/aoms/1177705688.

Atiyah, Yahya, Wachowicz Keith, and B. Gino Fallone (2010). Feasibility of Using Linear Combination SSFP for Lung MRI at 3 T. *Proc. Intl. Soc. Mag. Reson. Med. 18*, p. 2511.

Attenberger, Ulrike I. et al. (2009). Time-resolved 3D pulmonary perfusion MRI: comparison of different k-space acquisition strategies at 1.5 and 3 T. *Investigative radiology* 44.9, pp. 525–531. ISSN: 15360210.

Bachert, Peter et al. (1996). Nuclear magnetic resonance imaging of airways in humans with use of hyperpolarized 3He. *Magnetic Resonance in Medicine* 36.2, pp. 192–196. ISSN: 07403194. DOI: 10.1002/mrm.1910360204.

Bahadir, Cagla D et al. (2020). Deep-Learning-Based Optimization of the Under-Sampling Pattern in MRI. *IEEE Transactions on Computational Imaging* 6, pp. 1139–1152. ISSN: 23339403. DOI: 10.1109/TCI.2020.3006727. arXiv: 1907.11374.

Bai, Zhe et al. (2020). Dynamic Mode Decomposition for Compressive System Identification. *AIAA Journal* 58.2, pp. 561–574. ISSN: 0001-1452. DOI: 10.2514/1.J057870. arXiv: 1710.07737.

Balasch, Anke et al. (2020). 2D Ultrashort Echo-Time Functional Lung Imaging. *Journal of Magnetic Resonance Imaging* 52.6, pp. 1637–1644. ISSN: 1053-1807. DOI: 10.1002/jmri.27269.

Bangerter, Neal K et al. (2004). Analysis of multiple-acquisition SSFP. *Magnetic Resonance in Medicine* 51.5, pp. 1038–1047. ISSN: 0740-3194. DOI: 10.1002/mrm.20052.

Barrow, B. (1963). Diversity Combination of Fading Signals with Unequal Mean Strengths. *IEEE Transactions on Communications* 11.1, pp. 73–78. ISSN: 0096-2244. DOI: 10.1109/TCOM.1963.1088732.

Bauman, Grzegorz and Oliver Bieri (2017). Matrix pencil decomposition of time-resolved proton MRI for robust and improved assessment of pulmonary ventilation and perfusion. *Magnetic Resonance in Medicine* 77.1, pp. 336–342. ISSN: 0740-3194. DOI: 10.1002/mrm.26096.

Bauman, Grzegorz, Orso Pusterla, and Oliver Bieri (2016). Ultra-fast Steady-State Free Precession Pulse Sequence for Fourier Decomposition Pulmonary MRI. *Magnetic Resonance in Medicine* 75.4, pp. 1647–1653. ISSN: 07403194. DOI: `10.1002/mrm.25697`.

— (2019). Functional lung imaging with transient spoiled gradient echo. *Magnetic Resonance in Medicine* 81.3, pp. 1915–1923. ISSN: 0740-3194. DOI: `10.1002/mrm.27535`.

Bauman, Grzegorz et al. (2009). Non-contrast-enhanced perfusion and ventilation assessment of the human lung by means of fourier decomposition in proton MRI. *Magnetic Resonance in Medicine* 62.3, pp. 656–664. ISSN: 07403194. DOI: `10.1002/mrm.22031`.

Bauman, Grzegorz et al. (2013). Validation of Fourier decomposition MRI with dynamic contrast-enhanced MRI using visual and automated scoring of pulmonary perfusion in young cystic fibrosis patients. *European Journal of Radiology* 82.12, pp. 2371–2377. ISSN: 0720048X. DOI: `10.1016/j.ejrad.2013.08.018`.

Bauman, Grzegorz et al. (2017). Pulmonary relaxometry with inversion recovery ultra-fast steady-state free precession at 1.5T. *Magnetic Resonance in Medicine* 77.1, pp. 74–82. ISSN: 15222594. DOI: `10.1002/mrm.26490`.

Behrendt, Lea et al. (2020). Validation of Automated Perfusion-Weighted Phase-Resolved Functional Lung (PREFUL)-MRI in Patients With Pulmonary Diseases. *Journal of Magnetic Resonance Imaging* 52.1, pp. 103–114. ISSN: 1053-1807. DOI: `10.1002/jmri.27027`.

Benkert, Thomas et al. (2015). Dynamically phase-cycled radial balanced SSFP imaging for efficient banding removal. *Magnetic Resonance in Medicine* 73.1, pp. 182–194. ISSN: 07403194. DOI: `10.1002/mrm.25113`.

Bergin, C. J., J. M. Pauly, and A. Macovski (1991). Lung parenchyma: Projection reconstruction MR imaging. *Radiology* 179.3, pp. 777–781. ISSN: 00338419. DOI: `10.1148/radiology.179.3.2027991`.

Bernstein, Matt A., Kevin F. King, and Xiaohong J. Zhou, eds. (2004). Burlington: Academic Press, pp. 960–962. ISBN: 978-0-12-092861-3. DOI: `https://doi.org/10.1016/B978-012092861-3/50026-1`.

Biederer, J. et al. (2012a). MRI of the lung (2/3). Why … when … how? *Insights into Imaging* 3.4, pp. 355–371. ISSN: 1869-4101. DOI: `10.1007/s13244-011-0146-8`.

Biederer, Juergen (2018). General Requirements of MRI of the Lung and Suggested Standard Protocol. *MRI of the Lung*. Ed. by Hans-Ulrich Kauczor and Mark Oliver Wielpütz. Cham: Springer International Publishing, pp. 1–20. ISBN: 978-3-319-42617-4. DOI: `10.1007/174_2017_98`.

Biederer, Jürgen et al. (2012b). MRI of the lung (3/3)current applications and future perspectives. *Insights into Imaging* 3.4, pp. 373–386. ISSN: 1869-4101. DOI: `10.1007/s13244-011-0142-z`.

Bieri, Oliver (2013). Ultra-fast steady state free precession and its application to in vivo 1 H morphological and functional lung imaging at 1.5 tesla. *Magnetic Resonance in Medicine* 70.3, pp. 657–663. ISSN: 07403194. DOI: `10.1002/mrm.24858`.

Bieri, Oliver and Klaus Scheffler (2013). Fundamentals of balanced steady state free precession MRI. *Journal of Magnetic Resonance Imaging* 38.1, pp. 2–11. DOI: `10.1002/jmri.24163`.

Biyik, Erdem, Efe Ilicak, and Tolga Çukur (2018). Reconstruction by calibration over tensors for multi-coil multi-acquisition balanced SSFP imaging. *Magnetic Resonance in Medicine* 79.5, pp. 2542–2554. ISSN: 0740-3194. DOI: `10.1002/mrm.26902`. arXiv: `1704.00096`.

Björkman, Karin C. et al. (2011). Postoperative regional distribution of pulmonary ventilation and perfusion in infants with congenital diaphragmatic hernia. *Journal of Pediatric Surgery* 46.11, pp. 2047–2053. ISSN: 00223468. DOI: 10.1016/j.jpedsurg.2011.06.042.

Bondesson, David et al. (2019). Nonuniform Fourier-decomposition MRI for ventilation- and perfusion-weighted imaging of the lung. *Magnetic Resonance in Medicine* 82.4, pp. 1312–1321. ISSN: 0740-3194. DOI: 10.1002/mrm.27803.

Brown, Robert W. et al. (2014). *Magnetic Resonance Imaging: Physical Principles and Sequence Design, Second Edition*. Chichester, UK: John Wiley & Sons, Ltd. ISBN: 9781118633953. DOI: 10.1002/9781118633953.

Buxton, Richard B. et al. (1998). A general kinetic model for quantitative perfusion imaging with arterial spin labeling. *Magnetic Resonance in Medicine* 40.3, pp. 383–396. ISSN: 07403194. DOI: 10.1002/mrm.1910400308.

Campbell-Washburn, Adrienne E. et al. (2019). Opportunities in interventional and diagnostic imaging by using high-performance low-field-strength MRI. *Radiology* 293.2, pp. 384–393. ISSN: 15271315. DOI: 10.1148/radiol.2019190452.

Capaldi, Dante P.I. et al. (2015). Free-breathing Pulmonary 1H and Hyperpolarized 3He MRI. *Academic Radiology* 22.3, pp. 320–329. ISSN: 10766332. DOI: 10.1016/j.acra.2014.10.003.

Carr, H. Y. (1958). Steady-State Free Precession in Nuclear Magnetic Resonance. *Physical Review* 112.5, pp. 1693–1701. ISSN: 0031-899X. DOI: 10.1103/PhysRev.112.1693.

Chang, Kevin J. et al. (2008). 3.0-T MR imaging of the Abdomen: Comparison with 1.5 T. *Radiographics* 28.7, pp. 1983–1998. DOI: 10.1148/rg.287075154.

Chassagnon, Guillaume et al. (2019). High-resolution lung MRI with Ultrashort-TE: 1.5 or 3 Tesla? *Magnetic Resonance Imaging* 61.April, pp. 97–103. ISSN: 18735894. DOI: 10.1016/j.mri.2019.04.015.

Chefd'Hotel, C., G. Hermosillo, and O. Faugeras (2001). A variational approach to multi-modal image matching. *Proceedings IEEE Workshop on Variational and Level Set Methods in Computer Vision*. IEEE Computer Soc, pp. 21–28. ISBN: 0-7695-1278-X. DOI: 10.1109/VLSM.2001.938877.

Chefd'hotel, C., G. Hermosillo, and O. Faugeras (2002). Flows of diffeomorphisms for multimodal image registration. *Proceedings IEEE International Symposium on Biomedical Imaging*. IEEE, pp. 753–756. ISBN: 0-7803-7584-X. DOI: 10.1109/ISBI.2002.1029367.

Cloutier, Michelle M. (2019). *Respiratory Physiology*. 2nd. Elsevier. ISBN: 978-0-323-59579-7.

Corteville, D. M. R. et al. (2015). Fourier decomposition pulmonary MRI using a variable flip angle balanced steady-state free precession technique. *Magnetic Resonance in Medicine* 73.5, pp. 1999–2004. ISSN: 07403194. DOI: 10.1002/mrm.25293.

Couch, Marcus J. et al. (2021). Comparison of Functional Free-Breathing Pulmonary 1H and Hyperpolarized 129Xe Magnetic Resonance Imaging in Pediatric Cystic Fibrosis. *Academic Radiology* 28.8, e209–e218. ISSN: 18784046. DOI: 10.1016/j.acra.2020.05.008.

Crémillieux, Yannick et al. (2019). Three-dimensional quantitative MRI of aerosolized gadolinium-based nanoparticles and contrast agents in isolated ventilated porcine lungs. *Magnetic Resonance in Medicine* July, pp. 1–9. ISSN: 15222594. DOI: 10.1002/mrm.28041.

Cukur, Tolga (2015). Accelerated Phase-Cycled SSFP Imaging With Compressed Sensing. *IEEE Transactions on Medical Imaging* 34.1, pp. 107–115. ISSN: 0278-0062. DOI: 10.1109/TMI.2014.2346814.

Çukur, Tolga (2016). Spectrally selective imaging with wideband balanced steady-state free precession MRI. *Magnetic Resonance in Medicine* 75.3, pp. 1132–1141. ISSN: 0740-3194. DOI: `10.1002/mrm.25700`.

Çukur, Tolga, Michael Lustig, and Dwight G. Nishimura (2008). Multiple-profile homogeneous image combination: Application to phase-cycled SSFP and multicoil imaging. *Magnetic Resonance in Medicine* 60.3, pp. 732–738. ISSN: 07403194. DOI: `10.1002/mrm.21720`.

Dao, Duy T. et al. (2020). Longitudinal Analysis of Ventilation Perfusion Mismatch in Congenital Diaphragmatic Hernia Survivors. *Journal of Pediatrics* 219, 160–166.e2. ISSN: 10976833. DOI: `10.1016/j.jpeds.2019.09.053`.

Dassios, Theodore et al. (2022). Ventilation-to-perfusion relationships and right-to-left shunt during neonatal intensive care in infants with congenital diaphragmatic hernia. *Pediatric Research* 92.6, pp. 1657–1662. ISSN: 15300447. DOI: `10.1038/s41390-022-02001-2`.

Dawson, Scott T. M. et al. (2016). Characterizing and correcting for the effect of sensor noise in the dynamic mode decomposition. *Experiments in Fluids* 57.3, p. 42. ISSN: 0723-4864. DOI: `10.1007/s00348-016-2127-7`. arXiv: `1507.02264`.

Deimling, M et al. (2008). Time Resolved Lung Ventilation Imaging by Fourier Decomposition. *Proceedings 16th Scientific Meeting, International Society for Magnetic Resonance in Medicine* Toronto.c, p. 2639.

Delacoste, Jean et al. (2019). Ultrashort echo time imaging of the lungs under high-frequency noninvasive ventilation: A new approach to lung imaging. *Journal of Magnetic Resonance Imaging* 50.6, pp. 1789–1797. ISSN: 1053-1807. DOI: `10.1002/jmri.26808`.

Deppe, Martin H. et al. (2009). Susceptibility effects in hyperpolarized 3 He lung MRI at 1.5T and 3T. *Journal of Magnetic Resonance Imaging* 30.2, pp. 418–423. ISSN: 10531807. DOI: `10.1002/jmri.21852`.

Dirk-Jan Kroon (2021). *Region Growing*. Tech. rep.

Dyke, J P et al. (2023). Assessment of lung ventilation of premature infants with bronchopulmonary dysplasia at 1.5 Tesla using phase-resolved functional lung magnetic resonance imaging. *Pediatric Radiology* 0123456789. ISSN: 1432-1998. DOI: `10.1007/s00247-023-05598-6`.

Ebert, M et al. (1996). Nuclear magnetic resonance imaging with hyperpolarised helium-3. *The Lancet* 347.9011, pp. 1297–1299. ISSN: 01406736. DOI: `10.1016/S0140-6736(96)90940-X`.

Ebner, Lukas et al. (2017). The role of hyperpolarized 129xenon in MR imaging of pulmonary function. *European Journal of Radiology* 86, pp. 343–352. ISSN: 0720048X. DOI: `10.1016/j.ejrad.2016.09.015`.

Edelman, Robert R. and Ioannis Koktzoglou (2019). Noncontrast MR angiography: An update. *Journal of Magnetic Resonance Imaging* 49.2, pp. 355–373. ISSN: 10531807. DOI: `10.1002/jmri.26288`.

Elliott, Andrew M. et al. (2007). Nonlinear averaging reconstruction method for phase-cycle SSFP. *Magnetic Resonance Imaging* 25.3, pp. 359–364. ISSN: 0730-725X. DOI: `10.1016/j.mri.2006.09.013`.

Ertürk, M. Arcan et al. (2017). Toward imaging the body at 10.5 tesla. *Magnetic Resonance in Medicine* 77.1, pp. 434–443. ISSN: 15222594. DOI: `10.1002/mrm.26487`.

Feng, Li et al. (2018). Simultaneous Evaluation of Lung Anatomy and Ventilation Using 4D Respiratory-Motion-Resolved Ultrashort Echo Time Sparse MRI. *Journal of Magnetic Resonance Imaging*. ISSN: 10531807. DOI: `10.1002/jmri.26245`.

Fink, Christian et al. (2007). Lung MRI at 1.5 and 3 Tesla. *Investigative Radiology* 42.6, pp. 377–383. ISSN: 0020-9996. DOI: `10.1097/01.rli.0000261926.86278.96`.

Fischer, André et al. (2008). Assessment of pulmonary perfusion in a single shot using SEEPAGE. *Journal of Magnetic Resonance Imaging* 27.1, pp. 63–70. ISSN: 10531807. DOI: `10.1002/jmri.21235`.

Fischer, André et al. (2014). SElf-gated Non-Contrast-Enhanced FUnctional Lung imaging (SENCEFUL) using a quasi-random fast low-angle shot (FLASH) sequence and proton MRI. *NMR in Biomedicine* 27.8, pp. 907–917. ISSN: 09523480. DOI: `10.1002/nbm.3134`.

Fischer, Daniel and Eva Eberlein (2013). *The New, High-Performance MR Gradient System XR 80/200. Design, Benefits and Safe Operation*.

Fleming, Susannah et al. (2011). Normal ranges of heart rate and respiratory rate in children from birth to 18 years of age: a systematic review of observational studies. *The Lancet* 377.9770, pp. 1011–1018. ISSN: 01406736. DOI: `10.1016/S0140-6736(10)62226-X`.

Glandorf, Julian et al. (2020). Comparison of phase-resolved functional lung (PREFUL) MRI derived perfusion and ventilation parameters at 1.5T and 3T in healthy volunteers. *PLOS ONE* 15.12. Ed. by Pascal A. T. Baltzer, e0244638. ISSN: 1932-6203. DOI: `10.1371/journal.pone.0244638`.

Groß, Verena et al. (2021). MR lung perfusion measurements in adolescents after congenital diaphragmatic hernia: correlation with spirometric lung function tests. *European Radiology* 0123456789. ISSN: 14321084. DOI: `10.1007/s00330-021-08315-9`.

Groun, Nourelhouda et al. (2022). Higher order dynamic mode decomposition: From fluid dynamics to heart disease analysis. *Computers in Biology and Medicine* 144.February, p. 105384. ISSN: 00104825. DOI: `10.1016/j.compbiomed.2022.105384`. arXiv: `2201.03030`.

Gulani, Vikas et al. (2017). Gadolinium deposition in the brain: summary of evidence and recommendations. *The Lancet Neurology* 16.7, pp. 564–570. ISSN: 14744422. DOI: `10.1016/S1474-4422(17)30158-8`.

Hahn, Andrew D. et al. (2020). Characterization of R2* and tissue density in the human lung: Application to neonatal imaging in the intensive care unit. *Magnetic Resonance in Medicine* 84.2, pp. 920–927. ISSN: 15222594. DOI: `10.1002/mrm.28137`.

Hargreaves, B A et al. (2001). Characterization and reduction of the transient response in steady-state MR imaging. *Magn Reson Med* 46.1, pp. 149–158.

Hatabu, Hiroto et al. (1999). MR imaging of pulmonary parenchyma with a half-Fourier single-shot turbo spin-echo (HASTE) sequence. *European Journal of Radiology* 29.2, pp. 152–159. ISSN: 0720048X. DOI: `10.1016/S0720-048X(98)00167-3`.

Hatabu, Hiroto et al. (2020). Expanding Applications of Pulmonary MRI in the Clinical Evaluation of Lung Disorders: Fleischner Society Position Paper. *Radiology* 297.2, pp. 286–301. ISSN: 0033-8419. DOI: `10.1148/radiol.2020201138`.

Hayward, Melissa J. et al. (2007). Predicting inadequate long-term lung development in children with congenital diaphragmatic hernia: an analysis of longitudinal changes in ventilation and perfusion. *Journal of Pediatric Surgery* 42.1, pp. 112–116. ISSN: 00223468. DOI: `10.1016/j.jpedsurg.2006.09.011`.

Heidenreich, Julius F et al. (2020). Three-dimensional Ultrashort Echo Time MRI for Functional Lung Imaging in Cystic Fibrosis. *Radiology* 296.1, pp. 191–199. ISSN: 0033-8419. DOI: `10.1148/radiol.2020192251`.

Higano, Nara S. et al. (2017). Quantification of neonatal lung parenchymal density via ultrashort echo time MRI with comparison to CT. *Journal of Magnetic Resonance Imaging* 46.4, pp. 992–1000. ISSN: 15222586. DOI: `10.1002/jmri.25643`.

Hilbert, Tom et al. (2018). True constructive interference in the steady state (trueCISS). *Magnetic Resonance in Medicine* 79.4, pp. 1901–1910. ISSN: 0740-3194. DOI: 10.1002/mrm.26836.

Hollinger, Laura E., Matthew T. Harting, and Kevin P. Lally (2017). Long-term follow-up of congenital diaphragmatic hernia. *Seminars in Pediatric Surgery* 26.3, pp. 178–184. ISSN: 15329453. DOI: 10.1053/j.sempedsurg.2017.04.007.

Hui, Benjamin K. et al. (2005). Navigator-gated three-dimensional MR angiography of the pulmonary arteries using steady-state free precession. *Journal of Magnetic Resonance Imaging* 21.6, pp. 831–835. ISSN: 1053-1807. DOI: 10.1002/jmri.20334.

IJsselstijn, Hanneke et al. (2018). Defining outcomes following congenital diaphragmatic hernia using standardised clinical assessment and management plan (SCAMP) methodology within the CDH EURO consortium. *Pediatric Research* 84.2, pp. 181–189. ISSN: 0031-3998. DOI: 10.1038/s41390-018-0063-3.

Ilicak, Efe, Emine Ulku Saritas, and Tolga Çukur (2022). Automated Parameter Selection for Accelerated MRI Reconstruction via Low-Rank Modeling of Local k-Space Neighborhoods. *Zeitschrift für Medizinische Physik*. ISSN: 0939-3889. DOI: https://doi.org/10.1016/j.zemedi.2022.02.002.

Ilicak, Efe et al. (2017). Profile-encoding reconstruction for multiple-acquisition balanced steady-state free precession imaging. *Magnetic Resonance in Medicine* 78.4, pp. 1316–1329. ISSN: 07403194. DOI: 10.1002/mrm.26507.

Ilicak, Efe et al. (2019a). Assessment of scan parameter effects on time resolved bSSFP acquisition for Fourier Decomposition Pulmonary MR. *Proc. Intl. Soc. Mag. Reson. Med.* 27.6, p. 4093.

Ilicak, Efe et al. (2019b). Compressed Sensing reconstruction in non-contrast-enhanced functional lung MRI using Fourier Decomposition: An initial study. *Proc. Intl. Soc. Mag. Reson. Med.* Vol. 27, p. 1897.

Ilicak, Efe et al. (2020). Low-rank and sparse matrix decomposition for accelerated non-contrast-enhanced functional lung MRI. *Proc. Intl. Soc. Mag. Reson. Med.* P. 2310.

Ilicak, Efe et al. (2021). Phase-Cycled Balanced Steady-State Free Precession Imaging for Functional Lung Imaging at 1.5 and 3 Tesla. *Proc. Intl. Soc. Mag. Reson. Med.* P. 3230.

Ilicak, Efe et al. (2022a). Improving reconstruction quality in non-contrast-enhanced functional lung imaging via LORAKS. *Proc. Intl. Soc. Mag. Reson. Med.* P. 1478.

Ilicak, Efe et al. (2022b). Phase-cycled balanced SSFP imaging for non-contrast-enhanced functional lung imaging. *Magnetic Resonance in Medicine* 88.4, pp. 1764–1774. ISSN: 0740-3194. DOI: 10.1002/mrm.29302.

Ilicak, Efe et al. (2023). Dynamic mode decomposition of dynamic MRI for assessment of pulmonary ventilation and perfusion. *Magnetic Resonance in Medicine* 90.2, pp. 761–769. DOI: https://doi.org/10.1002/mrm.29656.

Ionescu, Clara Mihaela (2013). *The Human Respiratory System*. Series in BioEngineering. London: Springer London, pp. 19–44. ISBN: 978-1-4471-5387-0. DOI: 10.1007/978-1-4471-5388-7.

IT'IS Foundation (2018). *Tissue Properties Database V4.0*. DOI: 10.13099/VIP21000-04-0.

Itoh, Harumi, Mizuki Nishino, and Hiroto Hatabu (2004). Architecture of the lung: Morphology and function. *Journal of Thoracic Imaging* 19.4, pp. 221–227. ISSN: 08835993. DOI: 10.1097/01.rti.0000142835.06988.b0.

Janos, Sara et al. (2019). Free-breathing unsedated MRI in children: Justification and techniques. *Journal of Magnetic Resonance Imaging*. ISSN: 10531807. DOI: 10.1002/jmri.26644.

Johnson, Kevin M. et al. (2013). Optimized 3D ultrashort echo time pulmonary MRI. *Magnetic Resonance in Medicine* 70.5, pp. 1241–1250. ISSN: 07403194. DOI: `10.1002/mrm.24570`.

Jovanović, Mihailo R., Peter J. Schmid, and Joseph W. Nichols (2014). Sparsity-promoting dynamic mode decomposition. *Physics of Fluids* 26.2, p. 024103. ISSN: 1070-6631. DOI: `10.1063/1.4863670`. arXiv: `1309.4165`.

Kaireit, Till F. et al. (2018). Comparison of quantitative regional ventilation-weighted fourier decomposition MRI with dynamic fluorinated gas washout MRI and lung function testing in COPD patients. *Journal of Magnetic Resonance Imaging* 47.6, pp. 1534–1541. ISSN: 10531807. DOI: `10.1002/jmri.25902`.

Kassner, Nora et al. (2018). Histogram based analysis of lung perfusion of children after congenital diaphragmatic hernia repair. *Magnetic Resonance Imaging* 48, pp. 42–49. ISSN: 0730-725X. DOI: `10.1016/J.MRI.2017.11.013`.

Kauczor, Hans Ulrich et al. (1996). Normal and abnormal pulmonary ventilation: visualization at hyperpolarized He-3 MR imaging. *Radiology* 201.2, pp. 564–568. ISSN: 0033-8419. DOI: `10.1148/radiology.201.2.8888259`.

Keijzer, Richard and Prem Puri (2010). Congenital diaphragmatic hernia. *Seminars in Pediatric Surgery* 19.3, pp. 180–185. ISSN: 10558586. DOI: `10.1053/j.sempedsurg.2010.03.001`.

Kjørstad, Åsmund et al. (2014a). Quantitative lung perfusion evaluation using fourier decomposition perfusion MRI. *Magnetic Resonance in Medicine* 72.2, pp. 558–562. ISSN: 07403194. DOI: `10.1002/mrm.24930`.

Kjørstad, Åsmund et al. (2014b). Quantitative lung ventilation using Fourier decomposition MRI; comparison and initial study. *Magnetic Resonance Materials in Physics, Biology and Medicine* 27.6, pp. 467–476. ISSN: 0968-5243. DOI: `10.1007/s10334-014-0432-9`.

Kjørstad, Åsmund et al. (2015). Non-invasive quantitative pulmonary V/Q imaging using Fourier decomposition MRI at 1.5T. *Zeitschrift für Medizinische Physik* 25.4, pp. 326–332. ISSN: 09393889. DOI: `10.1016/j.zemedi.2015.02.002`.

Klein, Jared and Megan Sirota (2017). Congenital Diaphragmatic Hernia. *New England Journal of Medicine* 377.17, e25. DOI: `10.1056/NEJMicm1701321`.

Klimeš, F. et al. (2019). Free-breathing quantification of regional ventilation derived by phase-resolved functional lung (PREFUL) MRI. *NMR in Biomedicine* December 2018, e4088. ISSN: 0952-3480. DOI: `10.1002/nbm.4088`.

Kruger, Stanley J. et al. (2016). Functional imaging of the lungs with gas agents. *Journal of Magnetic Resonance Imaging* 43.2, pp. 295–315. ISSN: 15222586. DOI: `10.1002/jmri.25002`.

Kunert-Graf, James M. et al. (2019). Extracting Reproducible Time-Resolved Resting State Networks Using Dynamic Mode Decomposition. *Frontiers in Computational Neuroscience* 13.October, pp. 1–17. ISSN: 16625188. DOI: `10.3389/fncom.2019.00075`.

Kunz, A. S. et al. (2021). Non-contrast pulmonary perfusion MRI in patients with cystic fibrosis. *European Journal of Radiology* 139.January. ISSN: 18727727. DOI: `10.1016/j.ejrad.2021.109653`.

Kurz, Felix.T. et al. (2021). Dependence of the frequency distribution around a sphere on the voxel orientation. *Zeitschrift für Medizinische Physik* 31.4, pp. 403–419. ISSN: 09393889. DOI: `10.1016/j.zemedi.2021.01.005`.

Kutz, J. Nathan, Xing Fu, and Steven L. Brunton (2016). Multiresolution Dynamic Mode Decomposition. *SIAM Journal on Applied Dynamical Systems* 15.2, pp. 713–735. ISSN: 1536-0040. DOI: `10.1137/15M1023543`. arXiv: `1506.00564`.

Kutz, J Nathan et al. (2016). *Dynamic Mode Decomposition*. Philadelphia, PA: Society for Industrial and Applied Mathematics. ISBN: 978-1-61197-449-2. DOI: 10.1137/1.9781611974508.

Lauzon, M Louis and Richard Frayne (2009a). Analytical characterization of RF phase-cycled balanced steady-state free precession. *Concepts in Magnetic Resonance Part A* 34A.3, pp. 133–143. ISSN: 15466086. DOI: 10.1002/cmr.a.20138.

Lauzon, M. Louis and Richard Frayne (2009b). Analytical characterization of RF phase-cycled balanced steady-state free precession. *Concepts in Magnetic Resonance Part A* 34A.3, pp. 133–143. DOI: https://doi.org/10.1002/cmr.a.20138. eprint: https://onlinelibrary.wiley.com/doi/pdf/10.1002/cmr.a.20138.

Le Roux, Pierre-Yves, Grégoire Le Gal, and Pierre-Yves Salaun (2020). Lung scintigraphy for pulmonary embolism diagnosis during the COVID-19 pandemic: does the benefit-risk ratio really justify omitting the ventilation study? *European Journal of Nuclear Medicine and Molecular Imaging* 47.11, pp. 2499–2500. ISSN: 1619-7070. DOI: 10.1007/s00259-020-04964-y.

Lederlin, Mathieu et al. (2013). Functional MRI using Fourier decomposition of lung signal: Reproducibility of ventilation- and perfusion-weighted imaging in healthy volunteers. *European Journal of Radiology* 82.6, pp. 1015–1022. ISSN: 0720048X. DOI: 10.1016/j.ejrad.2012.12.003.

Lee, Hyunji et al. (2019). Morphologic Evaluation of Primary Non-Small Cell Lung Cancer by 3 Tesla MRI with Free-Breathing Ultrashort Echo Time and Radial T1-Weighted Gradient Echo Sequences: A Comparison with CT Analysis. *Journal of the Korean Society of Radiology* 80.3, p. 466. ISSN: 1738-2637. DOI: 10.3348/jksr.2019.80.3.466.

Levitzky, Michael G. (2018). *Pulmonary Physiology*. 9th. McGraw Hill. ISBN: 978-1-26-001934-6.

Lewis, Leonie et al. (2022). Long term outcomes in CDH: Cardiopulmonary outcomes and health related quality of life. *Journal of Pediatric Surgery* 57.11, pp. 501–509. ISSN: 15315037. DOI: 10.1016/j.jpedsurg.2022.03.020.

Lin, Yung-Ya et al. (1997). A Novel DetectionEstimation Scheme for Noisy NMR Signals: Applications to Delayed Acquisition Data. *Journal of Magnetic Resonance* 128.1, pp. 30–41. ISSN: 10907807. DOI: 10.1006/jmre.1997.1215.

Ljimani, Alexandra et al. (2021). Analysis of different image-registration algorithms for Fourier decomposition MRI in functional lung imaging. *Acta Radiologica* 62.7, pp. 875–881. ISSN: 0284-1851. DOI: 10.1177/0284185120944902.

Mai, Vu M., Jack Knight-Scott, and Stuart S. Berr (1999). Improved visualization of the human lung in 1H MRI using multiple inversion recovery for simultaneous suppression of signal contributions from fat and muscle. *Magnetic Resonance in Medicine* 41.5, pp. 866–870. ISSN: 07403194. DOI: 10.1002/(SICI)1522-2594(199905)41:5<866::AID-MRM2>3.0.CO;2-D.

Mendes Pereira, L. et al. (2019). UTE-SENCEFUL: first results for 3D high-resolution lung ventilation imaging. *Magnetic Resonance in Medicine* 81.4, pp. 2464–2473. ISSN: 0740-3194. DOI: 10.1002/mrm.27576.

Michael A. Grippi et al. (2015). *Fishman's Pulmonary Diseases and Disorders*. Vol. 32. 3. McGraw-Hill Education. ISBN: 978-0-07-179672-9.

Middleton, Hunter et al. (1995). MR Imaging with Hyperpolarized3He Gas. *Magnetic Resonance in Medicine* 33.2, pp. 271–275. ISSN: 07403194. DOI: 10.1002/mrm.1910330219.

Miller, G. Wilson et al. (2014). Advances in functional and structural imaging of the human lung using proton MRI. *NMR in Biomedicine* 27.12, pp. 1542–1556. ISSN: 10991492. DOI: 10.1002/nbm.3156.

Mohapatra, Saurav and Thomas J. Overbye (2016). Fast modal identification, monitoring, and visualization for large-scale power systems using Dynamic Mode Decomposition. *2016 Power Systems Computation Conference (PSCC)*. IEEE, pp. 1–7. ISBN: 978-88-941051-2-4. DOI: `10.1109/PSCC.2016.7540904`.

Molinari, Francesco et al. (2008). Oxygen-enhanced magnetic resonance imaging: Influence of different gas delivery methods on the T1-changes of the lungs. *Investigative Radiology* 43.6, pp. 427–432. DOI: `10.1097/RLI.0b013e318169012d`.

Möller, Harald E. et al. (2002). MRI of the lungs using hyperpolarized noble gases. *Magnetic Resonance in Medicine* 47.6, pp. 1029–1051. ISSN: 07403194. DOI: `10.1002/mrm.10173`.

Morini, Francesco, Laura Valfrè, and Pietro Bagolan (2017). Long-term morbidity of congenital diaphragmatic hernia: A plea for standardization. *Seminars in Pediatric Surgery* 26.5, pp. 301–310. ISSN: 1055-8586. DOI: `10.1053/J.SEMPEDSURG.2017.09.002`.

Mullassery, Dhanya and Nicola P. Smith (2015). Lung development. *Seminars in Pediatric Surgery* 24.4, pp. 152–155. ISSN: 15329453. DOI: `10.1053/j.sempedsurg.2015.01.011`.

Muratore, Christopher S. et al. (2001). Pulmonary morbidity in 100 survivors of congenital diaphragmatic hernia monitored in a multidisciplinary clinic. *Journal of Pediatric Surgery* 36.1, pp. 133–140. ISSN: 00223468. DOI: `10.1053/jpsu.2001.20031`.

Neal, Mary A. et al. (2019). Optimized and accelerated 19F-MRI of inhaled perfluoropropane to assess regional pulmonary ventilation. *Magnetic Resonance in Medicine* 82.4, pp. 1301–1311. ISSN: 15222594. DOI: `10.1002/mrm.27805`.

Nichols, Michael B. and Cynthia B. Paschal (2008). Measurement of longitudinal (T1) relaxation in the human lung at 3.0 Tesla with tissue-based and regional gradient analyses. *Journal of Magnetic Resonance Imaging* 27.1, pp. 224–228. ISSN: 10531807. DOI: `10.1002/jmri.21243`.

Nishimura, D.G. (1996). *Principles of Magnetic Resonance Imaging*.

Nyilas, Sylvia et al. (2017). Novel magnetic resonance technique for functional imaging of cystic fibrosis lung disease. *European Respiratory Journal* 50.6, p. 1701464. ISSN: 0903-1936. DOI: `10.1183/13993003.01464-2017`.

Nyilas, Sylvia et al. (2019). Ventilation and perfusion assessed by functional MRI in children with CF: reproducibility in comparison to lung function. *Journal of Cystic Fibrosis* 18.4, pp. 543–550. ISSN: 15691993. DOI: `10.1016/j.jcf.2018.10.003`.

Okuyama, Hiroomi et al. (2006). Correlation between lung scintigraphy and long-term outcome in survivors of congenital diaphragmatic hernia. *Pediatric Pulmonology* 41.9, pp. 882–886. ISSN: 8755-6863. DOI: `10.1002/ppul.20466`.

Oluyomi-Obi, Titilayo, Tim Van Mieghem, and Greg Ryan (2017). Fetal imaging and therapy for CDH-Current status. *Seminars in Pediatric Surgery* 26.3, pp. 140–146. ISSN: 15329453. DOI: `10.1053/j.sempedsurg.2017.04.002`.

Oppenheim, Alan V., Ronald W. Schafer, and John R. Buck (1999). *Discrete-time signal processing*. Prentice Hall.

Otazo, Ricardo, Emmanuel Candès, and Daniel K. Sodickson (2015). Low-rank plus sparse matrix decomposition for accelerated dynamic MRI with separation of background and dynamic components. *Magnetic Resonance in Medicine* 73.3, pp. 1125–1136. DOI: `10.1002/mrm.25240`. arXiv: `NIHMS150003`.

Pauly, John et al. (1989). Slice-selective excitation for very short T2 species. *Proceedings of the 8th Annual Meeting of SMRM*. Amsterdam, p. 28.

Pogorelyuk, Leonid and Clarence W. Rowley (2018). Clustering of Series via Dynamic Mode Decomposition and the Matrix Pencil Method, pp. 1–22. DOI: `10.48550/ARXIV.1802.09878`. arXiv: `1802.09878`.

Prince, Jerry L. and Jonathan M. Links (2015). *Medical Imaging Signals and Systems*. Prentice Hall.

Proctor, Joshua L., Steven L. Brunton, and J. Nathan Kutz (2016). Dynamic Mode Decomposition with Control. *SIAM Journal on Applied Dynamical Systems* 15.1, pp. 142–161. ISSN: 1536-0040. DOI: `10.1137/15M1013857`. arXiv: `2101.02620`.

Rajaram, Smitha et al. (2012). Lung Morphology Assessment with Balanced Steady-State Free Precession MR Imaging Compared with CT. *Radiology* 263.2, pp. 569–577. ISSN: 0033-8419. DOI: `10.1148/radiol.12110990`.

Risse, Frank and Grzegorz Bauman (2016). "MR Perfusion in the Lung". *Dysphagia*. Vol. 39. 1, pp. 53–67. ISBN: 0009-918X. DOI: `10.1007/174_2016_82`. arXiv: `NIHMS150003`.

Roeloffs, Volkert et al. (2019). Frequency-modulated SSFP with radial sampling and subspace reconstruction: A time-efficient alternative to phase-cycled bSSFP. *Magnetic Resonance in Medicine* 81.3, pp. 1566–1579. ISSN: 0740-3194. DOI: `10.1002/mrm.27505`.

Rot, Miha, Martin Horvat, and Gregor Kosec (2022). Dynamic mode decomposition as an analysis tool for time-dependent partial differential equations. *2022 7th International Conference on Smart and Sustainable Technologies (SpliTech)*. IEEE, pp. 1–6. ISBN: 9789532901160. DOI: `10.23919/SpliTech55088.2022.9854243`. arXiv: `2203.04728`.

Sá, Rui Carlos et al. (2014). Validating the distribution of specific ventilation in healthy humans measured using proton MR imaging. *Journal of Applied Physiology* 116.8, pp. 1048–1056. ISSN: 8750-7587. DOI: `10.1152/japplphysiol.00982.2013`.

Sadeghi-Tarakameh, Alireza et al. (2020). In vivo human head MRI at 10.5T: A radiofrequency safety study and preliminary imaging results. *Magnetic Resonance in Medicine* 84.1, pp. 484–496. ISSN: 15222594. DOI: `10.1002/mrm.28093`.

Sanchez, Thomas et al. (2020). Scalable Learning-Based Sampling Optimization for Compressive Dynamic MRI. *ICASSP 2020 - 2020 IEEE International Conference on Acoustics, Speech and Signal Processing (ICASSP)*. 16066. IEEE, pp. 8584–8588. ISBN: 978-1-5090-6631-5. DOI: `10.1109/ICASSP40776.2020.9053345`. arXiv: `1902.00386`.

Sanchez-Crespo, Alejandro (2019). Lung Ventilation/Perfusion Single Photon Emission Computed Tomography (SPECT) in Infants and Children with Nonembolic Chronic Pulmonary Disorders. *Seminars in Nuclear Medicine* 49.1, pp. 37–46. ISSN: 15584623. DOI: `10.1053/j.semnuclmed.2018.10.006`.

Saritas, Emine U., Samantha J. Holdsworth, and Roland Bammer (2014). "Susceptibility Artifacts". *Quantitative MRI of the Spinal Cord*. Elsevier, pp. 91–105. ISBN: 9780123969736. DOI: `10.1016/B978-0-12-396973-6.00007-1`.

Sarkar, T.K. and Odilon Pereira (1995). Using the matrix pencil method to estimate the parameters of a sum of complex exponentials. *IEEE Antennas and Propagation Magazine* 37.1, pp. 48–55. ISSN: 1045-9243. DOI: `10.1109/74.370583`.

Scheffler, Klaus and Stefan Lehnhardt (2003). Principles and applications of balanced SSFP techniques. *European Radiology* 13.11, pp. 2409–2418. ISSN: 0938-7994. DOI: `10.1007/s00330-003-1957-x`.

Schmid, P. J. et al. (2011). Applications of the dynamic mode decomposition. *Theoretical and Computational Fluid Dynamics* 25.1-4, pp. 249–259. ISSN: 0935-4964. DOI: `10.1007/s00162-010-0203-9`.

Schneider, Wilfried, Thomas Bortfeld, and Wolfgang Schlegel (2000). Correlation between CT numbers and tissue parameters needed for Monte Carlo simulations of clinical dose distributions. *Physics in Medicine and Biology* 45.2, pp. 459–478. ISSN: 00319155. DOI: `10.1088/0031-9155/45/2/314`.

Schönfeld, Christian et al. (2015). Performance of perfusion-weighted Fourier decomposition MRI for detection of chronic pulmonary emboli. *Journal of Magnetic Resonance Imaging* 42.1, pp. 72–79. ISSN: 10531807. DOI: `10.1002/jmri.24764`.

Section on Surgery and the Committee on Fetus and Newborn (2008). Postdischarge Follow-up of Infants With Congenital Diaphragmatic Hernia. *Pediatrics* 121.3, pp. 627–632. ISSN: 0031-4005. DOI: `10.1542/peds.2007-3282`.

Serai, Suraj D. et al. (2020). Pediatric lung MRI: Currently available and emerging techniques. *American Journal of Roentgenology* 216.3, pp. 781–790. ISSN: 15463141. DOI: `10.2214/AJR.20.23104`.

Shahdloo, Mohammad et al. (2019). Projection onto Epigraph Sets for Rapid Self-Tuning Compressed Sensing MRI. *IEEE Transactions on Medical Imaging* 38.7, pp. 1677–1689. ISSN: 0278-0062. DOI: `10.1109/TMI.2018.2885599`.

Stadler, Alfred et al. (2005). T1 mapping of the entire lung parenchyma: Influence of the respiratory phase in healthy individuals. *Journal of Magnetic Resonance Imaging* 21.6, pp. 759–764. ISSN: 1053-1807. DOI: `10.1002/jmri.20319`.

Stefanutti, Giorgio et al. (2004). Cardiopulmonary Anatomy and Function in Long-Term Survivors of Mild to Moderate Congenital Diaphragmatic Hernia. *Journal of Pediatric Surgery* 39.4, pp. 526–531. ISSN: 0022-3468. DOI: `10.1016/j.jpedsurg.2003.12.006`.

Stewart, Neil J. et al. (2018). Comparison of 3He and 129Xe MRI for evaluation of lung microstructure and ventilation at 1.5T. *Journal of Magnetic Resonance Imaging* 48.3, pp. 632–642. ISSN: 10531807. DOI: `10.1002/jmri.25992`.

Tedjasaputra, Vince et al. (2013). The heterogeneity of regional specific ventilation is unchanged following heavy exercise in athletes. *Journal of Applied Physiology* 115.1, pp. 126–135. ISSN: 8750-7587. DOI: `10.1152/japplphysiol.00778.2012`.

Tibiletti, Marta et al. (2016). Multistage three-dimensional UTE lung imaging by image-based self-gating. *Magnetic Resonance in Medicine* 75.3, pp. 1324–1332. ISSN: 0740-3194. DOI: `10.1002/mrm.25673`.

Tiddens, Harm A.W.M. et al. (2018). Paediatric lung imaging: The times they are a-changin'. *European Respiratory Review* 27.147, pp. 1–9. ISSN: 16000617. DOI: `10.1183/16000617.0097-2017`.

Tirunagari, Santosh et al. (2017). Movement correction in DCE-MRI through windowed and reconstruction dynamic mode decomposition. *Machine Vision and Applications* 28.3-4, pp. 393–407. ISSN: 0932-8092. DOI: `10.1007/s00138-017-0835-5`.

Torres, Luis et al. (2019). Structure-Function Imaging of Lung Disease Using Ultrashort Echo Time MRI. *Academic Radiology* 26.3, pp. 431–441. ISSN: 10766332. DOI: `10.1016/j.acra.2018.12.007`.

Trinh, Wei and Thomas Overbye (2019). Comparison of Dynamic Mode Decompositon and Iterative Matrix Pencil Method for Power System Modal Analysis. *2019 International Conference on Smart Grid Synchronized Measurements and Analytics (SGSMA)*. IEEE, pp. 1–6. ISBN: 978-1-7281-1607-5. DOI: `10.1109/SGSMA.2019.8784536`.

Tu, Jonathan H. et al. (2014). On dynamic mode decomposition: Theory and applications. *Journal of Computational Dynamics* 1.2, pp. 391–421. ISSN: 2158-2505. DOI: `10.3934/jcd.2014.1.391`. arXiv: `1312.0041`.

Voskrebenzev, Andreas and Jens Vogel-Claussen (2020). Proton MRI of the Lung: How to Tame Scarce Protons and Fast Signal Decay. *Journal of Magnetic Resonance Imaging*, pp. 1–14. ISSN: 15222586. DOI: 10.1002/jmri.27122.

Voskrebenzev, Andreas et al. (2017). Low-pass imaging of dynamic acquisitions (LIDA) with a group-oriented registration (GOREG) for proton MR imaging of lung ventilation. *Magnetic Resonance in Medicine* 78.4, pp. 1496–1505. DOI: 10.1002/mrm.26526.

Voskrebenzev, Andreas et al. (2018). Feasibility of quantitative regional ventilation and perfusion mapping with phase-resolved functional lung (PREFUL) MRI in healthy volunteers and COPD, CTEPH, and CF patients. *Magnetic Resonance in Medicine* 79.4, pp. 2306–2314. ISSN: 0740-3194. DOI: 10.1002/mrm.26893.

Walkup, Laura L., Nara S. Higano, and Jason C. Woods (2019). Structural and Functional Pulmonary Magnetic Resonance Imaging in PediatricsFrom the Neonate to the Young Adult. *Academic Radiology* 26.3, pp. 424–430. ISSN: 10766332. DOI: 10.1016/j.acra.2018.08.006.

Weidner, Meike et al. (2014). High temporal versus high spatial resolution in MR quantitative pulmonary perfusion imaging of two-year old children after congenital diaphragmatic hernia repair. *European Radiology* 24.10, pp. 2427–2434. ISSN: 14321084. DOI: 10.1007/s00330-014-3304-9.

Weiger, Markus and Klaas P. Pruessmann (2019). Short-T2 MRI: Principles and recent advances. *Progress in Nuclear Magnetic Resonance Spectroscopy* 114-115, pp. 237–270. ISSN: 00796565. DOI: 10.1016/j.pnmrs.2019.07.001.

Weis, Meike et al. (2016a). Lung Perfusion MRI After Congenital Diaphragmatic Hernia Repair in 2-Year-Old Children With and Without Extracorporeal Membrane Oxygenation Therapy. *American Journal of Roentgenology* 206.6, pp. 1315–1320. ISSN: 0361-803X. DOI: 10.2214/AJR.15.14860.

Weis, Meike et al. (2016b). Region of interest-based versus whole-lung segmentation-based approach for MR lung perfusion quantification in 2-year-old children after congenital diaphragmatic hernia repair. *European Radiology* 26.12, pp. 4231–4238. ISSN: 0938-7994. DOI: 10.1007/s00330-016-4330-6.

West, John B. and Andrew M. Luks (2016). *West's Respiratory Physiology: The Essentials*. 10th. Wolters Kluwer Health. ISBN: 978-1496310118.

Wiesinger, Florian et al. (2006). Potential and feasibility of parallel MRI at high field. *NMR in Biomedicine* 19.3, pp. 368–378. ISSN: 09523480. DOI: 10.1002/nbm.1050.

Wild, J. M. et al. (2012a). MRI of the lung (1/3): Methods. *Insights into Imaging* 3.4, pp. 345–353. ISSN: 18694101. DOI: 10.1007/s13244-012-0176-x.

Wild, J. M. et al. (2012b). MRI of the lung (1/3): methods. *Insights into Imaging* 3.4, pp. 345–353. ISSN: 1869-4101. DOI: 10.1007/s13244-012-0176-x.

Wong, Matthew et al. (2018). Pulmonary hypertension in congenital diaphragmatic hernia patients: Prognostic markers and long-term outcomes. *Journal of Pediatric Surgery* 53.5, pp. 918–924. ISSN: 00223468. DOI: 10.1016/j.jpedsurg.2018.02.015.

Yang, Shuyi et al. (2020). Clinical Potential of UTE-MRI for Assessing COVID-19: Patient- and Lesion-Based Comparative Analysis. *Journal of Magnetic Resonance Imaging*, pp. 397–406. ISSN: 15222586. DOI: 10.1002/jmri.27208.

Yu, Jiangsheng, Yiqun Xue, and Hee Kwon Song (2011). Comparison of lung T2* during free-breathing at 1.5 T and 3.0 T with ultrashort echo time imaging. *Magnetic Resonance in Medicine* 66.1, pp. 248–254. ISSN: 15222594. DOI: 10.1002/mrm.22829.

Zanette, Brandon et al. (2022). Clinical Feasibility of Structural and Functional MRI in Free-Breathing Neonates and Infants. *Journal of Magnetic Resonance Imaging*, pp. 1–12. ISSN: 15222586. DOI: 10.1002/jmri.28165.

Zapke, Maren et al. (2006). Magnetic resonance lung function a breakthrough for lung imaging and functional assessment? A phantom study and clinical trial. *Respiratory Research* 7.1, p. 106. ISSN: 1465-993X. DOI: 10.1186/1465-9921-7-106.

Zhi-Pei Liang and Paul C. Lauterbur (2000). *Principles of Magnetic Resonance Imaging: A Signal Processing Perspective*. Wiley-IEEE Press, p. 416. ISBN: 9780470545652.

Zöllner, F. G. et al. (2012). Quantitative pulmonary perfusion imaging at 3.0 T of 2-year-old children after congenital diaphragmatic hernia repair: initial results. *European Radiology* 22.12, pp. 2743–2749. ISSN: 0938-7994. DOI: 10.1007/s00330-012-2528-9.

Zöllner, Frank G. et al. (2016). An open source software for analysis of dynamic contrast enhanced magnetic resonance images: UMMPerfusion revisited. *BMC Medical Imaging* 16.1, pp. 1–13. ISSN: 1471-2342. DOI: 10.1186/s12880-016-0109-0.

Appendix A

Publications

A.1 Peer-Reviewed Journal Publications

1. **Efe Ilicak**, Safa Ozdemir, Jascha Zapp, Lothar R. Schad, Frank G. Zöllner. "Dynamic Mode Decomposition of Dynamic MRI for Assessment of Pulmonary Ventilation and Perfusion." *Magnetic Resonance in Medicine.* 2023 Aug; 90(2): 761- 769. doi:10.1002/mrm.29656.

2. **Efe Ilicak**, Safa Ozdemir, Lothar R. Schad, Meike Weis, Stefan o. Schoenberg, Frank G. Zöllner, Jascha Zapp. "Phase-cycled balanced SSFP imaging for non-contrast-enhanced functional lung imaging." *Magnetic Resonance in Medicine.* 2022 Oct; 88(4): 1764-1774. doi:10.1002/mrm.29302.

3. **Efe Ilicak**, Emine U. Saritas, Tolga Çukur. "Automated Parameter Selection for Accelerated MRI Reconstruction via Low-Rank Modeling of Local k-Space Neighborhoods." *Zeitschrift für Medizinische Physik.* 2022 Feb. doi:10.1016/j.zemedi.2022.02.002.

4. Sabrina K. Bech, Haiyun Qi, Christian Ø. Mariager, Esben S.S. Hansen, **Efe Ilicak**, Frank G. Zöllner, Christoffer Laustsen. "The number of glomeruli and pyruvate metabolism is not strongly coupled in the healthy rat kidney." *Magnetic Resonance in Medicine.* 2022 Feb; 87: 896-903. doi:10.1002/mrm.29025.

5. Mohammad Shahdloo, **Efe Ilicak**, Mohammad Tofighi, Emine U. Saritas, A. Enis Çetin and Tolga Çukur. "Projection onto Epigraph Sets for Rapid Self-Tuning Compressed Sensing MRI." *IEEE Transactions on Medical Imaging.* 2019 Jul; 38(7): 1677-1689. doi:10.1109/TMI.2018.2885599.

6. Baran Gozcu, Rabeeh Karimi Mahabadi, Yen-Huan Li, **Efe Ilıcak**, Tolga Cukur, Jonathan Scarlett, Volkan Cevher. "Learning-Based Compressive MRI." *IEEE Transactions on Medical Imaging.* 2018 Jun; 37(6): 1394-1406. doi:10.1109/TMI.2018.2832540.

7. Erdem Biyik, **Efe Ilicak**, Tolga Çukur. "Reconstruction by calibration over tensors for multi-coil multi-acquisition balanced SSFP imaging." *Magnetic Resonance in Medicine.* 2018 May; 79(5): 2542-2554. doi:10.1002/mrm.26902.

8. **Efe Ilicak**, L. Kerem Senel, Erdem Biyik, Tolga Çukur. "Profile-encoding reconstruction for multiple-acquisition balanced steady-state free precession imaging." *Magnetic Resonance in Medicine.* 2017 Oct; 78(4): 1316-1329. doi:10.1002/mrm.26507.

9. **Efe Ilicak**, Suheyla Cetin, Elif Bulut, Kader K. Oguz, Emine U. Saritas, Gozde Unal, Tolga Çukur. "Targeted vessel reconstruction in non-contrast-enhanced

steady-state free precession angiography." *NMR in Biomedicine.* 2016 May; 29 (5): 532-544. doi:10.1002/nbm.3497.

A.2 Journal Publications Under Peer-Review

1. **Efe Ilicak**, Greta Thater, Safa Ozdemir, Jascha Zapp, Lothar R. Schad, Stefan O. Schoenberg, Frank G. Zöllner, Meike Weis. "Functional lung imaging of 2-year-old children after congenital diaphragmatic hernia repair using dynamic mode decomposition." *European Radiology*. Submitted on 19.04.2023.

A.3 Peer-Reviewed Conference Proceedings

1. Safa Ozdemir, **Efe Ilicak**, "Investigating Variable Density Sampling Patterns in Spiral Trajectories for use in MREPT" in *Proc. Intl. Soc. Mag. Reson. Med.* 2023; 31 (Toronto, CA): 5164.
2. **Efe Ilicak**, Safa Ozdemir, Jascha Zapp, Lothar R. Schad, Frank G. Zöllner. "Using Dynamic Mode Decomposition for Functional Lung Imaging." in *Proc. Intl. Soc. Mag. Reson. Med.* 2022; 31 (Toronto, CA): 4671.
3. Safa Ozdemir, **Efe Ilicak**, Lothar R. Schad, Frank G. Zöllner. "Investigating Spiral Trajectories for Sub-second Conductivity Imaging." in *Proc. Intl. Soc. Mag. Reson. Med.* 2022; 30 (London, UK): 2915.
4. **Efe Ilicak**, Safa Ozdemir, Lothar R. Schad, Jascha Zapp, Frank G. Zöllner. "Improving reconstruction quality in non-contrast-enhanced functional lung imaging via LORAKS." in *Proc. Intl. Soc. Mag. Reson. Med.* 2022; 30 (London, UK): 1478.
5. Safa Ozdemir, **Efe Ilicak**, Carmen Stutz, Mara Berger, Jascha Zapp, Lothar R. Schad, Frank G. Zöllner. "Fast 3D Undersampled Bloch-Siegert based $B_{+}1$ Mapping for use in MREPT." in *Proc. Intl. Soc. Mag. Reson. Med.* 2021; 29 (Virtual Meeting): 3780.
6. **Efe Ilicak**, Jascha Zapp, Safa Ozdemir, Lothar R. Schad, Frank G. Zöllner. "Phase-Cycled Balanced Steady-State Free Precession Imaging for Functional Lung Imaging at 1.5 and 3 Tesla." in *Proc. Intl. Soc. Mag. Reson. Med.* 2021; 29 (Virtual Meeting): 3230.
7. Ken-Ju Chao, **Efe Ilicak**, Jascha Zapp, Lothar R. Schad, Frank G. Zöllner. "Low-rank plus sparse compressed sensing for accelerated pulmonary imaging." in *Proc. ESMRMB Congress.* 2020; 37 (Virtual Meeting): 191-192.
8. **Efe Ilicak**, Jascha Zapp, Lothar R. Schad, Frank G. Zöllner. "Low-rank and sparse matrix decomposition for accelerated non-contrast-enhanced functional lung MRI." in *Proc. Intl. Soc. Mag. Reson. Med.* 2020; 28 (Virtual Meeting): 2310.
9. Thomas Sanchez, Baran Gözcü, Ruud B. van Heeswijk, Armin Eftekhari, **Efe Ilıcak**, Tolga Çukur, Volkan Cevher. "Scalable learning-based sampling optimization for compressive dynamic MRI" in *IEEE International Conference on Acoustics, Speech, and Signal Processing* 2020; 45 (Virtual Meeting): 8584-8588.

10. **Efe Ilicak**, Lothar R. Schad, Jorge Chacon-Caldera. "Glomerular quantification from undersampled data using compressed sensing reconstructions." in *Proc. ESMRMB Congress.* 2019; 36 (Rotterdam, NL): 317.
11. **Efe Ilicak**, Jascha Zapp, Lothar R. Schad, Frank G. Zöllner. "Assessment of scan parameter effects on time resolved bSSFP acquisition for Fourier Decomposition Pulmonary MR" in *Proc. Intl. Soc. Mag. Reson. Med.* 2019; 27 (Montreal, CA): 4093.
12. **Efe Ilicak**, Jorge Chacon-Caldera, Jascha Zapp, Lothar R. Schad, Frank G. Zöllner. "Compressed Sensing reconstruction in non-contrast-enhanced functional lung MRI using Fourier Decomposition: An initial study" in *Proc. Intl. Soc. Mag. Reson. Med.* 2019; 27 (Montreal, CA): 1897.
13. Mohammad Shahdloo, **Efe Ilicak**, Mohammad Tofighi, Emine U. Saritas, A. Enis Çetin and Tolga Çukur. "Rapid self-tuning compressed-sensing MRI using projection onto epigraph sets." in *Proc. Intl. Soc. Mag. Reson. Med.* 2018; 26 (Paris, FR): 251.
14. Toygan Kilic, **Efe Ilicak**, Tolga Cukur, Emine U. Saritas. "Improved SPIRiT Operator for Joint Reconstruction of Multiple T2-weighted Images." in *Proc. Intl. Soc. Mag. Reson. Med.* 2017; 25 (Honolulu, USA): 5165.
15. Yigit B. Can, **Efe Ilicak**, Tolga Cukur. "Fast 3D Variable-FOV Reconstruction for Parallel Imaging with Localized Sensitivities." in *Proc. Intl. Soc. Mag. Reson. Med.* 2017; 25 (Honolulu, USA): 5158.
16. **Efe Ilicak**, Tolga Cukur. "Parameter-Free Profile Encoding Reconstruction for Multiple-Acquisition bSSFP Imaging." in *Proc. Intl. Soc. Mag. Reson. Med.* 2017; 25 (Honolulu, USA): 571.
17. **Efe Ilicak**, Tolga Cukur. "Huber function based reconstruction in accelerated phase-cycled bSSFP acquisitions for increased detection performance." in *IEEE Signal Processing and Communications Applications Conference* 2016; 25 (Antalya, TR): 1-4.
18. **Efe Ilicak**, Suheyla Cetin, Emine U. Saritas, Gozde Unal, Tolga Çukur. "Adaptive reconstruction for vessel preservation in unenhanced MR angiography." in *IEEE Signal Processing and Communications Applications Conference* 2016; 24 (Zonguldak, TR): 577-580.

Appendix B

Curriculum Vitae

B.1 Personal Data

Name:	Efe Ilıcak (Ilicak)
Date of Birth:	3 June 1992
Place of Birth:	Çankaya, Ankara
Nationality:	Turkish

B.2 Education

2018 – Present	Doctoral Candidate (Dr. sc. hum.), Computer Assisted Clinical Medicine, Ruprecht Karl University of Heidelberg, Supervisor: Prof. Dr. rer. nat. Lothar R. Schad.
2017 – 2018	Doctor of Philosophy (Exited program), Electrical and Electronics Engineering, İhsan Doğramacı Bilkent University, Supervisor: Prof. Dr. Tolga Çukur.
2014 – 2017	Master of Science, Electrical and Electronics Engineering, İhsan Doğramacı Bilkent University, Supervisor: Prof. Dr. Tolga Çukur.

B.3 Work Experience

2018 – Present	Research Assistant Project: Functional lung imaging using MRI. Chair in Computer Assisted Clinical Medicine, Ruprecht Karl University of Heidelberg.
2014 – 2018	Research Assistant Project: Compressed sensing techniques for accelerated MRI. Department of Electrical and Electronics Engineering, İhsan Doğramacı Bilkent University.

B.4 Teaching Experience

	Teaching Assistant Ruprecht Karl University of Heidelberg,
2021 – Present	Biomedical Engineering - Medical Physics in Imaging.
2018 – Present	Translational Medical Research - MRI Techniques.
	Teaching Assistant İhsan Doğramacı Bilkent University,
2016 – 2018	Senior Design Project.
2015 – 2016	Computational Neuroscience, Medical Imaging.
2014 – 2015	Analog Electronics, Microprocessors.

Appendix C

Acknowledgements

I would like to express my sincere gratitude to all the individuals who have supported me during my PhD journey. Without their help and guidance, this thesis would not have been possible.

First and foremost, I would like to thank Prof. Dr. Lothar R. Schad, for his support and encouragement throughout this journey. I am immensely thankful for the opportunity to be a part of his lab, and for the independence he has given me to pursue my scientific interests.

I would also like to thank Prof. Dr. Frank Zöllner for his invaluable scientific guidance and support, which has been crucial to the completion of this thesis. I am also thankful for the resources and opportunities he has provided.

I would also like to express my gratitude to Dr. Jascha Zapp for his continuous support and supervision. He has been patient, understanding, and always willing to share his knowledge and expertise. His feedback has helped me to develop my skills and improve my work.

A great deal of appreciation goes to all the current and former members of CKM. I am indebted to my colleagues and friends who have provided me with emotional support and encouragement during the ups and downs of this journey. The warm and welcoming atmosphere in our office, the competitive foosball sessions, and the wild conversations we had during our coffee breaks were all greatly appreciated. I would like to extend a special thank you to Valerie, Safa, Anne, Irène, and Jorge for all the help and emotional support they provided me during this process.

Finally, my utmost gratitude goes to my family, for their endless love and unconditional support. I am especially grateful to my parents, Meltem and Sinan, my brother Ege and his family, including Maria and Lara, and to Tamara for being there for me during the most challenging moments. I cannot express how grateful I am, as without them, none of this would have been possible. Thank you for always believing in me, and standing by me throughout this journey.